Springer Series in Surface Sciences 75

Zhong Lin Wang

Contact-Electrification of Matter

Springer

Springer Series in Surface Sciences

Volume 75

This series covers the whole spectrum of surface sciences, including structure and dynamics of clean and adsorbate-covered surfaces, thin films, basic surface effects, analytical methods and also the physics and chemistry of interfaces. Written by leading researchers in the field, the books are intended primarily for researchers in academia and industry and for graduate students.

Zhong Lin Wang

Contact-Electrification of Matter

Springer

Zhong Lin Wang
Beijing Institute of Nanoenergy
and Nanosystems
Chinese Academy of Sciences
Beijing, China

Georgia Institute of Technology
Atlanta, USA

ISSN 0931-5195 ISSN 2198-4743 (electronic)
Springer Series in Surface Sciences
ISBN 978-3-031-88503-7 ISBN 978-3-031-88504-4 (eBook)
https://doi.org/10.1007/978-3-031-88504-4

This Springer imprint is published by the registered company Springer Nature Switzerland AG
The registered company address is: Gewerbestrasse 11, 6330 Cham, Switzerland

Preface

Contact-electrification (CE) refers to a process by which materials become electrically charged when they come into direct contact with each other and then are separated. This phenomenon is commonly known as triboelectrification (TE) in our daily life and is a fundamental aspect of static electricity. The key feature of CE is the transfer of charges between two objects when they come into contact, resulting in one object becoming positively charged and the other negatively charged. In fact, CE is a common phenomenon of matter between any two partners of liquids, solid and gases.

Although TE has been known for over 2600 years, the study about its mechanisms has been cumbersome and rather sluggish, possibly because the phenomenon was viewed from different angles by different communities of scientists and lacking of proper techniques. Because TE is always treated as a negative effect so there is a little motivation for studying it. In the last two decades, fundamental studies about CE has excited a lot of interest because the invention of the triboelectric nanogenerators (TENGs), which is a paradigm shift technology for harvesting mechanical energy with the use of contact-electrification effect. This book is to summarize the progresses made in the field for systematically covering the CE in systems made of liquid, solid and/or gas. We intend to give an updated review in understanding the CE and its various applications. Part I of the book from Chaps. 1–8 is about the fundamental science related to CE, as outlined in follows:

Chapter 1 by Zhong Lin Wang and Aurelia C. Wang is to introduce the brief history about the study of TE. The chapter also summarizes the major contributions made by TE for human civilization. By introducing the new developments in understanding CE and associated applications, there is a desperate need for authoring a text book, so that the science and technologies associated with CE can be advanced faster. This chapter serves as the basis for future chapters.

Chapter 2 by Haiyang Zou, Shiquan Lin, Xiangtian Ding and Zhong Lin Wang is on the methods and techniques for quantifying CE. The basic techniques used for quantifying the density of surface charges from nano-scale to macroscopic scale

are presented. The standards set up for quantifying CE are also covered. The establishments of these techniques are critical for studying interface charge transfers at various interfaces.

Chapter 3 by Lok C. Lew Yan Voon and Morten Willatzen is on the theory for understanding the CE. Both semi-classical and first principle quantum theories are introduced. Theoretical understanding about CE is at the early phase in comparison to experimental progress. Much more work is required in the future.

Chapter 4 by Xiangyu Chen and Zhong Lin Wang is on the CE at metal-insulator interface, by mainly introducing Schottky barrier related charge transfer process. This study is possible by the using of atomic force microscopy related probe techniques. By either varying the sample temperature or applying a bias voltage, the dominant charge carriers are proved to be electrons.

Chapter 5 by Cheng Xu and Zhong Lin Wang is about the CE between insulator and insulator. The energy band model is first introduced, which is useful for understanding the electron transfer between materials that can be described using energy band diagram with the introduce of surface states. Then, the electron cloud model first proposed by Wang in 2018 are presented in details, which is believed to be a more general understanding about CE in matters. By assuming that the electron transfer is the dominant process for CE, charge transfer is only possible in the areas there are close contact between atoms with a strong overlap of electron wave functions. Various charge releasing mechanisms are also presented.

Chapter 6 by Shiquan Lin, Xiangtian Ding and Zhong Lin Wang is to introduce the fundamentals about CE at semiconductor interfaces, with a focus on the newly discovered effect—the tribovoltaic effect, which was first proposed by Wang in 2019. By sliding an n-type semiconductor on a p-type semiconductor as an example, the binding between two atoms at the interface would release a binding energy, called bindington, which may exist in a form of internal photons and can excite local electron-hole pairs, which are then separated by the build-in electric field at the pn junction, resulting in a DC output. The effect is now a new area of studies for dynamic semiconductor interfaces for sending and energy harvesting.

Chapter 7 by Di Wei systematically describes the CE at a liquid-solid interface, emphasizing charge transfer processes across interfaces involving conductors, dielectrics, and semiconductors. It emphasizes the formation and dynamics of the electrical double layer (EDL), a fundamental structure regulating charge behavior at a liquid-solid interface. Wang's two-step model is introduced to elucidate the role played by CE in EDL formation on dielectric surfaces, which describe the key factor contributed by electron transfer at the interface and its initial contribution to the formation of EDL.

Chapter 8 by Ziming Wang, Mulin He, Xueyan Yang and Zhong Lin Wang introduces the newly discovered contact-electro-catalysis (CEC), first discovered by Wang's group in 2022, which is about the contact-electrification-driven electron transfer at a liquid-solid interface to facilitate local redox reactions. This chapter provides a comprehensive overview of the theoretical foundation of CEC, strategies for improving CEC, and the unique advantages of CEC. Additionally, a roadmap for future research and development of CEC has been proposed.

Part II of this book from Chaps. 9–12 is about the various applications of CE:

Chapter 9 by Ying-Chih Lai and Jie Wang systematically describes the fundamental approach and technological applications of triboelectric nanogenerators (TENGs). Starting with the introduction of the two primary types of TENGs: AC-type and DC-type, the chapter presents the five working modes of AC-type TENGs and the two material types used in DC TENGs. Key aspects of performance optimization, material selection, environmental control, and charge excitation in solid-solid TENGs are also discussed. TENG applications have been reviewed in the fields of as micro/nano power sources (e.g., from body motion energy, mechanical energy under in vivo conditions, vibration energy, and wind energy), self-powered sensors (including tactile, biomechanical, acoustic, human physiological, and chemical sensing), blue energy harvesting, and high-voltage sources.

Chapter 10 by Gang Cheng, Jinyang Zhang, and Huaifang Qin is about the applications of TENG based on CE between liquid and solid, range from water energy harvesting to sensing systems. TENG has been demonstrated as a probe for measuring the charge transfer and a liquid-solid interface, which is believed to be important for fundamental chemistry. In this chapter, recent advancements in the applications of TENGs utilizing liquid-solid CE are introduced in detail, the applications mainly focus on their roles as energy harvesters, sensors, and TENG probes, which can realize liquid kinetic energy converted into electricity, self-powered microfluidic or chemical sensing, and the liquid-solid interface study.

Chapter 11 by Chi Zhang and Zhi Zhang is about the tribovoltaic nanogenerator (TVNG) as an innovative energy conversion device using the tribovoltaic effect, with great application potential in areas such as mechanical components, multi-source energy harvesting, intelligent flexible devices, and self-powered sensing systems. The chapter also demonstrate the broad adaptability and high efficiency of the tribovoltaic effect across different scenarios but also guide the development of future intelligent systems and new energy technologies.

Chapter 12 by Wei Tang and Peng Jiang is about the applications of contact-electro-catalysis (CEC), including pollutant degradation, CO_2 capture, the synthesis of important chemicals (such as hydrogen peroxide and ammonia), resource recovery (e.g., recycling of lithium-ion batteries and precious metals), and even cancer therapy. CEC offers high reaction efficiency under mild conditions, which sets it apart from more demanding catalytic processes. A particularly significant advantage of CEC lies in its broad catalyst selections including many conventional organic and inorganic materials. Moreover, the scope of CEC extends beyond solid catalysts to liquid-liquid interfaces, such as oil-water boundaries, where liquid-liquid contact electrification can induce electron transfer to drive redox reactions, similar to solid-liquid systems. This opens up new possibilities for catalytic processes at liquid interfaces, where traditional catalytic methods may be less effective.

I have a long wish to get this book written up because I believe that there is an urgent need for such a book, which can be useful for a broad range of readers to understand CE, a phenomenon that is most well-known, available anywhere and happening all the time in nature, but lacking of in-depth of scientific understanding. I believe that the study of CE has been a “forgotten” corner in science in the past

centuries possibly due to its negative effects in many cases, such as causing fire and discharge, but now TENG possibly is the 5th major applications of CE in broad, therefore, a systematic understanding is very important. The book is intended as a text and reference book for students and researchers in the fields of physics, chemistry, materials science and electric engineering. Finally, I like to thank all of the authors who have contributed to this book. The book is impossible without the support of many colleagues and collaborators, to whom I am very grateful.

Zhong Lin Wang, Ph.D.
Chief Scientist
Chair Professor and Director
Beijing Institute of Nanoenergy
and Nanosystems
Chinese Academy of Sciences
Beijing, China
wangzhonglin@binn.cas.cn

Georgia Institute of Technology
Atlanta, USA

Competing Interests The author has no competing interests to declare that are relevant to the content of this manuscript.

Contents

Contributors

Xiangyu Chen Beijing Institute of Nanoenergy and Nanosystems, Chinese Academy of Sciences, Beijing, China

Gang Cheng Key Lab for Special Functional Materials of Ministry of Education, School of Nanoscience and Materials Engineering, Henan University, Kaifeng, China

Xiangtian Ding School of Mechanical Engineering, Beijing Institute of Technology, Beijing, China;
Hebei Key Laboratory of Intelligent Assembly and Detection Technology, Tangshan Research Institute, Beijing Institute of Technology, Tangshan, China

Mulin He Beijing Institute of Nanoenergy and Nanosystems, Chinese Academy of Sciences, Beijing, China

Peng Jiang School of Pharmaceutical Sciences, Wuhan University, Wuhan, China

Ying-Chih Lai Department of Materials Science and Engineering, National Chung Hsing University, Taichung, Taiwan;
Innovation and Development Center of Sustainable Agriculture, i-Center for Advanced Science and Technology, National Chung Hsing University, Taichung, Taiwan;
Department of Physics, National Chung Hsing University, Taichung, Taiwan

Shiquan Lin School of Mechanical Engineering, Beijing Institute of Technology, Beijing, China;
Hebei Key Laboratory of Intelligent Assembly and Detection Technology, Tangshan Research Institute, Beijing Institute of Technology, Tangshan, China

Huaifang Qin Key Lab for Special Functional Materials of Ministry of Education, School of Nanoscience and Materials Engineering, Henan University, Kaifeng, China

Lok C. Lew Yan Voon College of Sciences, University of Findlay, Findlay, OH, USA

Aurelia C. Wang School of Materials Science and Engineering, Georgia Institute of Technology, Atlanta, GA, USA

Jie Wang Beijing Institute of Nanoenergy and Nanosystems, Chinese Academy of Sciences, Beijing, China

Zhong Lin Wang Beijing Institute of Nanoenergy and Nanosystems, Chinese Academy of Sciences, Beijing, China

Ziming Wang Beijing Institute of Nanoenergy and Nanosystems, Chinese Academy of Sciences, Beijing, China

Di Wei Beijing Institute of Nanoenergy and Nanosystems, Chinese Academy of Sciences, Beijing, China

Tang Wei Beijing Institute of Nanoenergy and Nanosystems, Chinese Academy of Sciences, Beijing, China

Morten Willatzen Department of Mathematical Sciences, Aalborg University, Aalborg, Denmark

Cheng Xu School of Materials Science and Physics, China University of Mining and Technology, Xuzhou, Jiangsu, China

Xueyan Yang Beijing Institute of Nanoenergy and Nanosystems, Chinese Academy of Sciences, Beijing, China

Chi Zhang Beijing Key Laboratory of Micro-nano Energy and Sensor, CAS Center for Excellence in Nanoscience, Beijing Institute of Nanoenergy and Nanosystems, Chinese Academy of Sciences, Beijing, China

Jinyang Zhang Beijing Institute of Nanoenergy and Nanosystems, Chinese Academy of Sciences, Beijing, China

Zhi Zhang Beijing Key Laboratory of Micro-nano Energy and Sensor, CAS Center for Excellence in Nanoscience, Beijing Institute of Nanoenergy and Nanosystems, Chinese Academy of Sciences, Beijing, China

Haiyang Zou College of Materials Science and Engineering, Sichuan University, Chengdu, China

Chapter 7
Contact Electrification at Liquid-Solid Interfaces

Abstract The liquid-solid (L-S) interface, ubiquitous in nature, serves as a critical boundary for addressing fundamental scientific problems. Its prevalence and intricate dynamics underpin a wide range of essential physical and chemical phenomena essential to fields such as catalysis, energy, sensors and environmental science, offering profound opportunities for exploration in various disciplines. The functionality of the L-S interface is rooted in charge accumulation and release driven by potential gradients or disparities in material properties across the phases. This chapter delves into the mechanisms of contact electrification (CE) at L-S interfaces, emphasizing charge transfer processes across interfaces involving conductors, dielectrics, and semiconductors. It emphasizes the formation and dynamics of the electrical double layer (EDL), a fundamental structure regulating charge behavior at interfaces. Wang's two-step model is introduced to elucidate the role of CE in EDL formation on dielectric surfaces. Key discussions include ion and electron transfer quantification, advanced electron transfer modeling, and the hybrid characteristics of the EDL, shedding light on the physics of L-S CE. The chapter explores techniques for dynamic EDL regulation through electric fields or mechanical methods to control charge carrier behavior. By modulating ion migration and optimizing charge concentration at interfaces, these strategies directly influence energy scavenging, storage, and processes of information flow etc. Practical applications of L-S CE are demonstrated across various devices. At liquid-conductor interfaces, EDL regulation underpins efficient energy storage in supercapacitors and the functionality of electrochemical sensors. For liquid-dielectric interfaces, the dynamic regulation of the EDL has catalyzed innovations in high-efficiency energy harvesting and information flow, such as triboelectric nanogenerators (TENGs) and triboiontronic nanogenerators (TINGs). At liquid-semiconductor interfaces, the tribovoltaic effect harnesses L-S CE for effective direct current (DC) energy generation. These advancements highlight the vast and new application potential of EDL regulation at L-S interfaces, laying the foundation for breakthroughs in energy and information technologies.

Z. L. Wang, *Contact-Electrification of Matter*, Springer Series in Surface Sciences 75,
https://doi.org/10.1007/978-3-031-88504-4_7

7.1 Introduction

The phenomenon of contact electrification (CE) at liquid-solid interfaces has become a cornerstone of modern interfacial science, with the electrical double layer (EDL) theory serving as its foundational framework. Over nearly two centuries, the EDL model has evolved from basic conceptualizations to sophisticated formulations that underpin a myriad of technological applications. These advancements have reshaped our understanding of interfacial charge dynamics across conductors, dielectrics, and semiconductors in liquid CE systems. The origins of EDL theory can be traced to Helmholtz in the nineteenth century [1], who proposed a model likening interfacial charge distribution to a parallel-plate capacitor. While this provided an initial understanding, it failed to account for ion thermal motion and diffusion, limiting its applicability to dynamic systems. In the early twentieth century, Gouy and Chapman independently introduced the concept of a diffuse layer [2, 3], refining the understanding of charge distribution. This insight highlighted the dynamic nature of interfacial phenomena but overlooked finite ion sizes and specific adsorption effects. The Gouy-Chapman-Stern (Stern) model [4], introduced in 1924, addressed these limitations by combining the strengths of prior models. It divided the EDL into the Stern layer and the diffuse layer, with the Stern layer further subdivided into the Inner Helmholtz Plane (IHP) and Outer Helmholtz Plane (OHP). Beyond these regions lay the diffuse layer, where free ions moved under the influence of electrostatic forces and thermal energy. This comprehensive model provided a robust framework for understanding charge distribution at liquid-conductor interfaces and has remained invaluable for applications in energy storage, chemical sensing, and other advanced technologies.

Traditional EDL models primarily focused on liquid-conductor interfaces, leaving the complexities of liquid-dielectric systems less explored. Wang et al. bridged this gap by performing thermionic emission experiments across various liquid-dielectric systems [5], revealing critical nanoscale insights into charge transfer mechanisms. These studies demonstrated that interfacial charge exchange involves both electron transfer and ionization reactions, with their relative contributions shaped by the surface chemistry of the dielectric and the liquid's properties. Wang et al. proposed a two-step EDL model for liquid-dielectric interfaces [6]. In the initial step, electron transfer occurred due to the overlap of atomic electron clouds between the solid and liquid molecules. Concurrently, surface ionization reactions generated electrons and ions depending on the material's chemical properties and the liquid's ionization potential. In the subsequent step, electrostatic forces drove counter-ions in the liquid to form a structured EDL similar to that at conductor interfaces. This refined model elucidated the interplay between electron transfer and ionization, advancing our understanding of interfacial behaviors between dielectric materials and liquids. The EDL serves as an ideal ionic-electronic coupling interface, enabling dynamic modulation of ion and electron behaviors in iontronics. Unlike traditional electronics, which rely on electrons or holes as charge carriers, iontronics facilitates the simultaneous manipulation of ionic and electronic charges, significantly

enhancing energy efficiency. For instance, the human brain, a highly integrated iontronic system, operates on approximately 12 W of power, whereas electronic systems replicating similar integration would require megawatts, underscoring the efficiency advantage of iontronics. Wei et al. advanced this field by dynamically regulating EDL properties using the triboelectric charge from CE [7, 8]. This innovation led to the development of triboiontronics, which leveraged the interaction between triboelectricity and iontronics to precisely control ionic-electronic coupling interfaces. The dynamic modulation of charge carriers within the EDL enabled highly efficient energy harvesting and information flow, paving the way for groundbreaking applications in interface control, biosensing, and human-computer interaction.

From Helmholtz's initial parallel-plate capacitor model to Wang's two-step EDL model, the evolution of EDL theory at liquid-solid interfaces reflects a journey of profound scientific advancement. These developments have not only deepened our understanding of interfacial charge dynamics but also unlocked transformative applications across energy and information technologies. By continuing to refine these models and integrate emerging insights, the field of CE at liquid-solid interfaces stands poised to address critical challenges in sustainable energy and advanced information systems for the post-Moore era.

7.2 Electrical Double Layer

The L-S contact interface is a critical boundary governing interfacial dynamics between liquids and solids, forming the basis for diverse physical, chemical, and electrochemical processes in catalysis, corrosion, energy scavenging and sensors etc. Upon contact, differences in electrochemical potential and surface properties, such as electronegativity, surface energy, and roughness, drive charge redistribution, facilitating L-S CE. This charge redistribution governs the formation of the EDL, which in turn affects ionic transport kinetics, reaction rates, and colloidal stability, while driving key phenomena such as ion adsorption, surface reactivity, and electrostatic interactions. These functions are vital for applications in capacitive energy storage, electrochemical sensing, and advanced separation technologies. Dynamic regulation of the EDL via electric fields or mechanical methods enables control over charge carrier behavior, optimizing ion migration and charge concentrations at the interface. This capability directly enhances energy scavenging, storage, sensors, and information flow processes, underscoring the transformative potential of EDL engineering in advancing interfacial science and practical applications.

At the interface of L-S CE, EDL theory has been refined over nearly two centuries, advancing from foundational models to sophisticated frameworks with broad technological applications [9]. It originated with Helmholtz in the nineteenth century, who conceptualized interfacial charge distribution as a parallel-plate capacitor [1] (Fig. 7.1a). In this model, a rigid layer of counter-ions formed near the charged solid surface, balanced by an opposing charge on the solid. While groundbreaking, the Helmholtz model failed to account for ion thermal motion and diffusion, limiting

its ability to describe the EDL's dynamic behavior. In the early twentieth century, Gouy and Chapman independently extended the understanding of interfacial charge distribution by introducing the concept of the diffuse layer [2, 3] (Fig. 7.1b). They proposed that, in addition to ions accumulating near the contact surface, some ions diffuse into the bulk solution, forming a region where ion concentration follows a Boltzmann distribution. It resulted in an exponential decay of charge density with increasing distance from the interface. This dynamic representation marked a significant improvement but overlooked factors such as finite ion sizes and specific adsorption effects, which were critical to accurately describing interfacial phenomena. To address these limitations, Stern introduced the Gouy-Chapman-Stern (Stern) model in 1924 [4] (Fig. 7.1c), which integrated the strengths of both Helmholtz and Gouy-Chapman approaches. This model divided the EDL into two regions: the Stern layer and the diffuse layer. The Stern layer is further subdivided into the IHP and the OHP. The IHP was composed of specifically adsorbed ions and solvent molecules, influenced by electrostatic and chemical interactions, while the OHP contained solvated ions interacting with the surface primarily through long-range electrostatic forces. Beyond the Stern layer lies the diffuse layer, where free ions are governed by electrostatic forces and thermal motion. Together, these layers define the EDL's spatial structure, with their combined thickness approximating the Debye length, a key parameter determining ionic interaction strength in solution. The Debye length varied with electrolyte concentration and the dielectric constant of the medium, ranging from 0.2 to 20 nm under typical conditions. The Stern model has proven invaluable for understanding charge distribution at L-S contact interfaces. By synergizing the interactions among electrostatic forces, ion adsorption, and thermal dynamics, this model has continued to guide the development of advanced technologies, including energy storage, chemical sensing, and beyond, reaffirming its enduring relevance in both foundational research and practical innovation.

The classical models of EDL primarily emphasized charge distribution at liquid-conductor interfaces, often neglecting the complex interactions at liquid-non-conductor interfaces. To bridge this gap, Wang et al. performed thermionic emission experiments across various liquid-dielectric systems, offering critical nanoscale insights into charge transfer mechanisms [5]. These experiments revealed that charge exchange at the liquid-dielectric interface involves both electron transfer and ionization reactions, with their relative contributions influenced by the material's surface properties and the liquid's characteristics. Specifically, at liquid-hydrophobic dielectric interfaces, electron transfer dominated due to the limited occurrence of ionization reactions, as the solid surface lacked sufficient affinity for dissociating liquid molecules. In contrast, at liquid-hydrophilic dielectric interfaces, ionization reactions played a more significant role, enabling ions to mediate charge transfer processes more effectively. Based on these findings, Wang et al. proposed a two-step EDL model that extended traditional EDL concepts to liquid-dielectric interfaces [6] (Fig. 7.2). In the first step, when a liquid came into contact with a pristine dielectric surface, electron transfer occurred due to the overlap of atomic electron clouds between the solid and water molecules. Concurrently, surface ionization reactions might generate both electrons and ions, depending on the material's chemical properties and the

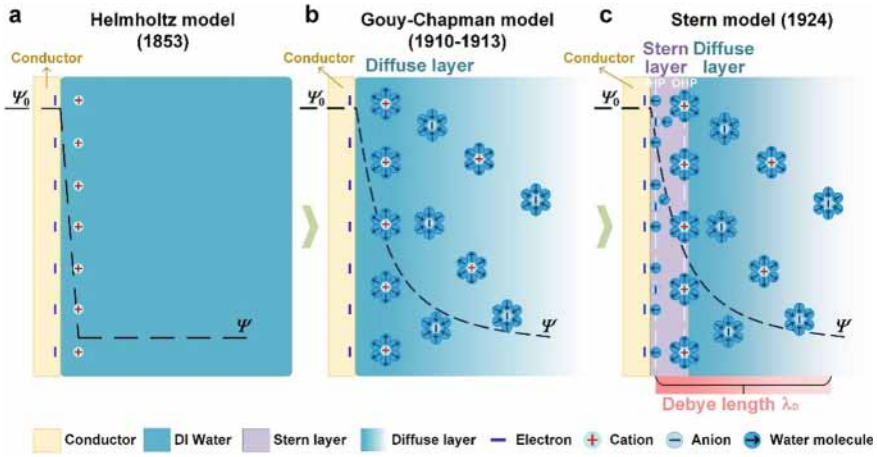

Fig. 7.1 The evolution of the EDL model at liquid-conductor interfaces. **a** The Helmholtz model. **b** The Gouy-Chapman model. **c** The Stern model. With permission from Wiley-VCH GmbH (2024) [9]

liquid's ionization potential. In the second step, electrostatic forces drive counterions in the liquid toward the charged solid surface, forming a structured EDL similar to that observed at conductor interfaces. This refined model enhanced the understanding of the EDL structure at non-conductor interfaces, particularly by elucidating the interplay between electron transfer and ionization in shaping interfacial charge distributions. The model also highlighted the critical role of surface chemistry and liquid properties in defining interfacial behaviors, with significant implications for applications in dielectric materials, energy storage devices, and environmental engineering.

The EDL served as an ideal ionic-electronic coupling interface in the field of iontronics, enabling the dynamic modulation of ion and electron behaviors. Unlike traditional electronics, which relied primarily on electrons and/or holes as charge carriers, iontronics facilitated the simultaneous manipulation of ionic and electronic charges, offering the potential for significantly enhanced energy efficiency [10]. For example, the human brain, a highly integrated iontronic system, operates on approximately 12 W of power. In contrast, replicating brain-like integration with electronic systems could demand tens of megawatts of energy [11], illustrating the efficiency advantage of iontronics. In this context, the EDL played a pivotal role by enabling the transport and reorganization of ions to modulate electronic properties, presenting a promising paradigm for achieving efficient energy and information flow, an essential feature for next-generation technologies in the post-Moore era [12]. Recently, the dynamic regulation of charge carriers within the EDL at liquid-dielectric interfaces by the triboelectric charge from CE was demonstrated by Wei et al. [7], as illustrated in Fig. 7.3. This breakthrough led to the development of triboiontronics, which leveraged the interplay between triboelectricity and

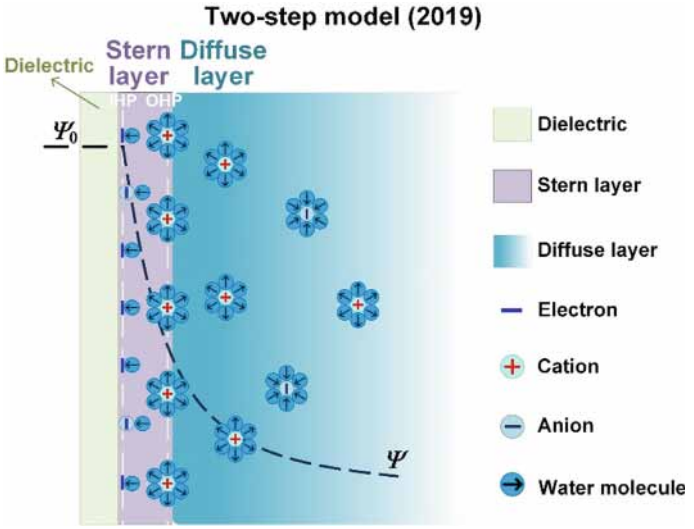

Fig. 7.2 The two-step EDL model at the liquid-dielectric interface was proposed by Wang et al. With permission from Wiley-VCH GmbH (2024) [9]

iontronics to precisely control the ionic-electronic coupling interface. This innovative approach enabled highly efficient energy scavenging and information flow by dynamically regulating EDL properties. The effective modulation of ionic and electronic charge carriers paved the way for controllable ionic-electronic information flow, unlocking new applications in interface control, biosensing, and human-computer interaction. These advancements underscored the transformative potential of triboiontronics across diverse fields, driving the seamless integration of ionic and electronic systems for next-generation energy and information technologies.

7.3 Contact Electrification at Liquid-Conductor Interfaces

Charge transfer at the liquid-conductor interface plays a crucial role in electrochemical processes, governing the movement of electrons between the conductive material and the surrounding electrolyte. This interaction is fundamental to processes such as electrolysis, corrosion, and energy storage. At the interface, the electrochemical potential difference between the liquid (electrolyte) and conductor (electrode) drives the transfer of charge, resulting in the formation of an EDL, which regulates ion and electron movements. In electrochemistry, the liquid-conductor interface is central to processes like oxidation and reduction reactions, where electrons are transferred between the solid electrode and the liquid phase. The rate of charge transfer depends on the nature of the electrode surface, its reactivity, and the ionic composition of the electrolyte. Additionally, the interface reaction is governed by the Nernst equation,

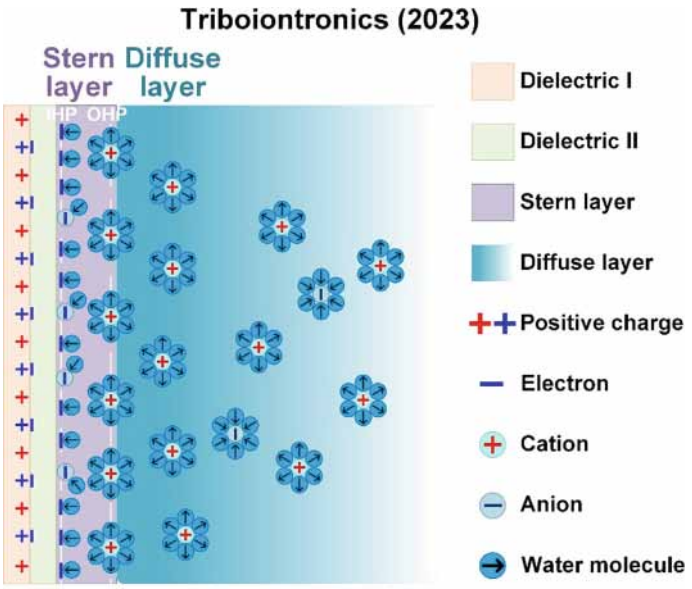

Fig. 7.3 Triboiontronics based on dynamically regulating the EDL at liquid-dielectric interfaces. With permission from Wiley-VCH GmbH (2024) [9]

which relates the electrode potential to the concentration of ions in the solution, and the Butler-Volmer equation, which describes the kinetics of electron transfer reactions. The efficiency of charge transfer at the liquid-conductor interface influences the overall performance of electrochemical devices such as batteries, capacitors, and sensors. Enhanced charge transfer can improve the power and energy densities of storage devices, while a better understanding of the interface dynamics can optimize electrochemical sensing for applications in chemical analysis, environmental monitoring, and medical diagnostics.

7.3.1 Supercapacitors

Since Helmholtz introduced the concept of the EDL, it has become a cornerstone in understanding electrochemical processes. The EDL effect facilitates the formation of a highly concentrated ion-electron layer at the electrode surface, providing a robust mechanism for energy storage. This principle is foundational to the design of EDL supercapacitors, a classical electrochemical energy storage device that leverages the EDL effect to deliver high power density and rapid charge-discharge capabilities as shown in Fig. 7.4. These characteristics make supercapacitors a critical component in modern energy systems. Unlike traditional capacitors, which rely primarily on dielectric materials for charge storage, supercapacitors accumulate a substantial

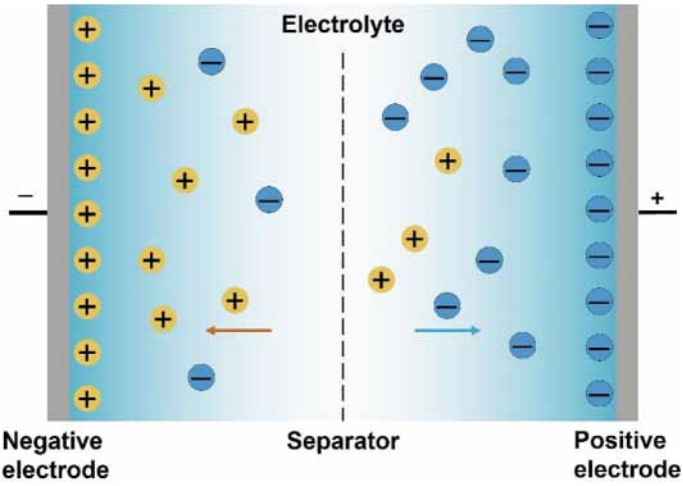

Fig. 7.4 Working mechanism and structure of supercapacitors based on EDL

amount of ionic charge directly within the interface layer. This physical process, free from chemical reactions, enables supercapacitors to sustain their performance over thousands of charge-discharge cycles. Such a unique mechanism grants supercapacitors significant advantages in power density, and cycle life, positioning them as indispensable in applications where rapid charging and long-term durability are paramount [13].

EDL supercapacitors arose in the mid-twentieth century, driven by advances in EDL theory and electrochemical materials, with prototypes employing activated carbon electrodes and aqueous electrolytes. [14]. By the 1970s, supercapacitors began to be used in industrial applications, but early devices were limited by low energy and power densities. Late in the twentieth century, advances in high-surface-area carbon materials and gel electrolytes significantly enhanced performance. The twenty-first century ushered in a new phase, with nanomaterials technology accelerating supercapacitor development. The introduction of novel electrode materials, such as graphene and carbon nanotubes, markedly improved device performance and expanded application potential. Today, supercapacitors are integral to energy-intensive sectors, from transportation to wearable electronics, cementing their role as key components in modern energy systems. In recent years, extensive modifications to electrode materials, electrolytes, and asymmetric electrode configurations have been pursued to enhance supercapacitor performance [15]. The efficiency of supercapacitors is highly dependent on the properties of electrode materials, including specific surface area, conductivity, and pore structure, which directly influence the EDL's effective surface. Notably, metal oxides like MnO_2 and RuO_2 function as pseudocapacitive materials, adding Faradaic reactions to conventional EDL charge storage, thereby significantly enhancing energy density [15]. Second, electrolytes are equally critical to achieving

high energy and power densities in supercapacitors. Conventional aqueous electrolytes offer high ionic conductivity and low cost, but their narrow electrochemical window, limited by water decomposition at elevated voltages, restricts energy density. As a result, organic electrolytes and ionic liquids have emerged as key alternatives to extend the electrochemical window. Organic electrolytes, with electrochemical windows up to 2.5–3 V, significantly enhance energy density, while ionic liquids, recognized for their wide electrochemical window, low vapor pressure, and chemical stability, excel in high-voltage applications. They improve ion concentration at the electrode-electrolyte interface, thereby enhancing capacitance and charge-discharge efficiency. Optimizing the surface and structural characteristics of electrodes to enhance charge storage has become a critical area of focus. Functional groups, such as hydroxyl and carboxyl, improve electrode hydrophilicity, facilitating efficient ion penetration and adsorption. Nanostructural modifications, including porous or layered architectures, significantly increase the specific surface area and shorten ion diffusion pathways, thereby maximizing charge storage density. These structural enhancements directly influence EDL processes: the expansion of the electrode surface area generates additional double layers, thereby augmenting charge storage capacity, while the use of advanced electrolytes extends the voltage window, enabling higher energy density within the same volume. Moreover, modifications to the physicochemical properties of the electrode interface optimize ion mobility, thereby improving the kinetics of EDL charge and discharge processes and resulting in enhanced power density.

Supercapacitors hold significant promise across renewable energy, transportation, and consumer electronics sectors, where their high power density, rapid response, long cycle life, and environmental compatibility have positioned them as pivotal components in modern energy systems. Unlike traditional batteries, supercapacitors excel in delivering bursts of high power within short durations, making them ideal for applications such as starting mechanisms and energy recovery systems in electric vehicles. In renewable energy setups like TENG, photovoltaic, and wind power systems, supercapacitors serve a vital role in smoothing power fluctuations, thereby enhancing overall stability and reliability [16]. As a highly efficient energy storage solution, supercapacitors are poised to play a transformative role in future low-carbon and intelligent energy infrastructures, aligning with global shifts toward sustainable and resilient power systems.

7.3.2 Various Types of Electrochemical Sensors

Electrochemical sensors utilizing the EDL have emerged as a versatile and promising technology across various applications, from environmental monitoring to implantable biomedical devices. These sensors exploit the distinctive properties of the EDL at the interface between conductors and ionic materials to convert physical or chemical variations into electrical signals with remarkable sensitivity and stability. Based on their structural design, EDL-based sensors can be categorized

into two primary types: EDL capacitive sensors and EDL electrode sensors, both of which have shown significant potential in overcoming challenges across diverse fields.

7.3.2.1 EDL Capacitive Sensors

The EDL capacitive sensor typically consists of two conductors and an ionic material arranged in a cavity or sandwich structure, as illustrated in Fig. 7.5. It exploits EDL capacitance effects to transduce external physical or chemical variations, such as pressure, strain, and temperature, into electrical signals [17]. These sensors rely on the EDL properties at the interface to detect changes in capacitance or impedance, with ionic materials rich in mobile ions serving as the critical components. Unlike traditional parallel-plate capacitors, EDL capacitive sensors utilize ion modulation mechanisms, offering enhanced sensitivity and resistance to interference. This makes them particularly suitable for high-resolution, wide-dynamic-range applications.

EDL capacitive sensors are increasingly pivotal in the sensing domain due to their exceptional sensitivity, resistance to interference, and rapid response times. In smart wearables and portable medical devices, these sensors can detect subtle pressure variations, facilitating health monitoring and motion analysis, and providing reliable support for real-time human signal monitoring. In environmental monitoring, the interference-resistant ion modulation mechanism of EDL capacitive sensors enables precise signal detection in complex electromagnetic environments. As advancements in ionic materials and structural designs continue, the application scope of EDL capacitive sensors expands, particularly in emerging areas such as smart materials, flexible electronics, and adaptive control systems. With ongoing progress in materials science and micro-nano manufacturing technologies, the performance and multifunctionality of EDL capacitive sensors will further improve, driving innovations in intelligent, portable, and multifunctional sensing devices.

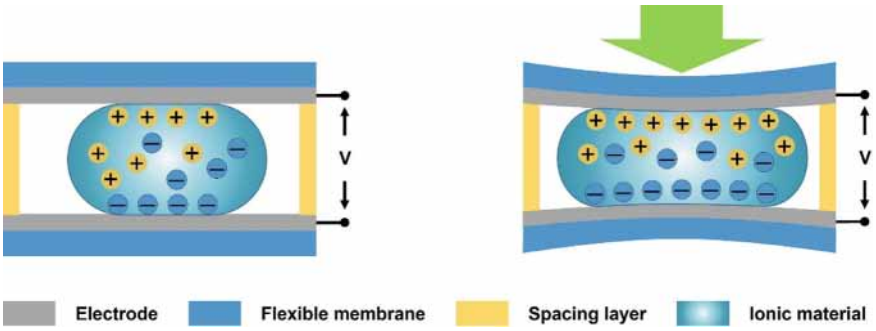

Fig. 7.5 Typical mechanism and structure of the EDL capacitive sensors

7.3.2.2 Implantable Sensors Based on EDL

The challenge of facilitating direct charge exchange between electronic electrodes and ion-regulated biological systems has highlighted the limitations of traditional conductive electrodes in implantable medical sensors and devices [18]. Such electrodes can cause electrochemical reactions at the electrode-tissue interface, leading to tissue damage through local pH shifts, heat generation, and hydrogen ion accumulation [19]. Implantable electrodes based on the EDL interface, typically consisting of a conductive electrode and an interfacial ionic gel as shown in Fig. 7.6, based on the EDL interfacial charge transfer mechanism have recently emerged as a promising solution. It leverages EDL effects to enable controlled ion transport and charge modulation at the interface between electrodes and biological tissues [20]. These ionic gels offer unique advantages in biocompatibility, stability, and signal transmission [21], making them an increasingly crucial technology in implantable devices, including pacemakers, neurostimulation electrodes, and brain-machine interfaces. Thus, it can establish an efficient charge transmission between the electrode and the biological tissue, enhance the biocompatibility of the electrode and make the signal stable and accurate.

Early explorations of EDL electrode interfaces in biology trace back to Luigi Galvani's seminal concept of "animal electricity" in the late eighteenth century [22], with implantable electrode technology achieving pivotal advancements by the mid-twentieth century. Milestones included the development of cardiac pacemakers and spinal stimulators by Medtronic in the 1960s, where the role of electrode capacitance in facilitating charge transfer across electrode-tissue interfaces was first realized [22]. In 1978, the cochlear implant, a platinum electrode array implanted in the cochlea, converted acoustic signals to electric pulses, marking a breakthrough in auditory prosthetics. In 2002, deep brain stimulation was approved for the treatment of Parkinson's disease. Implantable electrodes can also selectively identify and transmit electrical signals from specific biomolecules, such as glucose and lactic acid, and are widely used in the monitoring of diseases such as diabetes and Rheumatoid Arthritis. After that, with the rapid development of bioelectronics and ionic gel materials, EDL ionic

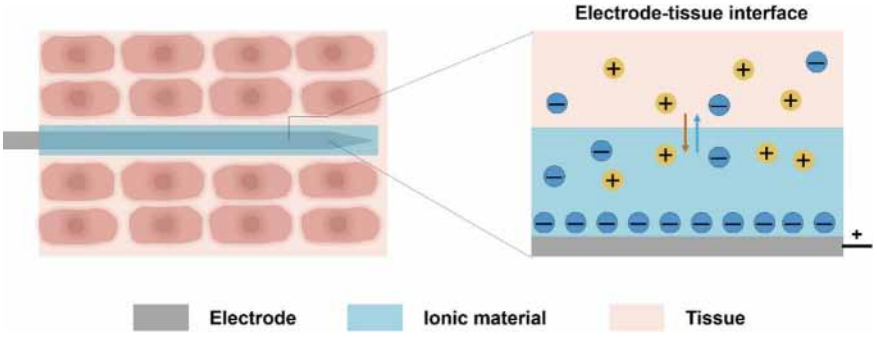

Fig. 7.6 Schematic of insertion of an EDL electrode sensor inside the tissue

gel technology has been widely used in electrical stimulation electrodes and brain-computer interfaces because of their biocompatibility and flexibility. Especially in the field of nerve repair, and muscle regeneration, by forming an EDL between the ionic gels and surrounding tissue, these gels establish efficient electrical signal pathways, enabling bioelectronic signal transduction while minimizing the risk of tissue damage. While in the field of brain-computer interface, the ionic gels can accurately convey brain signals to electronic systems, playing a critical role in intelligent prosthetic control and electroencephalogram [23]. To ensure optimal EDL performance in complex biological environments, researchers have incorporated a variety of modifications to enhance the biocompatibility, conductivity, mechanical durability, and surface properties of ionic gels. For example, natural polymers like alginate, gelatin, and chitosan, as well as bio-compatible conductive polymers such as polythiophene, polypyrrole, and PEDOT, have been utilized to optimize electrode safety. Mechanical stability has been improved by integrating cross-linking agents or layered structures within the gels to create support networks that withstand stretching and twisting forces. For applications requiring high conductivity, functional nanomaterials such as carbon nanotubes, graphene, and gold nanoparticles are added to enhance signal transmission and responsiveness. In short-term or transient implants, biodegradable polymers like poly(lactic-co-glycolic) acid (PLGA) reduce the need for removal surgery, minimizing patient discomfort and risk.

In summary, implantable electrodes based on EDL are positioned at the forefront of biomedical engineering, underpinning a new class of implantable devices that achieve higher signal fidelity, biocompatibility, and functional versatility. As material science and bioelectronics continue to advance, EDL technology is expected to play an increasingly vital role in personalized healthcare, providing precise and efficient solutions for diagnostics, therapeutic interventions, and human-machine interaction.

7.3.2.3 Electrocatalysis Based on EDL

Electrocatalysis plays a pivotal role in material recycling, environmental protection, and clean energy conversion, attracting significant attention for its capacity to efficiently convert molecules or ions into high-value products under mild conditions. While redox reactions dominate the electrode interfacial dynamics in electrocatalysis, increasing evidence highlights the significant impact of the structure and composition of the EDL at the electrode interface. Interactions with surface charges significantly affect charge distribution and the electric field within the interfacial electrolyte [24, 25]. These effects further regulate interfacial properties, including charge distribution, interfacial dielectric constant, solvent network structure, and local pH, thereby exerting effective kinetic and thermodynamic control over electrocatalytic reactions. Generally, at potentials below the point of zero charge (PZC), hydrogen atoms in water molecules within the IHP orient toward the electrode surface, enabling proton adsorption. At potentials above the PZC, oxygen atoms in water molecules within the IHP face the surface, facilitating the specific adsorption of anions. At even higher potentials, substantial adsorption of hydroxide ions and the formation of surface oxide

species occur. On the other hand, electrolyte cations with large hydration shells are believed to reside in the outer Helmholtz plane (OHP). Hydrated cations can influence surrounding water molecules and adsorption structures through non-covalent interactions, such as ion-dipole, dipole-dipole, and hydrogen bonding interactions [26]. The interface structure mediated by cations, including the electrode surface, water, and adsorbed species, is crucial for understanding high-performance electrocatalytic systems [27]. Recent studies have demonstrated that the EDL effect plays a pivotal role in various electrocatalytic reactions. For instance, in the hydrogen evolution reaction (HER) and oxygen evolution reaction (OER), as shown in Fig. 7.7, the EDL influences the reaction rate by modulating local ion or molecule concentrations. In the oxygen reduction reaction (ORR), the EDL stabilizes intermediates, enhancing reaction efficiency. In carbon dioxide reduction reactions (CO_2RR), the EDL regulates the adsorption of CO_2 molecules and the selectivity of products. Similarly, in nitrogen reduction reactions (NRR), the EDL facilitates the activation of reactants. These findings underscore the critical role of the EDL in electrocatalysis, providing new insights and directions for optimizing catalytic performance.

Electrocatalysis, as a scientific discipline, has undergone significant development since its origins in the late 19th and early twentieth centuries [28]. The early development of electrocatalysis centered on quantitative evaluations of reaction rates at electrode interfaces, exemplified by Bowden and Rideal's 1928 studies, which analyzed electrocatalytic activity through current densities at defined potentials. Frumkin later advanced the field by introducing reaction rate constants influenced by the· EDL, providing a formalized framework [29]. Historically, the hydrogen evolution reaction (HER) served as a foundational model for electrocatalytic investigations [30–32]. By the early twentieth century, industrial applications, such as chlorine and hypochlorite production, began to utilize electrocatalysis, with early catalysts like

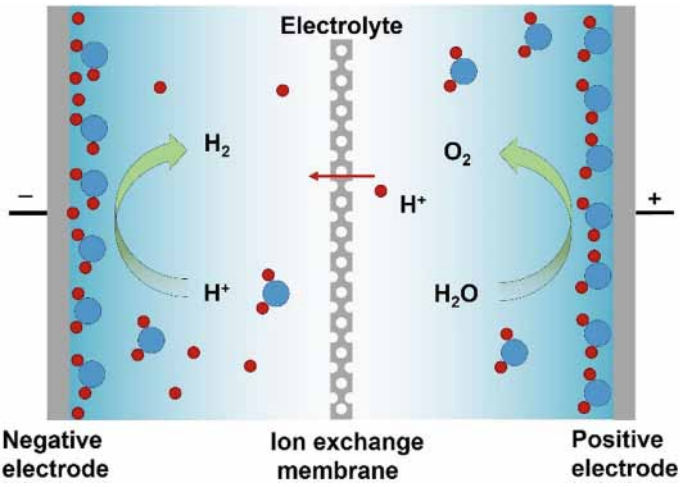

Fig. 7.7 Schematic of HER and OER electrocatalysis

platinized platinum offering enhanced surface area and activity. Groundbreaking work by scientists like Tafel and Haber during this period established key principles, including the relationship between overpotential and catalytic efficiency [33, 34]. The term "electrocatalysis" was formally introduced in the 1930s by researchers like Kobosew and Monblanowa, who investigated the correlation between hydrogen-metal bond energy and catalytic overpotentials [35]. This era also marked the introduction of model systems and the utilization of single crystals, enabling the investigation of catalytic properties under controlled conditions [36, 37]. By the mid-twentieth century, advancements in nanomaterials and surface science catalyzed further progress. Today, electrocatalysis encompasses diverse applications ranging from fuel cells and electrolyzers to carbon dioxide reduction and water splitting. The field has evolved to integrate complex catalysts, computational modeling, and advanced in situ characterization techniques, ensuring its continued relevance in addressing modern energy and environmental challenges.

Significant advancements in electrocatalysis have been achieved through innovations in materials, surface engineering, and system optimization, addressing the challenges of efficiency, selectivity, and durability. At the heart of many of these advancements is the EDL, whose structure and dynamics at the electrode-electrolyte interface play a critical role in determining catalytic performance. By tailoring materials and interfaces to modulate the EDL, researchers have achieved significant improvements in catalytic efficiency and stability. Material innovations, such as nanostructured catalysts and multi-element alloys, have enhanced catalytic activity by increasing active site density and tailoring electronic properties. For example, transition metal oxides, 2-dimensional (2D) materials like graphene and MXenes, and alloyed systems create enhanced electronic environments that influence the EDL by modulating surface charge density and local electric fields. Surface modifications, including doping and functionalization, have further optimized the binding strength of reaction intermediates and improved interfacial interactions. Doping introduces heteroatoms into the catalyst lattice, altering the local electronic structure and influencing the EDL by redistributing charge at the interface. Similarly, functional groups like hydroxyl (–OH) or amine (-NH_2) groups improve the hydrophilicity of the surface, promoting efficient ion transport within the EDL and thereby enhancing mass transfer and catalytic efficiency. The development of advanced support materials, such as carbon-based frameworks and corrosion-resistant metal oxides, has stabilized active sites and ensured structural integrity during operations. Electrolyte engineering, with the introduction of ionic liquids and polymer electrolytes, has expanded operational windows and improved charge transfer efficiency through the stabilization of the EDL. In situ and operando characterization techniques, such as X-ray absorption spectroscopy and surface-enhanced Raman spectroscopy, have elucidated intermediate stabilization mechanisms and reaction kinetics, informing the rational design of advanced catalysts. Additionally, strategies such as alloying, strain engineering, and protective coatings have addressed catalyst degradation, ensuring long-term stability under operational conditions. Together, these advancements have significantly improved the efficiency and resilience of electrocatalysts, positioning them as key enablers of

sustainable energy technologies such as fuel cells, electrolyzers, and CO_2 reduction systems.

Overall, the EDL, as a fundamental mechanism connecting interfacial chemistry with electrocatalytic processes, offers distinct advantages in enhancing electrocatalytic performance by modulating ion distribution, electric field intensity, and solvent environments. It has become integral to electrocatalysis research, underpinning advancements in green energy technologies such as fuel cells and triboelectrocatalysis [38]. With continued progress in advanced characterization methods and theoretical simulations, the precise control of EDL effects is poised to evolve further. Future endeavors will focus on leveraging these effects in increasingly complex and efficient electrocatalytic systems, propelling innovations in clean energy and sustainable technologies.

7.3.3 The Tribovoltaic Effect at Water-Metal Interfaces

When water interacts with a metal surface, beyond traditional electrochemical applications where EDLs are regulated by external electric fields, the tribovoltaic effect, driven by the Schottky junction, can also arise in the absence of external fields. The tribovoltaic effect at solid semiconductor-metal interfaces was first discovered by Wang et al. in 2020 [39]. The study demonstrated that a Schottky junction formed when a high-work-function metal was in static contact with n-type Si, characterized by a lower work function. This interaction facilitated electron transfer from the semiconductor to the metal, creating a built-in electric field. During sliding, frictional energy released through bond formation excited non-equilibrium carriers, such as electron-hole pairs in the semiconductor's space charge region and electrons in the surface states of both the metal and the semiconductor. Driven by the built-in electric field, these carriers drifted, producing a steady output in the external circuit.

In the tribovoltaic effect observed at water-metal interfaces explored by Wang et al. in 2020 [41], deionized (DI) water was considered analogous to a wide-band gap semiconductor. As illustrated in Fig. 7.8a, the Fermi level of the metal was lower than that of DI water. Upon contact, a built-in electric field was established to equalize the Fermi level difference, as shown in Fig. 7.8b. In solid-solid (S-S) Schottky junctions, the depletion region was always located on the semiconductor side. Similarly, at DI water-metal interfaces, the depletion region is formed on the DI water side. Recent experimental studies have confirmed the presence of the tribovoltaic effect at DI water-metal interfaces, highlighting its potential for energy scavenging and sensing applications. These findings suggested that interfacial charge dynamics in liquid-metal systems could play a significant role in developing next-generation technologies.

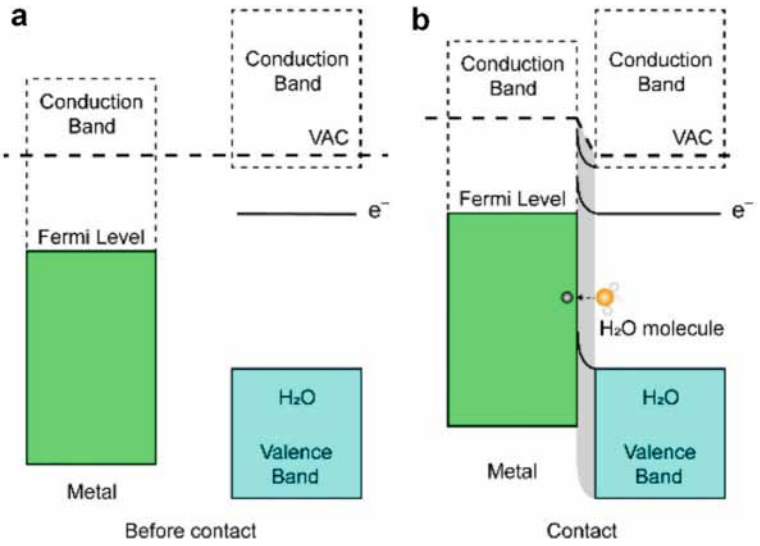

Fig. 7.8 The tribovoltaic effect observed at water-metal interfaces. **a** The Fermi level of the metal was lower than that of DI water. **b** Upon contact, a built-in electric field was established to equalize the Fermi level difference. With permission from American Chemical Society (2022) [40]

7.4 Contact Electrification at Liquid-Dielectric Interfaces

7.4.1 Quantifying Ion Transfer and Electron Transfer

In the context of the EDL at liquid-conductor interfaces, it was commonly assumed that the primary charge carriers were ions, as liquids typically contain ion species like H^+ and OH^- or other species. The EDL at the liquid-solid interface has traditionally been attributed to the ionization or dissociation of surface functional groups and the adsorption of ions from the liquid onto the solid surface. However, Wang et al. proposed an innovative "electron-cloud-potential-well" model in 2018 [6, 42], as illustrated in Fig. 7.9, which broadened the understanding of charge exchange processes beyond the conventional S-S CE framework. This model suggested that under mechanical stress, the electron clouds of two adjacent atoms could overlap significantly, reducing the potential barrier between them and facilitating electron transfer. Mechanical stress was critical for bringing the atoms into close proximity, thereby maximizing the overlap of their electron clouds and promoting electron transitions. This model has been extended to L-S interactions, where liquid molecules collide with atoms on a solid surface due to liquid pressure. Such collisions may enhance the overlap of electron clouds, enabling electron transfer at the interface. This perspective suggested that electron transfer, in addition to ion exchange, played a significant role in L-S CE. The ongoing debate surrounding the identity of charge carriers in L-S CE underscores a fundamental question in interfacial charge exchange

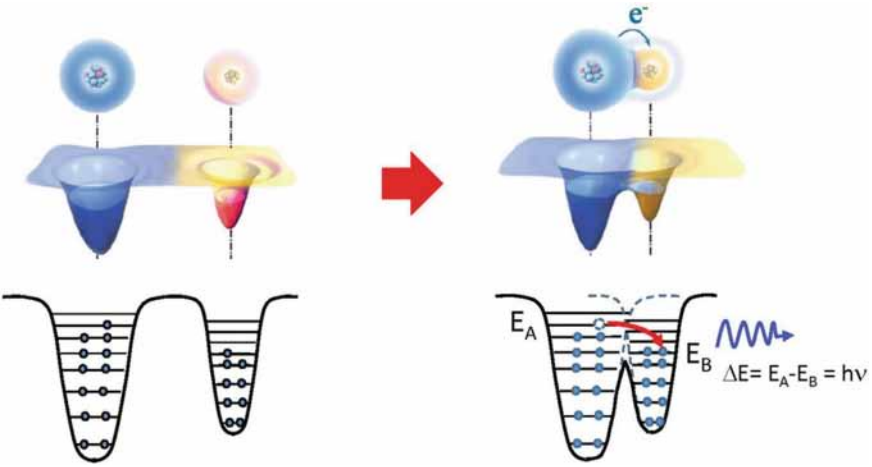

Fig. 7.9 The "electron-cloud-potential-well" model of L-S CE was proposed by Wang et al. With permission from Elsevier Ltd. (2019) [6]

and physical chemistry. Gaining deeper insights into the mechanisms governing charge transfer at these interfaces, including both ionic and electronic contributions, is crucial for advancing theoretical frameworks.

The attenuation of surface triboelectric charges via thermionic emission has been demonstrated as an effective approach to distinguish between electron and ion transfer in L-S CE. Lin et al. leveraged this principle by designing temperature-dependent charge decay experiments at the nanoscale in 2020 [5, 40, 43], employing Kelvin Probe Force Microscopy (KPFM) to quantitatively study CE processes between aqueous solutions and various insulating materials, such as SiO_2, Si_3N_4, and MgO (Fig. 7.10a). This methodology provided a comprehensive understanding of charge transfer dynamics at the L-S interface, shedding light on interfacial charge behavior. In the experiments, the initial surface charge density of insulating samples was measured using KPFM. Subsequently, a DI water droplet slid across the dielectric surface, facilitating charge transfer between the liquids and solid materials. The charges generated at the L-S contact interface might consist of either electrons or ions, with ions formed through ionization reactions on the oxide and nitride surfaces. After charge exchange, the dielectric was heated to a predetermined temperature (e.g., 513 K), enabling the thermionic emission of electrons as per thermionic emission theory [44, 45] (Fig. 7.10b). In contrast, ions chemically bonded to the dielectric's atoms underwent chemical adsorption, characterized by significantly higher detachment energy thresholds compared to electrons. For instance, detaching hydroxide ions (OH^-) from the SiO_2 surface requires approximately 8.5 eV, while removing protons (H^+) demands around 20 eV. These energy barriers indicate that chemically adsorbed ions are far more challenging to remove at moderate temperatures. The results revealed that SiO_2's initial surface charge density was nearly negligible. Upon water contact, negative charges were transferred from the liquid to the solid surface.

During heating, surface charge density decreased due to the thermionic emission of electrons. However, some charges remained post-heating, identified as "sticky" charges, corresponding to ions generated during the L-S CE process (Fig. 7.10c). With successive charging-heating cycles, the sticky charge density increased until reaching saturation, likely due to the limited number of available charge sites on the dielectric surface. As these sites became occupied by ions, the availability for further charge transfer decreased. Consequently, although both electrons and ions continued transferring to the surface, the number of transferred electrons diminished in subsequent cycles. Notably, initial contact was dominated by electron transfer, with a ratio exceeding 75%, reflecting the lower energy barrier and higher mobility of electrons compared to ions. This study highlights the nuanced interplay between electron and ion transfer at the L-S interface and advances the understanding of interfacial charge behaviors under different thermal and chemical conditions.

Temperature-dependent investigations of CE between DI water and various insulating materials revealed that surface charge density decays exponentially, consistent with thermionic emission principles. This decay pattern indicated the emission of electrons or holes from the material surface at elevated temperatures, helping clarify charge transfer mechanisms (Fig. 7.11a). For instance, materials such as MgO primarily exhibited an increase in positive surface charge density, attributed to the transfer of electrons to the solid surface during CE. Conversely, materials like Si_3N_4, HfO_2, Ta_2O_3, and AlN showed a decrease in positive charges due to the transfer of holes rather than electrons. This behavior highlighted a material-specific mechanism of charge reception during CE, which depended on their energy band structures and surface chemical properties. Negative surface charges arose from the transfer of electrons or negative ions, whereas positive charges originated from holes or positive ions. At elevated temperatures, thermionic emission could reduce surface charge density by releasing electrons and holes. However, exceptions such as MgO and Al_2O_3 display increased surface charge density over time. This phenomenon suggested that MgO absorbs both electrons and positive ions, while Al_2O_3 interacts with holes and negative ions. These differences stemmed from each material's specific surface adsorption properties and their ability to accommodate various charge species. The study also highlighted the role of surface hydrophilicity in charge transfer mechanisms (Fig. 7.11b). Hydrophilic surfaces, characterized by a water contact angle (CA) < 90°, form stronger interactions with water molecules, resulting in higher interfacial energy compared to hydrophobic surfaces (CA > 90°). These stronger interactions promoted the formation of covalent bonds between water molecules and surface atoms, facilitating ionization reactions at the interface and generating ions. In contrast, hydrophobic surfaces, with weaker water-solid interactions, were less likely to undergo ionization, leading to electron transfer dominating the CE process. One of the significant insights from this research was the apparent independence of electron transfer and ion transfer during L-S CE. While these processes may occur simultaneously, they are spatially segregated, with distinct regions of the surface facilitating different types of charge transfer. For hydrophilic materials, ion transfer was more pronounced due to stronger water-surface interactions, whereas hydrophobic materials favor electron transfer due to weaker molecular interactions.

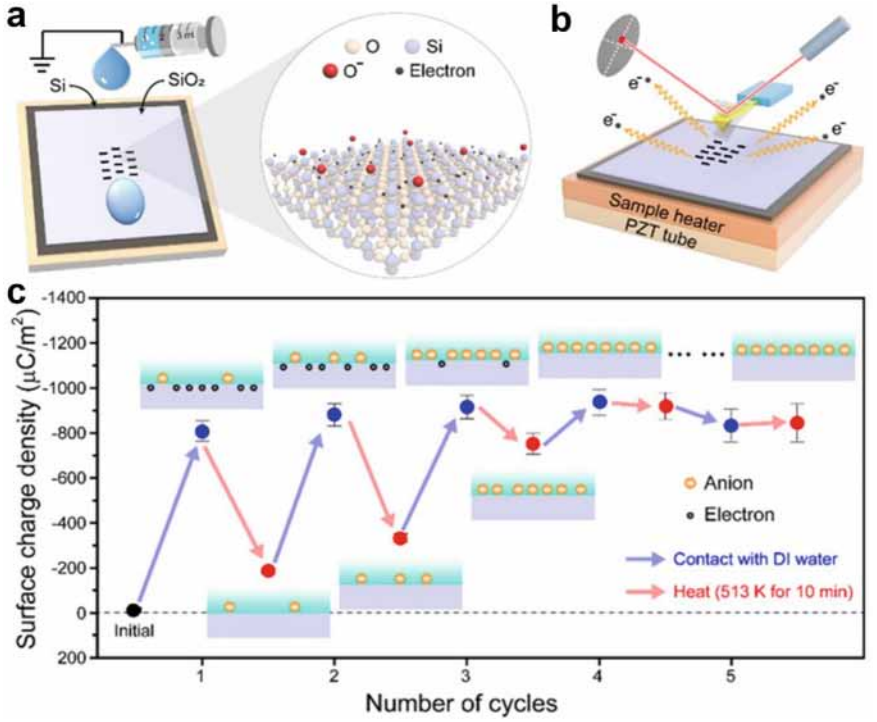

Fig. 7.10 The temperature-dependent charge decay experiments at the nanoscale were designed, employing KPFM to quantitatively study CE processes between aqueous solutions and various insulating materials. **a** A DI water droplet slid across the dielectric surface, facilitating charge transfer between the liquids and solid materials. **b** After charge exchange, the dielectric was heated to a predetermined temperature, enabling the thermionic emission of electrons as per thermionic emission theory. **c** During heating, surface charge density decreased due to the thermionic emission of electrons. However, some charges remained post-heating, identified as "sticky" charges, corresponding to ions generated during the L-S CE process. With successive charging-heating cycles, the sticky charge density increased until reaching saturation, likely due to the limited number of available charge sites on the dielectric surface. With permission from the authors (2020) [5]

These findings not only provided a deeper understanding of charge transfer dynamics but also offered practical guidance for designing and optimizing materials for electrochemical and energy-scavenging applications. By tailoring surface properties such as hydrophilicity, adsorption capacity, and thermal stability, it becomes possible to control charge transfer pathways, thereby improving the performance of CE-based systems across diverse environments and applications.

In addition to KPFM, Nie et al. developed a squeezing system in 2020 to investigate the electrification behavior at the L-S contact interface[46]. PTFE was selected as the insulating material due to its excellent chemical stability in both acidic and alkaline environments. In the experimental setup, a DI water droplet was positioned between two fluorine-doped tin oxide-coated PTFE (FTO-PTFE) substrates. The

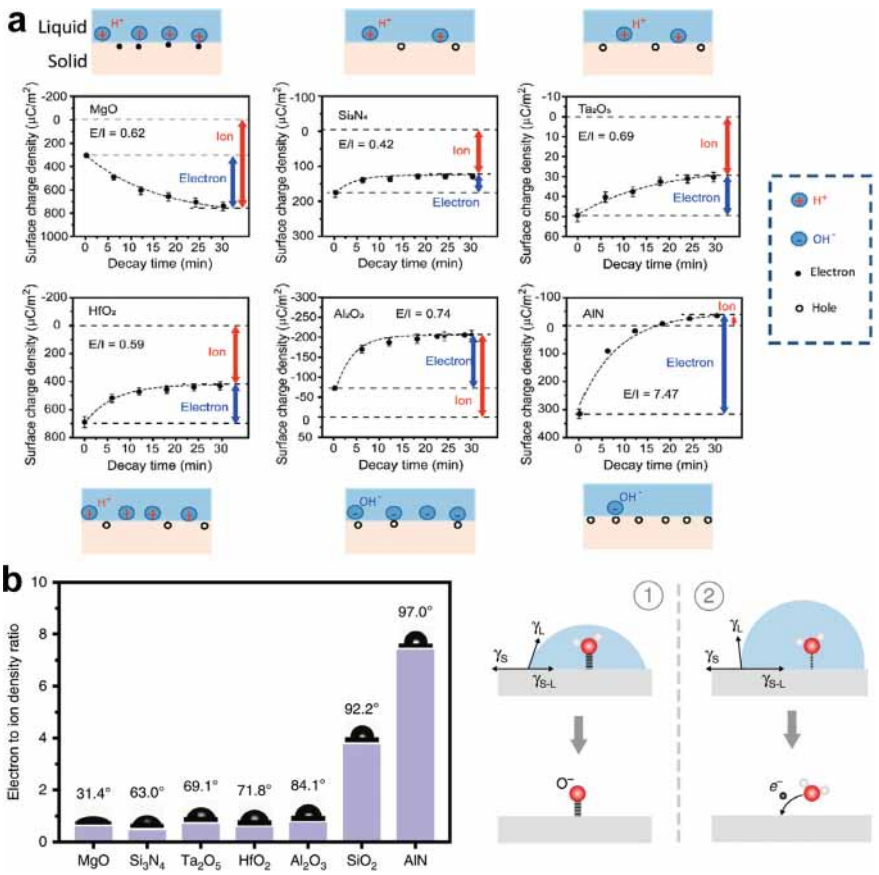

Fig. 7.11 The influence of dielectric materials properties on the L-S CE. **a** The comparative amounts of electron transfer and ion transfer during the CE process between DI water and various dielectric materials With permission from WILEY-VCH Verlag GmbH & Co. (2020) [43]. **b** The correlation between the ratio of electron transfer to ion transfer and the hydrophilicity of dielectric materials. With permission from the authors (2020) [5]

squeezing motion of the substrates was precisely controlled by a linear motor. As shown in Fig. 7.12a, the water droplet spread uniformly during compression, forming a thin liquid film and significantly increasing the contact area between the liquid and PTFE. After a contact-separation process, the triboelectric charge generated in the DI water droplet (50 μL) was measured, showing a positive correlation with the contact area, as depicted in Fig. 7.12b. To evaluate the contributions of electron transfer and ion adsorption to the total triboelectric charge, the authors performed a simplified calculation based on a pure ion adsorption model. Figure 7.12b also presented the calculated triboelectric charges under the assumption that the L-S CE was solely caused by ion adsorption. This calculation represented an ideal scenario

where all OH^- ions near the PTFE surface were adsorbed. However, several real-world factors, such as the inhibitory effects of H^+ ions, may suppress the adsorption of OH^- during experiments. Comparing the experimental results with the calculated values revealed that the calculated ion adsorption charge was over 10 times smaller than the experimental total triboelectric charge. This discrepancy indicated that ion adsorption alone could not account for the observed electrification and that electron transfer played a dominant role in the L-S CE process.

To further explore ion adsorption on the PTFE surface, solid-state ^1H nuclear magnetic resonance (NMR) spectroscopy was used to analyze changes in hydrogen signals after CE. As shown in Fig. 7.12c, a consistent peak around 0.7 ppm corresponded to primary alcohol ethoxylate (AEO, $RO(CH_2CH_2O)_nH$) in the PTFE dispersion. The water signal appeared near 4.8 ppm, with similar peak values observed for PTFE samples contacted with DI water, NaCl solution, and NaOH solution. However, the charge transfer after contact with DI water was significantly higher than those observed with NaCl or NaOH solutions, suggesting that ion adsorption alone cannot fully explain the CE process. Conversely, when PTFE was exposed to an acidic HCl solution, a prominent peak near 6.2 ppm was observed, indicative of substantial H^+ ion adsorption. This behavior highlighted that in acidic conditions, both electron transfer and ion adsorption occur, but the high concentration of H^+ ions suppresses electron transfer between water molecules and PTFE. These findings, corroborated by the proposed model in Fig. 7.12d, confirmed that both electron transfer and ion adsorption contribute to the L-S CE process. Ion adsorption, in particular, played a critical role in modulating the electrification behavior under acidic conditions.

7.4.2 The Wang's Two-Step EDL Model at Liquid-Dielectric Interfaces

The process of electron transfer at the L-S contact interface played a crucial role in the formation and dynamics of the EDL. To understand this phenomenon in depth, Wang et al. proposed a two-step model of the EDL in 2019 [5, 40], which reinterpreted the conventional concept of the EDL at liquid-dielectric interfaces. This model provided a comprehensive framework for understanding the charge transfer mechanisms that occur when a dielectric surface comes into contact with a liquid. In the first step of the model (Fig. 7.13a), upon contact with a liquid, various particles, including water molecules, cations, and anions, underwent thermal motion and pressure-driven collisions. These interactions promoted electron transfer between the solid's atomic structure and the surrounding liquid molecules. More specifically, the overlap of electron clouds between the solid surface and liquid molecules facilitated electron exchange. Concurrently, ionization reactions could occur at the contact interface, resulting in the simultaneous generation of electrons and ions. As electron transfer occurs on the timescale of picoseconds to nanoseconds, significantly faster than ion diffusion, it precedes ion movement. The electrons attract ions, with a portion being

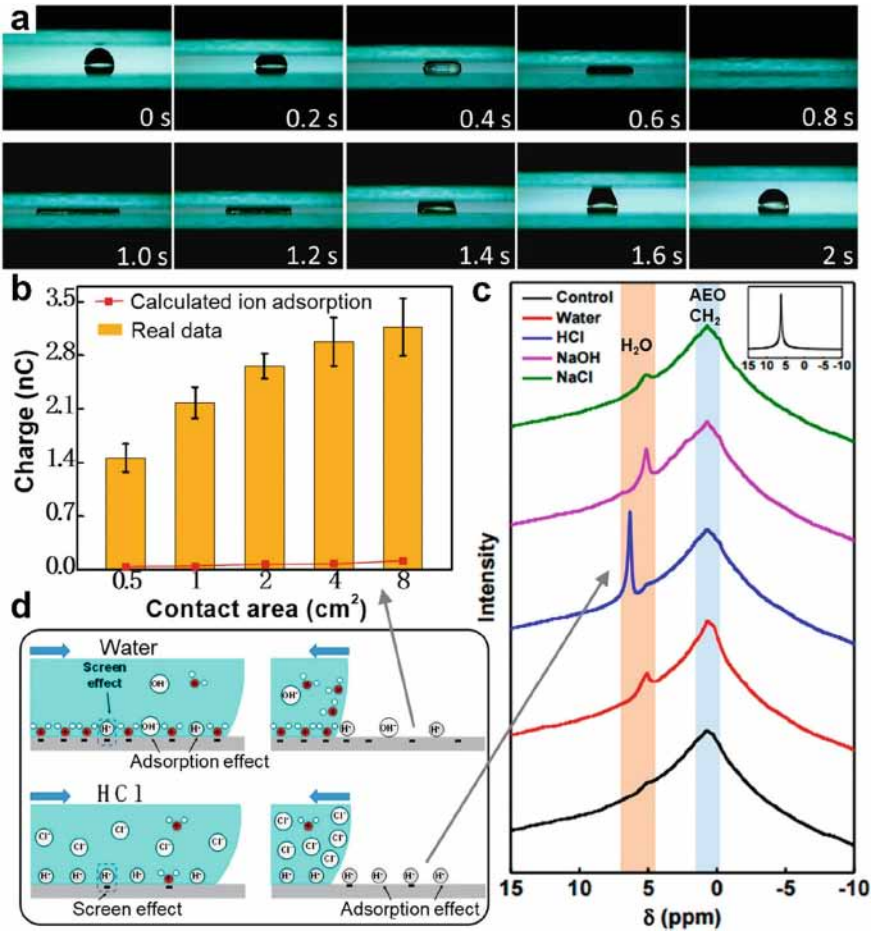

Fig. 7.12 The electrification behavior at the L-S contact interface was systematically investigated. **a** The water droplet spread uniformly during compression, forming a thin liquid film and significantly increasing the contact area between the liquid and PTFE. **b** Comparing the experimental results with the calculated values revealed that the calculated ion adsorption charge was over 10 times smaller than the experimental total triboelectric charge. **c** To further explore ion adsorption on the PTFE surface, solid-state ^{1}H NMR spectroscopy was used to analyze changes in hydrogen signals after CE. **d** These findings confirmed that both electron transfer and ion adsorption contribute to the L-S CE process. With permission from WILEY-VCH Verlag GmbH & Co. (2019) [46]

gradually adsorbed onto the solid surface, forming the IHP, a critical component of the EDL structure. In the second step (Fig. 7.13b), oppositely charged ions in the liquid are drawn to the charged solid surface through electrostatic interactions. This attraction drove the migration of these ions towards the surface, leading to the formation of the OHP. These two layers, IHP and OHP, together constituted the Stern layer, which was crucial for the overall structure of the EDL. In addition to

these structured layers, further oppositely charged free ions in the surrounding liquid contributed to the diffuse layer, completing the EDL. Overall, the two-step model is also referred to as Wang's model, which suggests that the formation of EDL is a result of liquid-solid interfacial CE. Secondly, both electron transfer and ion adsorption are possible in the process, but electron transfer is much faster than ion adsorption. The surface transferred charges (both electrons and ions) would attract the ions in the liquid and thus form an EDL. This type of EDL can be called the dynamic EDL, in which the compositions of ions and electrons could vary depending on the experimental conditions.

Wang's two-step model of the EDL offered significant insights into the charge transfer dynamics that occur at liquid-dielectric interfaces. It provided a nuanced understanding of how both electron transfer and ion adsorption contribute to the formation of the EDL, which was essential for the development of new materials and technologies for energy scavenging and information transmission. Specifically, the model enhanced the understanding by recognizing that ionization at L-S contact interfaces resulted in increased surface charge density, leading to charge dispersion in the diffuse layer. Furthermore, the electron transfer process could occur alongside ion adsorption, which was further divided into chemisorption (strong chemical bonding)

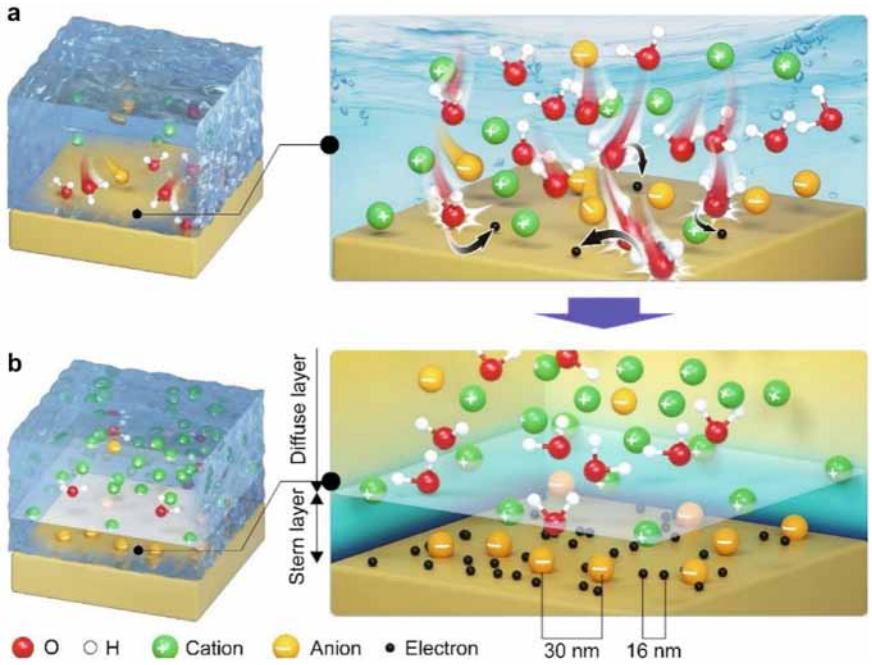

Fig. 7.13 The Wang's two-step EDL model and its formation processes. **a** In the first step, electron transfer occurs between the liquid and the solid, while ions might also adsorb onto the solid surface. **b** In the second step, free ions in the liquid are attracted to the charged solid surface due to electrostatic interactions. With permission from American Chemical Society (2022) [40]

and physisorption (weak physical bonding). For certain materials, such as SiO_2 and polytetrafluoroethylene (PTFE), electron transfer might dominate over ion transfer, leading to a more pronounced generation of surface charges. In these cases, the transferred electrons might become trapped in surface states, which were distinct from the atomic orbitals of the solid. The potential barrier for electrons in surface states was lower than that in atomic orbitals, making transferred electrons more mobile and less stable, a phenomenon that could be observed during heating experiments. In addition, the capacity of a material to either donate or accept electrons (electronegativity) could play a pivotal role in determining its behavior during charge exchange. Materials such as PTFE and fluorinated ethylene propylene (FEP), which were electron-withdrawing polymers (higher electronegative), exhibited stronger electron transfer during CE with water, further illustrating the importance of material properties in dictating charge transfer dynamics. It was also crucial to consider the spatial arrangement of charges in the EDL model. For example, in the case of CE between SiO_2 and DI water, calculations showed that the distance between neighboring electrons on the SiO_2 surface is approximately 16 nm, while the distance between adjacent ions is around 30 nm. These distances far exceed the thickness of the Stern layer, highlighting the necessity for any comprehensive EDL model to consider the spatial distribution of charges and their molecular-level interactions. This arrangement is crucial for accurately predicting EDL behavior and optimizing materials for diverse applications. In summary, the Wang's two-step EDL model offers a more comprehensive understanding of the complex interactions at the L-S interface. By incorporating both electron transfer and ion adsorption, while acknowledging the distinct roles of surface states and atomic orbitals, the model provides valuable insights into the charge transfer mechanisms fundamental to advancing energy-scavenging technologies and other applications.

7.4.3 Dynamic Regulation of the EDL at Liquid-Dielectric Interfaces

Wang's two-step model positioned the EDL as a pivotal interface for ionic-electronic coupling in the field of iontronics, enabling dynamic regulation of both ionic and electronic behaviors. Recent advancements underscore the potential of actively modulating the EDL to influence ionic migration, thereby enhancing the efficiency of electrical current generation. These developments lay the groundwork for innovations in energy scavenging and storage, particularly in effectively harnessing water-based energy. Emerging technologies that leverage the dynamic regulation of the EDL mainly include L-S TENGs and triboiontronic nanogenerators (TINGs). These systems offer promising solutions for capturing high-entropy energy from natural environments. L-S TENGs operate by modulating charge distribution within the EDL near dielectric materials through mechanical motion or electrostatic fields. They can be categorized into mechanically driven DC L-S TENGs [47, 48], mechanically

driven alternating current (AC) L-S TENGs [49, 50], and electrostatic-field-driven AC L-S TENGs [51, 52]. These devices exploit the high internal resistance of dielectric materials to produce high-voltage outputs. TINGs, by contrast, generate effective pulsed DC outputs via two primary mechanisms: creating asymmetric EDLs at ultra-thin conductor-liquid interfaces on dielectric substrates[8] or regulating charge density within the diffuse layer of the EDL adjacent to the dielectric surface [7]. Additionally, the inherent sensitivity of the EDL to external stimuli has enabled the development of self-powered information flow systems, unlocking applications in human-machine interaction and advanced interface probes [53]. The dynamic regulation of the EDL presents significant opportunities to enhance energy and information flow, with profound implications for intelligent, autonomous, and efficient systems in the Internet of Things (IoT) and artificial intelligence (AI). Innovative EDL modulation strategies show immense potential across diverse domains, from energy harvesting to the creation of self-powered devices, positioning these advancements to transform sustainable energy technologies and smart systems.

7.4.3.1 Various Types of L-S TENGs

L-S TENGs were operated by modulating charge distribution and migration within the EDL near dielectric material surfaces via mechanical motion or electrostatic fields. One of the first L-S TENGs were invented by Wang's group[49, 54, 55]. After over a decade of advancements, this technology has evolved into a well-established system. These devices can be classified into three main types: mechanically driven DC L-S TENGs, mechanically driven AC L-S TENGs, and electrostatic-field-driven AC L-S TENGs[56]. In mechanically driven DC L-S TENGs, where power generation was based on the movement of the EDL boundary along the dielectric material surface, the process was intricately linked to the coupling of the CE effect and the dynamic behavior of the EDL. When the liquid contacted the dielectric surface with the higher electronegativity, charge transfer occurred at the L-S contact interface, forming a negatively net-charged Stern layer tightly bound to the dielectric surface (Fig. 7.14a). Simultaneously, cations remained distributed within the diffuse layer in the liquid, consistent with Wang's two-step EDL model. The liquid slid across the dielectric surface driven by mechanical forces, causing the EDL boundary to move along the surface. It could generate continuous ion migration within the liquid. As the liquid moved away from the dielectric surface, cations within the diffuse layer interacted with the charge-collecting layer (Fig. 7.14b). This interaction redistributed charge carriers, inducing a unidirectional electron flow through an external circuit and sustaining a continuous current output. Power generation persisted as long as the liquid remained in motion, dynamically adjusting charge distribution within the EDL until a stable state was established near the dielectric material's surface. The reliability and efficiency of this process underscored its potential for effective energy scavenging and precise surface charge regulation. These attributes positioned mechanically driven DC L-S TENGs as highly promising technologies for practical applications in energy generation and advanced sensor systems.

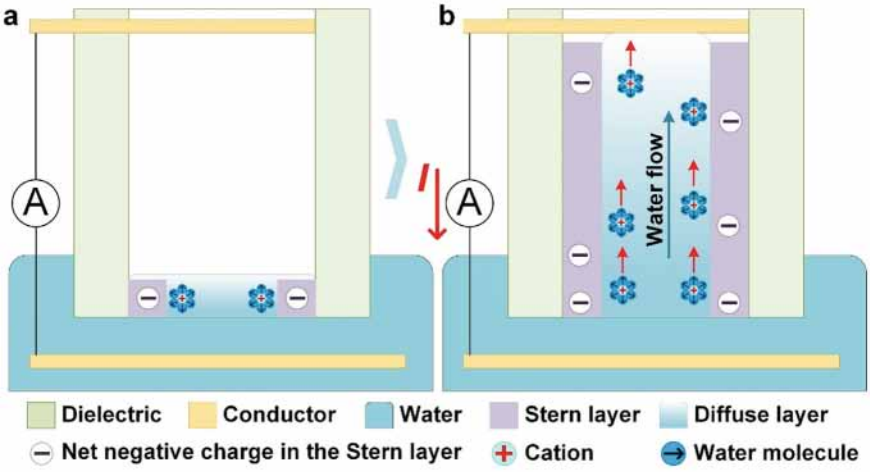

Fig. 7.14 The operating mechanism of mechanically driven DC L-S TENGs. **a** When the liquid contacted the dielectric surface with the higher electronegativity, charge transfer occurred at the L-S contact interface, forming a negatively net-charged Stern layer tightly bound to the dielectric surface. **b** As the liquid moved away from the dielectric surface, cations within the diffuse layer interacted with the charge-collecting layer, which redistributed charge carriers, driving a unidirectional flow of electrons through an external circuit and generating a continuous current output. With permission from the authors (2024) [56]

In 2015, Zhang et al. developed a microfluidic generator (MFG) as a representative mechanically driven DC L-S TENG[47] (Fig. 7.15a). This device was designed to achieve stable output performance by dynamically moving the EDL boundary at the contact interface between the KCl solution and the polydimethylsiloxane (PDMS) surface. The MFG was designed to produce a stable electrical current through L-S CE as the KCl solution flowed across the PDMS surface. Experimental results demonstrated that at a flow rate of 0.4 mL/min, the MFG produced a stable open-circuit voltage (V_{OC}) of approximately 0.16 V and a short-circuit current (I_{SC}) of around 1.75 nA (Fig. 7.15b and c). These outputs remained consistent across multiple on-off flow cycles, highlighting the device's operational stability. When the flow was stopped by turning off the syringe pump, the voltage output gradually decayed to zero, confirming the liquid-flow-dependent nature of the device. Further analysis demonstrated a nearly linear correlation between flow rate and current output, where an increase in flow rate proportionally enhanced the current, provided the flow direction and electrical connection were aligned in the forward configuration (Fig. 7.15d). Reversing the flow direction yielded a negative current output, demonstrating a predictable and reversible relationship between flow direction and electrical output (Fig. 7.15e). The effect of different ions, including Li^+, Na^+, and K^+, on current output was also evaluated (Fig. 7.15f). The MFG exhibited similar performance across these ions, indicating its compatibility with various ionic solutions. However, the KCl concentration significantly influenced the current output. At

lower concentrations (< 10 μM), the current increased with concentration, peaking at approximately 2.45 nA at 10 μM. This enhancement was attributed to reduced internal resistance and improved solution conductivity. At concentrations exceeding 10 μM, the current output declined sharply. This reduction was likely caused by the formation of a denser EDL via the ion adsorption on the PDMS surface at higher ion concentrations, which induced a screening effect that hindered charge transfer at the contact interface, thereby decreasing the generator's performance (Fig. 7.15g).

In addition to external mechanical forces, liquid evaporation offered an autonomous and effective mechanism for driving the motion of the EDL boundary at the liquid-dielectric interface. In 2022, Chi et al. developed a mechanically driven DC L-S TENG that utilized both liquid evaporation and capillary forces to guide water through Al_2O_3 ceramic sheets[48] (Fig. 7.16a). This process initiated L-S CE and generated a consistent electrical output. By regulating the environmental seal, the liquid evaporation rate, and consequently the continuous flow through nanochannels, could be precisely controlled, ensuring a stable electrical output (Fig. 7.16b). Environmental parameters such as temperature and airflow significantly influenced the evaporation rate, leading to higher current outputs (Fig. 7.16c). These findings underscored the critical role of environmental factors in optimizing the performance of energy-scavenging devices and provided strategies to enhance operational efficiency. The optimized DC L-S TENG demonstrated notable performance metrics, achieving a V_{OC} of 0.7 V and an I_{SC} of 0.3 μA, highlighting its potential for diverse self-powered systems and energy-scavenging applications. In mechanically driven DC L-S TENGs, prolonged liquid flow over solid surfaces could lead to the formation of a dense EDL, which might impede subsequent charge transfer and reduce output stability. To address this limitation, Dong et al. in 2022 introduced a gas-liquid two-phase flow-based triboelectric nanogenerator (GL-TENG) [57] (Fig. 7.16d). This design leveraged dielectric breakdown to dissipate accumulated charges in the dense EDL, maintaining the solid surface's initial charge density and enabling efficient subsequent charge transfer at the L-S contact interface. The GL-TENG utilized gas-liquid flow dynamics to optimize the contact area and relative velocity between the water and the PTFE tube, enhancing both ion mobility and charge density within the diffuse layer. This configuration ensured a stable current output by dynamically facilitating charge exchange across the interface. During continuous operation, accumulated charges induced dielectric breakdown (Fig. 7.16e), producing high pulse voltages and effectively resetting the tube's surface charge state to sustain subsequent charging cycles. By incorporating dielectric breakdown, the GL-TENG achieved significantly enhanced operational stability and energy-scavenging performance. The device exhibited exceptional pulse output values, with a V_{OC} of 3789 V, an I_{SC} of 867 μA (Fig. 7.16f), and a volumetric peak power (P_R) density of 143.6 mW/cm^3. These metrics underscored the GL-TENG's potential for high-voltage output and reliable energy scavenging across diverse applications.

In addition to addressing the dense EDL's screening effect on charge transfer at L-S contact interfaces through the introduction of the dielectric breakdown effect in mechanically driven DC L-S TENGs, mechanically driven AC L-S TENGs offered a complementary approach by enabling effective control over ion migration within the

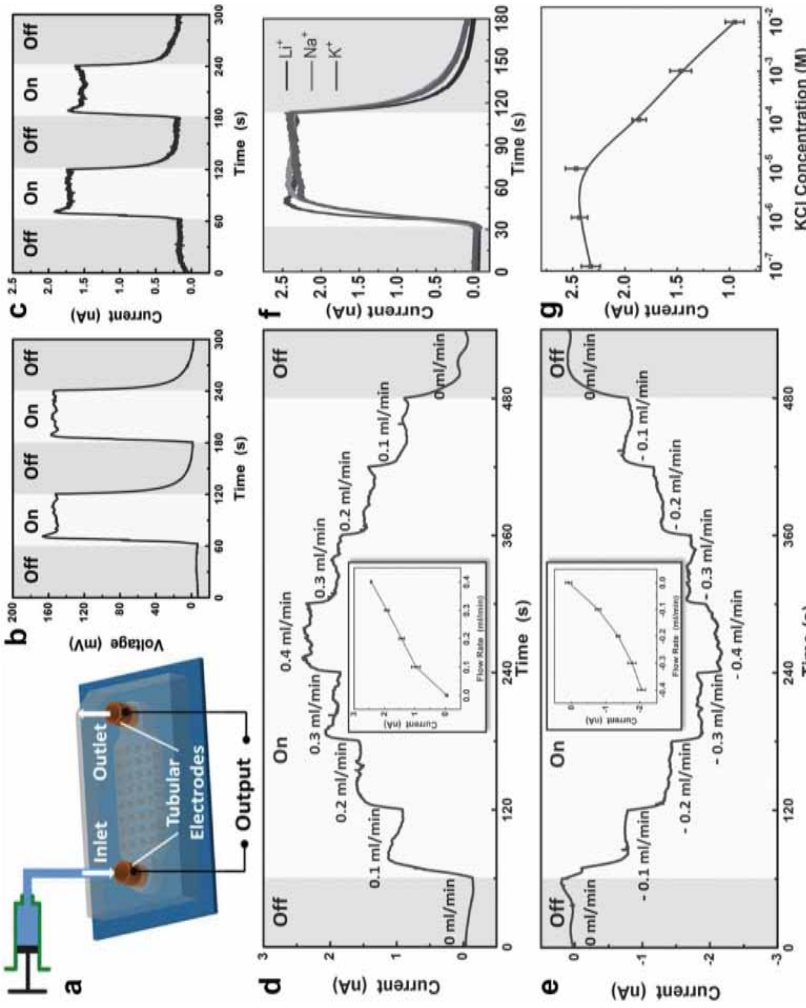

Fig. 7.15 An MFG as a typical mechanically driven DC L-S TENG and its output performance. **a** Schematic diagram of the MFG. **b**, **c** At a flow rate of 0.4 mL/min, the MFG generated a stable V_{OC} of approximately 0.16 V and an I_{SC} of around 1.75 nA. **d**, **e** The output performance of MFG was related to the direction and flow rate of the liquid. **f** The MFG exhibited similar performance across Li^+, Na^+, and K^+, indicating its compatibility with various ionic solutions. **g** Effect of ion concentration in solution on the output performance of the MFG. With permission from WILEY-VCH Verlag GmbH & Co. (2015) [47]

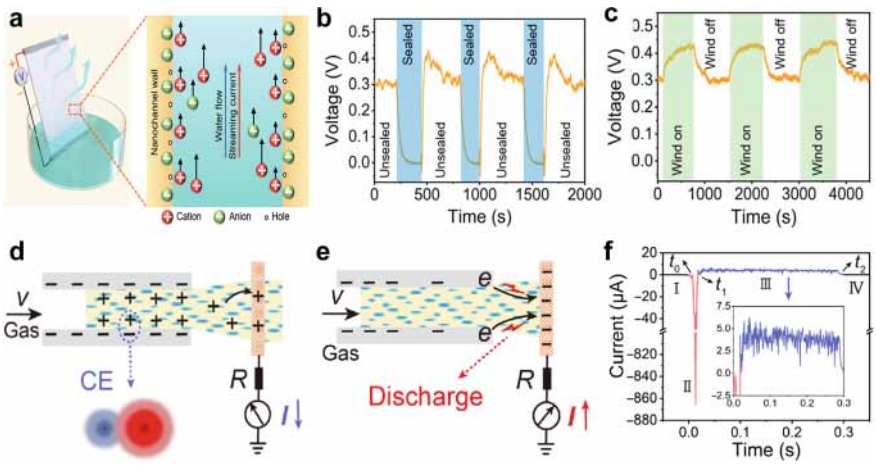

Fig. 7.16 A series of mechanically driven DC L-S TENG and their output characteristics. **a** A mechanically driven DC L-S TENG was introduced in 2022, which harnesses both liquid evaporation and capillary forces to guide the water through Al_2O_3 ceramic sheets. **b** By adjusting the environmental seal, the rate of liquid evaporation could be precisely controlled, resulting in a stable electrical output. **c** Environmental parameters such as temperature and airflow significantly amplified the evaporation rate, leading to increased current output. With permission from the authors (2022) [48]. **d** The GL-TENG was developed in 2022. **e** During continuous operation, the accumulated charges initiate dielectric breakdown, generating higher pulse voltages and effectively resetting the tube's surface charge state to support subsequent charging cycles. **f** The GL-TENG could generate a higher I_{SC} of 867 μA. With permission from the authors (2022) [57]

diffuse layer. This was achieved by manipulating the mechanical motion of the Stern layer adjacent to the dielectric surface by external mechanical forces. This strategy facilitated the flexible and consistent generation of stable AC outputs by dynamically harnessing the processes of charge accumulation and release at the dielectric-liquid interface. During the operation of mechanically driven AC L-S TENGs, when the liquid came into contact with a dielectric surface possessing higher electronegativity, an EDL formed stably at the contact interface (Fig. 7.17a). The Stern layer, characterized by a net negative charge, adhered closely to the dielectric, while cations from the liquid accumulated in the adjacent diffuse layer, forming a distributed charge region. At this stage, charge equilibrium was established between the dielectric and liquid. As mechanical motion separates the dielectric from the liquid, the interaction between the Stern and diffuse layers diminishes, weakening the electrostatic binding of cations to the charged dielectric surface. This reduction triggered electron transfer between the two metal charge-collecting layers via electrostatic induction, generating a forward I_{SC} in the external circuit (Fig. 7.17b). Once the dielectric and liquid were fully separated, electron transfer concluded, and a new equilibrium state was reached (Fig. 7.17c). When the dielectric re-approached the liquid, cations migrated back toward the Stern layer, re-establishing the diffuse layer within the EDL (Fig. 7.17d). This process induced a reverse electron flow in the external circuit, generating a

reverse I_{SC}. Through this continuous cycle of contact and separation, mechanically driven AC L-S TENGs efficiently leveraged the dynamic interactions between the Stern and diffuse layers to produce stable AC outputs.

The mechanically driven AC L-S TENG could be realized using PDMS as the dielectric material (Fig. 7.18a) [49]. When water fully contacted the PDMS surface, a stable EDL was established at the interface. During cyclic separation and re-contact between the PDMS and water, cations in the diffuse layer synchronized with the Stern layer on the PDMS surface. This coordinated movement induced electron transfer back and forth in the external circuit through electrostatic induction, resulting in an AC output. Initial experiments explored the impact of varying ion concentrations on the performance of L-S TENGs (Fig. 7.18b). Adding ethanol to water reduced the overall ionic concentration, decreasing both the net charge density in the Stern

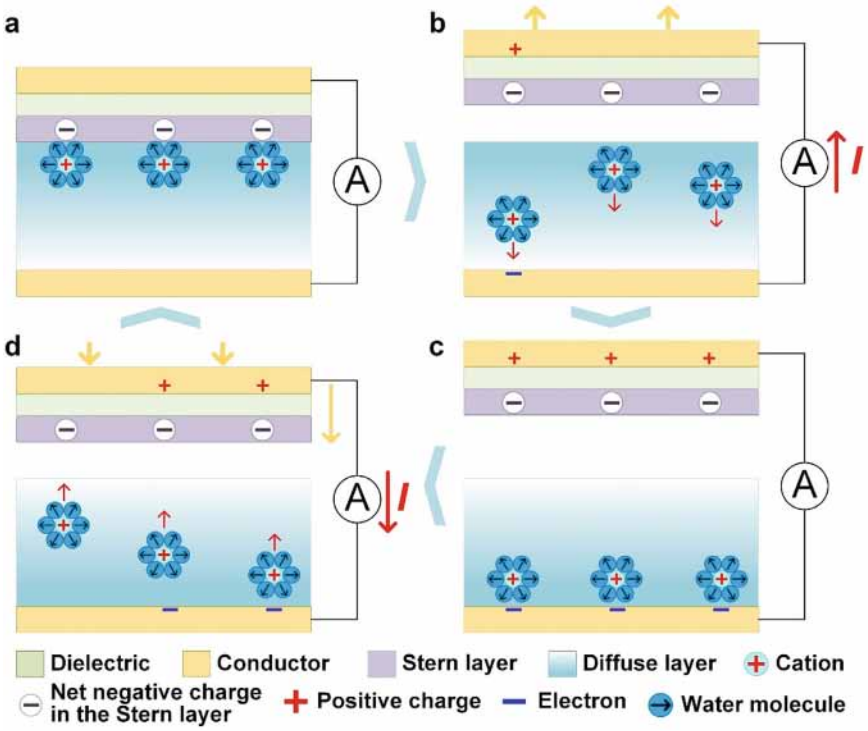

Fig. 7.17 The operating mechanism of mechanically driven AC L-S TENGs. **a** As the liquid came into contact with a dielectric surface with higher electronegativity, a stable EDL formed. **b** The net negative charge in the Stern layer induced electron transfer in the external circuit via electrostatic induction, generating a forward I_{SC}. **c** Upon full separation of the dielectric from the liquid, electron transfer was completed, and the system attained a new equilibrium. **d** When the dielectric re-approached the liquid, cations migrated back toward the Stern layer, re-forming the diffuse layer in the EDL. This process induced a reverse electron flow in the external circuit, generating a reverse I_{SC}. With permission from the authors (2024) [56]

layer and the cation density in the diffuse layer. This reduction impaired electron transfer efficiency, lowering the overall output. Modifications to the PDMS surface microstructure were also explored, increasing the L-S contact area and enhancing ion migration in the diffuse layer. These structural optimizations significantly improved output performance. Under optimal conditions, the L-S TENG achieved a V_{OC} of approximately 80 V and an I_{SC} density of 0.25 μA/cm^2 at an operating frequency of 5 Hz. With an 88 MΩ load resistance, the P_R density reached 5 μW/cm^2 (Fig. 7.18c), demonstrating its potential for efficient energy scavenging in self-powered applications. Building on the practical potential of mechanically driven AC L-S TENGs for ocean and wave energy scavenging, You et al. developed an advanced single-electrode AC L-S TENG in 2021 [50] (Fig. 7.18d). They systematically analyzed the effects of L-S contact area and relative sliding velocity on output performance. Experimental results showed that expanding the PTFE-water contact area increased ion density in both the Stern and diffuse layers, significantly enhancing electron transfer efficiency (Fig. 7.18e). Additionally, higher relative sliding velocities between the PTFE membrane and water improved output performance (Fig. 7.18f). This improvement was attributed to intensified interfacial collisions, which expanded the microscopic contact area and promoted controlled, directional ion migration. By optimizing contact area and sliding speed, the single-electrode L-S TENG achieved a remarkable V_{OC} of approximately 400 V, underscoring its promise for scavenging energy from ocean and wave environments. This innovation highlighted the potential of mechanically driven AC L-S TENGs for sustainable energy solutions in marine applications and offers a roadmap for further advancements in L-S energy scavenging technologies.

While ocean wave energy has garnered substantial attention for mechanically driven AC L-S TENG applications, the untapped potential of raindrop kinetic energy presents a promising alternative for sustainable power generation. In 2014, Lin et al. first introduced a mechanically droplet-driven AC L-S TENG specifically designed to harvest raindrop energy[54] (Fig. 7.19a). This device utilized the negatively charged Stern layer on the PTFE surface to drive ion migration within the diffuse layer of droplets, producing efficient AC output. By optimizing the droplet impact height, the contact area between droplets and the PTFE film was maximized, increasing the charge transfer per droplet and improving overall performance (Fig. 7.19b). At an optimized impact height of 90 cm, a single 30-μL droplet sliding across the PTFE surface generated a V_{OC} of 9.3 V and an I_{SC} of 17 μA (Fig. 7.19c), corresponding to a P_R density of 9.1 μW/cm^2. This work demonstrated the feasibility of utilizing raindrops as a renewable energy source, marking a significant breakthrough in sustainable energy scavenging. To further enhance energy-scavenging efficiency, Xu et al. developed an advanced droplet-driven AC L-S TENG in 2020 [58] (Fig. 7.19d). In this design, droplets striking the negatively charged PTFE surface spread across it while simultaneously contacting a top aluminum (Al) charge-collecting layer. This configuration exploited a "bulk effect", wherein rapid electron transfer occurred between the Al layer and the bottom indium tin oxide (ITO) via an external circuit, generating a robust positive current. As droplets moved across the Al layer, reverse electron flow produced a low-amplitude current. This bulk effect significantly improved

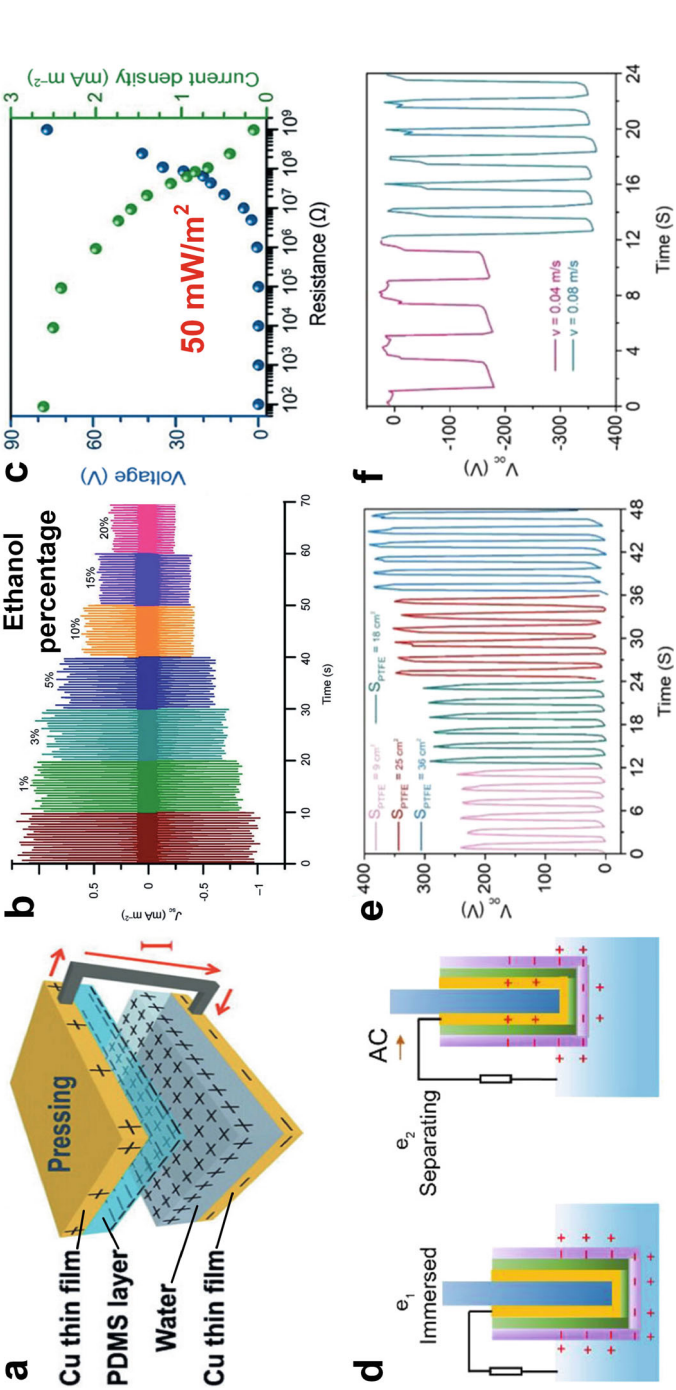

Fig. 7.18 A series of mechanically driven AC L-S TENG and their output characteristics. **a** The first mechanically driven AC L-S TENG was developed in 2013. **b** Increasing ethanol concentration in the water led to a reduction in electron transfer efficiency and the overall output. **c** With an 88 MΩ load resistance, this L-S TENG achieved a P_R density of 5 μW/cm^2. With permission from WILEY-VCH Verlag GmbH & Co (2013) [49]. **d** To harvest ocean and wave energy, a single-electrode AC L-S TENG was developed in 2021. **e** Expanding the PTFE-water contact area directly increased the ion density in both the Stern and diffuse layers, significantly increasing the output performance of the L-S TENG. **f** The higher relative sliding velocity between the PTFE membrane and water further improved the output performance. With permission from American Chemical Society (2021) [50]

performance, yielding a V_{OC} of 143.5 V and an I_{SC} of 270 μA (Fig. 7.19e). These results far exceeded those of single-electrode configurations without the Al layer. Under an optimal load resistance of 332 kΩ, the P_R density reached 5.01 mW/cm^2, representing a three-order-of-magnitude increase compared to conventional designs. Building on the bulk effect, Li et al. developed a high-voltage droplet-driven AC L-S TENG in 2023 [59] (Fig. 7.19f). Their work identified directional ion migration within the droplet's diffuse layer, guided by the electrostatic field of the Stern layer on the PTFE surface, as a key factor for power enhancement. When droplets struck the negatively charged PTFE and contacted the top charge-collecting layer, rapid anion migration caused the electron transfer to generate a high-magnitude positive current. As droplets moved away, cations migrated back more slowly, resulting in a low-magnitude reverse current. By optimizing droplet dynamics and refining circuit designs, this generator achieved an exceptional V_{OC} of 1200 V. These innovations highlight the transformative potential of droplet-driven AC L-S TENGs for renewable energy applications. By precisely controlling ion migration and L-S interactions, these devices offer novel strategies to maximize energy output and represent a promising pathway for sustainable energy solutions.

The various contact states between the droplet and the dielectric material significantly impact the output performance of mechanically droplet-driven AC L-S TENGs while also influencing the wettability characteristics of the dielectric surface. Wettability, a fundamental property dictating L-S interface interactions, is critical for numerous industrial and scientific applications. However, the dynamic interplay between surface charge and wettability, especially in the context of CE, remains intricate and incompletely understood. To address it, Tang et al., systematically investigated the relationship between triboelectric charge generation and the subsequent alteration in the wettability of dielectric surfaces, elucidating the CE induced wetting (CEW) phenomenon [60] (Fig. 7.20a). A custom-designed droplet generator was developed to simulate and monitor the behavior of water droplets sliding across an inclined dielectric surface, emphasizing the influence of triboelectric charge accumulation on the dynamic wettability of these materials. The apparatus facilitated precise, real-time measurements of CA variations and surface potential changes during droplet interaction. The spreading behavior of the droplets, driven by surface tension, governed the CA at the L-S contact interface (Fig. 7.20b). A smaller CA corresponds to enhanced wettability, while a larger CA indicates reduced wettability. When a water droplet is deposited, dielectric surfaces, especially those with strong electronegativity like PTFE, acquire residual surface charges via CE. The polarity of the charges generated adheres to the principle of charge opposition: the dielectric surface typically accumulates negative charges, while the water droplet carries positive charges. This triboelectric charge induces an electric field gradient at the interface, electrostatically attracting polar water molecules and ions, thereby modulating the surface's wetting behavior (Fig. 7.20c). In this study, the PTFE surface potential and CA of PTFE films were monitored as they interacted with water droplets. The results revealed a marked reduction in hydrophobicity, with the CA decreasing from 114° to 99° as the number of water droplets sliding across the surface increased from 0 to 1000 (Fig. 7.20d). Concurrently, as measured by KPFM, the PTFE surface

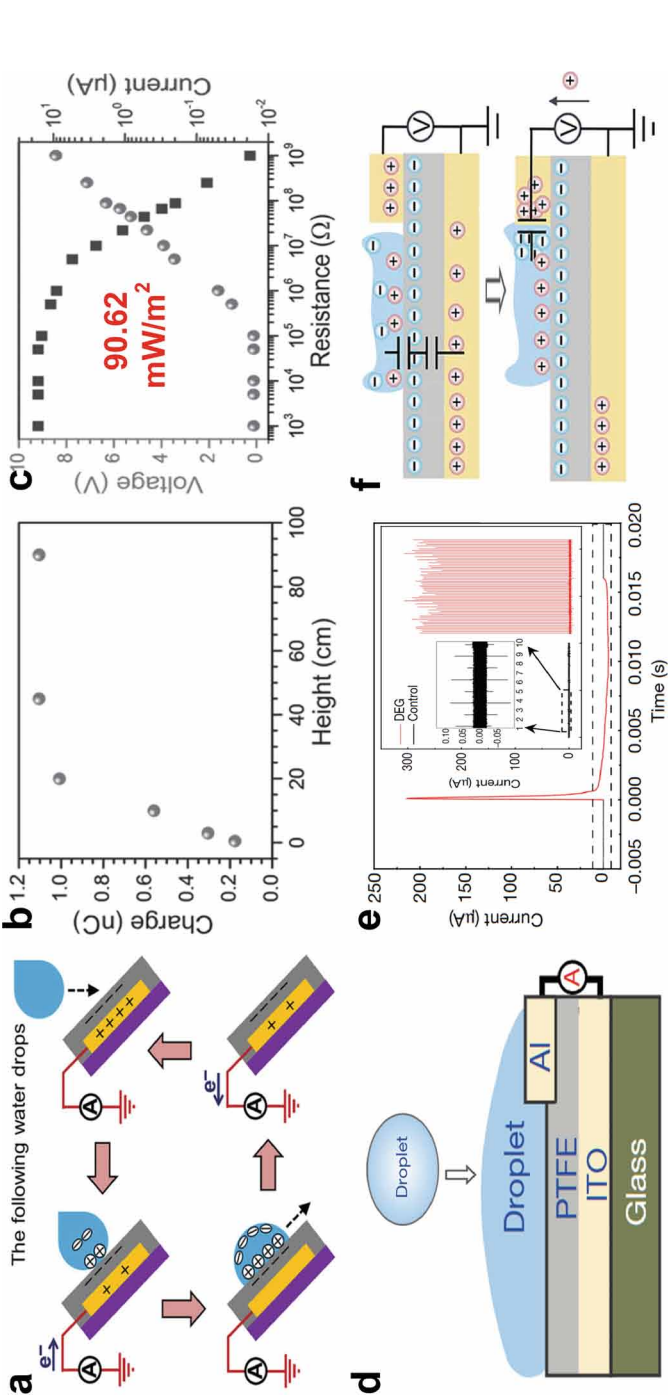

Fig. 7.19 A series of mechanically droplet-driven AC L-S TENG and their output characteristics. **a** A mechanically droplet-driven AC L-S TENG specifically designed to harness raindrop energy was pioneered in 2014. **b** By optimizing the droplet impact height, the contact area between droplets and the PTFE film was enhanced, thereby improving output performance. **c** After height optimization to 90 cm, this droplet-driven AC L-S TENG could achieve a P_R density of 9.1 μW/cm^2. With permission from WILEY-VCH Verlag GmbH & Co (2014) [54]. **d** An advanced droplet-driven AC L-S TENG was developed in 2020. **e** Its V_{OC} and I_{SC} could reach approximately 143.5 V and 270 μA, respectively. With permission from the Authors (2020) [58]. **f** A high-voltage droplet-driven AC L-S TENG was developed by Li et al. in 2023. With permission from the Authors (2023) [59]

potential shifted from a positive value of 11 mV to a negative potential of 663 mV, indicating the accumulation of negative charges on the surface (Fig. 7.20e). This shift in surface potential is indicative of the triboelectric charge transfer that occurred during the CE process.

The CEW phenomenon can be described as a two-step process: firstly, the generation of triboelectric charges at the contact interface, followed by the alteration in wettability due to the accumulation of these charges (Fig. 7.21a). The charge storage capacity of dielectric films enables sustained retention of surface charges, leading to prolonged modifications in wettability. To gain a deeper understanding of the mechanism, molecular dynamics (MD) simulations were employed to model the behavior of

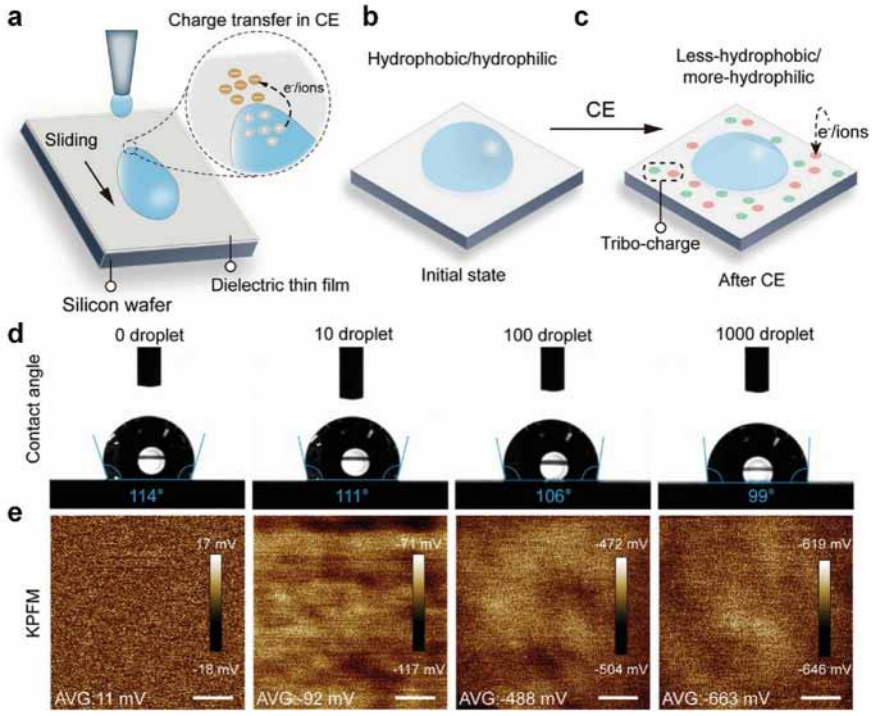

Fig. 7.20 The relationship between triboelectric charge generation and the subsequent alteration in the wettability of dielectric surfaces was systematically investigated in 2024, elucidating the CEW phenomenon. **a** A custom-made droplet generator was developed, which allowed for the simulation and monitoring of the behavior of water droplets sliding across an inclined dielectric surface. **b** The spreading behavior of the droplets, governed by surface tension, dictates the CA formed at the L-S contact interface. **c** Triboelectric charge creates an electric field gradient at the interface, which electrostatically attracts both polar water molecules and ions, thereby influencing the wetting behavior of the surface. **d** The results revealed a marked reduction in hydrophobicity, with the CA decreasing from 114° to 99° as the number of water droplets sliding across the surface increased from 0 to 1000. **e** The surface potential, as measured by KPFM, shifted from a positive value of 11 mV to a negative potential of 663 mV, indicating the accumulation of negative charges on the surface. With permission from Wiley-VCH GmbH (2024) [60]

water droplets on PTFE surfaces under different charge states (Fig. 7.21b). The simulations indicated a significant reduction in the CA, from 118° to 96°, as a result of the induced negative charges on the surface. Furthermore, ab initio calculations were used to examine the intermolecular interactions between water molecules and charged PTFE surfaces (Fig. 7.21c). These calculations revealed that the presence of triboelectric charges leads to stronger hydrogen bonding, particularly through O–H···F interactions, between water molecules and the fluorine atoms on the PTFE surface (Fig. 7.21d). The enhanced hydrogen bonding was observed to decrease the distance between the oxygen and hydrogen atoms in the O–H···F bond, thereby reducing the interfacial tension and promoting a more hydrophilic surface (Fig. 7.21e). These findings were supported by experimental data, which demonstrated that the presence of surface charges significantly alters the interfacial properties, resulting in enhanced wettability. In addition to PTFE, the study extended to other materials such as polymethyl methacrylate (PMMA) and PDMS, which exhibit distinct charge behaviors upon contact with water (Fig. 7.21f). PMMA, which acquires a negative charge, showed similar behavior to PTFE, with a reduction in hydrogen bond length, thereby enhancing wettability. Conversely, PDMS, which acquires a positive charge, displayed an unexpected trend: the hydrogen bond length increased, suggesting a unique proton-driven hydrogen bonding mechanism. This difference in behavior highlights the complexity of charge-induced wetting phenomena across different materials. Specifically, the number of hydrogen bonds increased in PDMS from two to three, indicating a more pronounced interaction between water molecules and the substrate, which further promoted wettability. These observations underscore the intricate relationship between surface charge and wettability. Triboelectric charge accumulation at the L-S interface significantly influences droplet dynamics, affecting both advancing and receding CAs. The advancing CA, linked to droplet spreading, is highly sensitive to electrostatic forces, while the receding CA, reflecting retraction, is less impacted due to the stabilized electrostatic environment after initial contact. This study highlights the role of triboelectric charge in modulating wettability and interface interactions. By leveraging the CEW effect, droplet movement on solid surfaces can be controlled for applications ranging from TENG-based energy harvesting to surface engineering for improved liquid management. Additionally, these findings enable the design of advanced materials with tailored wettability for applications in self-cleaning, droplet manipulation, and microfluidics.

Advances in mechanically driven AC L-S TENGs have been propelled by a deeper understanding of the dynamic modulation of diffuse layers at dielectric-liquid interfaces, with a focus on stabilizing the EDL. However, visualizing the complexities of EDL formation has remained challenging. The influence of the EDL during phase transitions is an intriguing area of study. A recent investigation explored how the phase transition from ice to water affects charge transfer dynamics with dielectric materials [53] (Fig. 7.22a). The stages of charge transfer and EDL formation during ice melting in contact with PTFE were systematically elucidated (Fig. 7.22b and c). Initially, during the S-S contact stage, electron transfer dominated. The limited contact area resulted in relatively weak charge transfer. As melting began, microdroplets formed on the ice surface, substantially increasing the contact area with

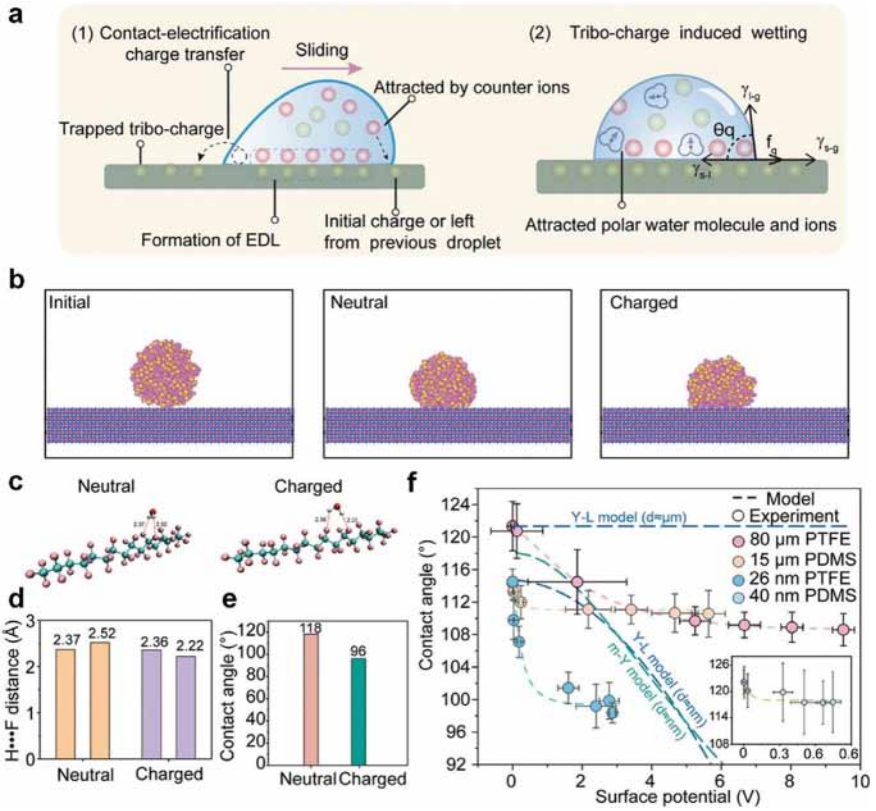

Fig. 7.21 The theoretical model and influencing factors of CEW were systematically investigated. **a** The CEW phenomenon can be described as a two-step process. **b** MD simulations were employed to model the behavior of water droplets on PTFE surfaces under different charge states. **c** Ab initio calculations were used to examine the intermolecular interactions between water molecules and charged PTFE surfaces. **d** The presence of triboelectric charges leads to stronger hydrogen bonding between water molecules and the fluorine atoms on the PTFE surface. **e** The enhanced hydrogen bonding was observed to decrease the distance between the oxygen and hydrogen atoms in the O–H···F bond, thereby reducing the interfacial tension and promoting a more hydrophilic surface. **f** In addition to PTFE, the study extended to other materials such as PMMA and PDMS, which exhibit distinct charge behaviors upon contact with water. With permission from Wiley-VCH GmbH (2024) [60]

PTFE and enhancing electron transfer, leading to a sixfold increase in transferred charge. With continued melting, larger droplets condensed, transitioning the S-S contact stage toward the L-S contact stage. At this stage, EDL formation began, progressively screening the dielectric surface charge. This shifted the primary mechanism from electron transfer to charge migration in the diffuse layer, reducing the total transferred charge. Upon full melting, a stable EDL formed at the contact interface, generating strong electrostatic shielding that minimizes further charge transfer. To further investigate these phenomena, Wei et al. [53] studied the influence of

temperature on charge transfer during ice melting. By raising ambient temperatures to accelerate the melting process, they observed distinct trends in transferred charge. At 20°C, the peak transferred charge reached 1.75 nC over 214 s (Fig. 7.22d). At 40°C, faster melting resulted in a peak charge of 1.21 nC within 105 s (Fig. 7.22e). At 60°C, the peak charge was reduced to 0.58 nC, achieved in just 98 s (Fig. 7.22f). These results indicated that while higher temperatures accelerate melting and increase the contact area, they also expedited the EDL formation, enhancing the electrostatic shielding effect and thereby reducing the total transferred charge. The critical role of phase transitions and temperature in triboelectric charge exchange at L-S contact interfaces was highlighted, affecting both electron transfer rates and charge dissipation dynamics. The study provided valuable insights into the interplay between thermal conditions, phase changes, and charge transfer mechanisms, laying a foundation for advanced energy-scavenging strategies in S-S and L-S TENG systems. These insights opened avenues for designing devices that optimize charge interactions, enhance energy conversion efficiency, and improve performance under dynamic environmental conditions.

Mechanically driven AC L-S TENGs often faced performance instability due to liquid evaporation, which altered interfacial properties, and diminished both charge transfer efficiency and output. To address this challenge, employing a sealed design could effectively limit evaporation while encapsulating the liquid with highly electronegative dielectric materials enhances EDL stability by promoting a dense and uniform EDL formation. Furthermore, the dynamic regulation of charge distribution in the EDL using a unidirectional electrostatic field enabled the development of electrostatic-field-driven AC L-S TENGs, significantly enhancing output performance and operational stability. The working principle of an electrostatic-field-driven AC L-S TENG could be delineated into four distinct stages. In the initial stage, the liquid established contact with dielectric material I, triggering the formation of an EDL at the contact interface (Fig. 7.23a). Concurrently, dielectric I interacted with a more electronegative dielectric II on its opposite side, facilitating electron transfer from dielectric I to dielectric II and imparting a net positive charge to the surface of dielectric I. During the second stage, as dielectric I and dielectric II began to separate (Fig. 7.23b), the positive charge on dielectric I generated an electric field that drove cations in the EDL's diffuse layer away from the liquid-dielectric I interface, pushing them toward the charge-collecting layer. This movement induced electron flow from the ground to the charge-collecting layer, generating a positive current. In the third stage, as dielectric I and dielectric II reached full separation (Fig. 7.23c), the migration of ions ceased, halting electron transfer and stabilizing the system momentarily. Finally, during the fourth stage, as dielectric II returned toward dielectric I (Fig. 7.23d), the electric field associated with the positive charge on dielectric I was rebalanced through electrons distributed onto dielectric II. Simultaneously, cations migrated back to the liquid-dielectric I interface, re-establishing the diffuse layer and generating a reverse current. This cyclic process, driven by continuous mechanical stimulation, ensured stable AC output. The sealed design not only mitigated evaporation-induced disruptions but also strengthened the structural integrity of the dielectric-liquid interface, enhancing charge transfer efficiency and

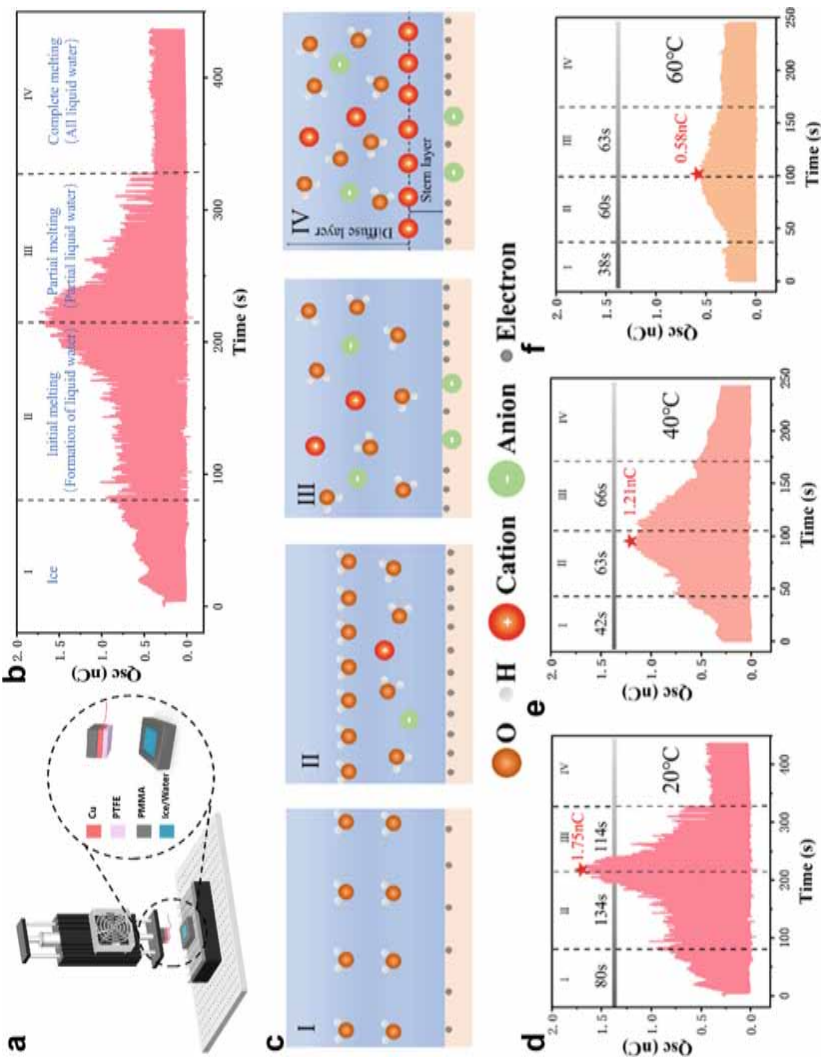

Fig. 7.22 A study examining how the phase transition from ice to water influences charge transfer dynamics with dielectric materials was conducted in 2024. **a** The experimental system. **b** The charge transfer stages between ice and PTFE at different melting stages. **c** The EDL formation stages between ice and PTFE at different melting stages. **d–f** The influence of temperature on charge transfer and EDL formation during ice melting was studied. With permission from Elsevier Ltd. (2024) [53]

energy conversion reliability. These innovations significantly expanded the adaptability of L-S TENGs to diverse environmental conditions, paving the way for efficient, stable energy-scavenging solutions in real-world applications. By combining structural enhancements with advanced charge modulation strategies, these devices held great promise for powering next-generation sustainable technologies.

In 2016, Yi et al. introduced an innovative shape-adaptive triboelectric nanogenerator (SA-TENG) [51] (Fig. 7.24a), a notable example of an electrostatic-field-driven AC L-S TENG that leveraged a unidirectional electrostatic field to regulate charge distribution within the EDL. This design uniquely utilized deformation to enhance energy output. Operating in single-electrode mode, the SA-TENG employed a 20 wt% NaCl solution as a conductive liquid electrode. When the conductive liquid was

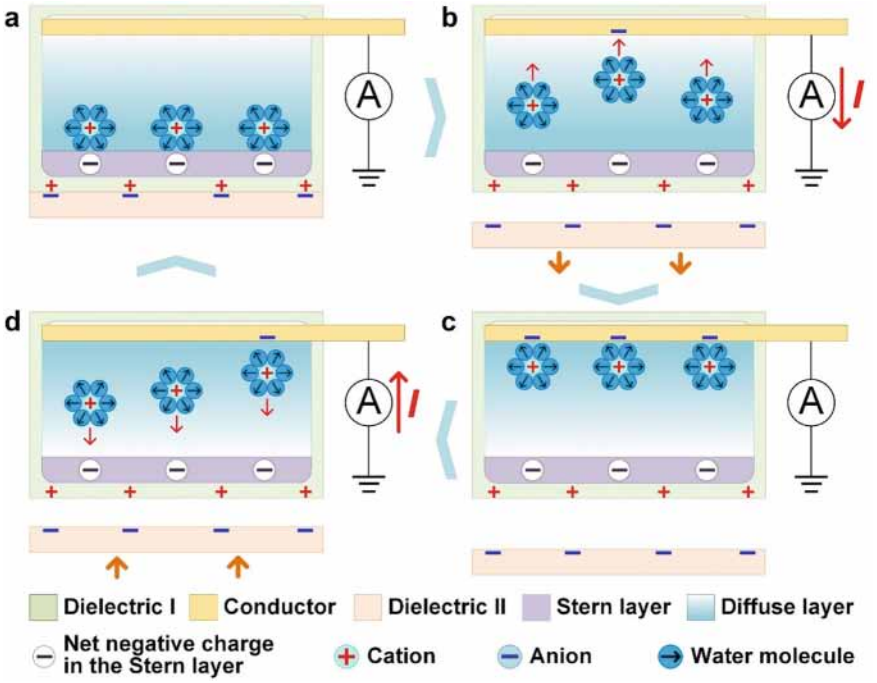

Fig. 7.23 The operating mechanism of electrostatic-field-driven AC L-S TENGs. **a** In the initial stage, the liquid established contact with dielectric material I, triggering the formation of an EDL at the contact interface. **b** During the second stage, as dielectric I and dielectric II began to separate, the positive charge on dielectric I generated an electric field that drove cations in the EDL's diffuse layer away from the liquid-dielectric I interface, pushing them toward the charge-collecting layer. **c** In the third stage, as dielectric I and dielectric II reached full separation, the migration of ions ceased, halting electron transfer and stabilizing the system momentarily. **d** During the fourth stage, as dielectric II returned toward dielectric I, the electric field associated with the positive charge on dielectric I was rebalanced through electrons distributed onto dielectric II. With permission from the authors (2024) [56]

grounded through an external load, the flexible rubber shell of the SA-TENG interacted with an external dielectric material, such as nylon (PA), to efficiently harvest mechanical energy. The performance of the SA-TENG was governed by two critical parameters: the deformation of the SA-TENG (denoted as d_0) and the distance (d_1) between the external PA film and the rubber shell. Both factors significantly influenced the transferred charge (Q_{SC}) and V_{OC} (Fig. 7.24b and c). Increased deformation d_0 enlarged the contact area between the PA film and the SA-TENG surface, thereby enhancing Q_{SC} and V_{OC}. Similarly, increasing d_1 while maintaining constant deformation strengthened electric field interactions, further boosting Q_{SC} and V_{OC}. Under fixed d_0 and d_1, Q_{SC} and V_{OC} stabilized, however, the I_{SC} increased with the frequency of contact between the rubber shell and the PA film, underscoring the role of contact rate in optimizing power output. Adjusting the dimensions of the SA-TENG also impacted performance. Lengthening or widening the device enhanced Q_{SC} and V_{OC} by increasing the contact area between the triboelectric surfaces. Conversely, a thicker rubber shell reduced Q_{SC} and V_{OC} under fixed d_0 and d_1 conditions due to the increased distance between the liquid electrode and the dielectric surface, which lowered capacitance and diminished electrical output. Experimental testing under periodic contact at ~ 0.45 Hz revealed that the SA-TENG achieved a V_{OC} of approximately 67.71 V (Fig. 7.24d), a Q_{SC} density of ~ 35.35 μC/m^2 (Fig. 7.24e), and an I_{SC} density of ~ 0.83 mA/m^2 (Fig. 7.24f). Encased in a flexible polymer, the SA-TENG was highly adaptable and capable of scavenging energy through various operational modes while enduring strains of up to 300%. Its seamless adaptability to complex three-dimensional and curved surfaces establishes it as an optimal candidate for wearable power sources and self-powered sensors in biomechanical motion monitoring. The scalable, flexible design of the SA-TENG marks a notable breakthrough in stretchable electronics, delivering a robust, adaptable energy solution and multifunctional sensing capabilities across diverse applications.

To further enhance the output performance of electrostatic-field-driven AC L-S TENGs, expanding the effective microscopic contact area of the electrostatic field has been demonstrated as a promising approach. Building on this principle, Chen et al. developed a hierarchical micro-nanostructured triboelectric nanogenerator (HM-TENG) in 2019 [52], designed to efficiently harvest both mechanical energy and raindrop energy (Fig. 7.24g). The elastomer surface of this device was engineered with a hierarchical micro-nanostructure fabricated through electrospinning, significantly increasing its surface roughness. This enhancement amplified the microscopic contact area between the elastomer and the dielectric film, thereby strengthening the electrostatic field. As a result, a greater number of free ions were driven to migrate directionally across the elastomer-ion conductor interface, increasing the current output. Moreover, applying pressure on the dielectric film further deformed the elastomer, enhancing its contact with the dielectric film (Fig. 7.24h). This enhancement amplified electrostatic interactions, significantly improving the device's output performance. The optimized HM-TENG achieved remarkable results, including a V_{OC} of approximately 170 V, an I_{SC} of 12.5 μA/cm^2, and a Q_{SC} density of 24 nC/cm^2. When paired with an external load resistance of 13 MΩ, the HM-TENG produced a power density of 0.72 mW/cm^2 (Fig. 7.24i). This study highlighted the crucial role of

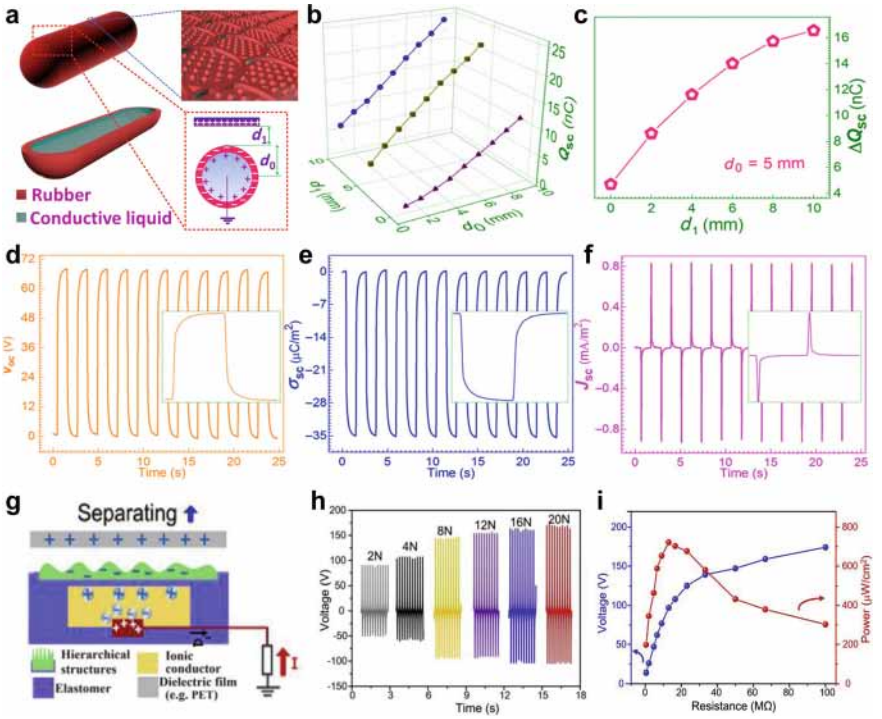

Fig. 7.24 A series of electrostatic-field-driven AC L-S TENGs and their output characteristics. **a** The SA-TENG as an exemplary electrostatic-field-driven AC L-S TENG was developed in 2016. **b**, **c** The output performance of the SA-TENG is strongly influenced by two main parameters including the deformation of the SA-TENG and the distance between the external PA film and the rubber shell. **d**–**d** At an operating frequency of 0.45 Hz, the SA-TENG achieved a V_{OC} of ~ 67.71 V, a Q_{SC} density of ~ 35.35 μC/m^2, and an I_{SC} density of ~ 0.83 mA/m^2. With permission from the authors (2016) [51]. **g** The HM-TENG was developed in 2019 to effectively harvest both mechanical and raindrop energy. **h** Applying pressure on the dielectric film increased elastomer deformation, which could intensify the electrostatic field and raise the output signals from the HM-TENG. **i** With an external load resistance of 13 MΩ, the HM-TENG generated a power density of 0.72 mW/cm^2. With permission from Elsevier Ltd. (2019) [52]

mechanical force in determining the output performance of electrostatic-field-driven AC L-S TENGs and underscores hierarchical micro-nanostructuring as an effective design strategy for optimizing energy scavenging technologies. The HM-TENG demonstrated the potential of surface engineering to enhance energy conversion efficiency, offering valuable insights for advancing the field of TENGs.

Electrostatic-field-driven AC L-S TENGs have surpassed traditional liquid systems by exploiting dynamic EDL regulation at the dielectric-hydrogel interface, achieving enhanced output performance. In 2020, Bao et al. introduced a single-electrode triboelectric nanogenerator featuring an anti-freezing hydrogel electrode (AH-TENG) [61], as illustrated in Fig. 7.25a. This design incorporated thin silicone rubber layers as the top and bottom dielectric surfaces, while a 1 M LiCl ionic

hydrogel, selected for its exceptional mechanical stability and sub-zero temperature resilience, serves as the conductive electrode. This configuration rendered the AH-TENG highly efficient in freezing environments. During operation, human skin, serving as an electropositive dielectric, interacted with the electronegative silicone rubber. Contact induced negative charging on the silicone, while subsequent separation triggered ion redistribution within the EDL at the dielectric-hydrogel interface, facilitating electron flow through the grounding circuit. This cyclic contact-separation mechanism enabled continuous power generation. Performance tests demonstrated a V_{OC} of approximately 285 V and a Q_{SC} of ~ 90 nC. The I_{SC} increased from 6.7 to 15.5 μA as the frequency rose from 0.5 to 2.5 Hz (Fig. 7.25b), indicating a frequency-dependent enhancement in output. When connected to various load resistances, the AH-TENG exhibited P_R scaling with frequency, achieving a maximum P_R density of 626 mW/m^2 at 2.5 Hz (Fig. 7.25c). The AH-TENG demonstrated exceptional output performance even under sub-zero conditions, exhibiting remarkable adaptability to both low-temperature and high-stretch environments. These attributes position the AH-TENG as an outstanding candidate for energy scavenging in demanding conditions.

Additionally, differences in electronegativity between dielectric materials significantly influence charge transfer during S-S CE, thereby impacting the output performance of electrostatic-field-driven AC L-S TENGs. In 2021, Xia et al. introduced a fully transparent and stretchable triboelectric nanogenerator (EC-TENG) based on edible-grade silicone and crystal mud [62], as shown in Fig. 7.25d. By exploiting a substantial difference in electronegativity between materials, the EC-TENG achieved ultra-high voltage outputs. Systematic selection of dielectric materials with varying electronegativities interacting with silicone created electrostatic fields of different strengths, modulating the EDL at the silicone-crystal mud interface. This approach generated diverse electrical signals, directly correlating the electronegativity disparity to EC-TENG performance. Experimental results revealed that greater electronegativity differences led to stronger electrostatic fields, which enhanced EC-TENG efficiency (Fig. 7.25e). Under compression using nitrile gloves at 5 Hz, the EC-TENG achieved an I_{SC} of 25.96 μA, a V_{OC} of 1400 V, and a Q_{SC} of 150 nC. With an optimal load resistance of 40 MΩ, the device attained a P_R density of 0.17 mW/cm^2 (Fig. 7.25f). Furthermore, leveraging triboelectric sequence principles improved the device's electrical performance, significantly enhancing its energy-scavenging efficiency. These results underscore the potential of employing unidirectional electrostatic fields to regulate EDL charge distribution in energy-scavenging systems. Encapsulating liquid or gel components in electrostatic-field-driven AC L-S TENGs further enhanced their flexibility and adaptability, making them ideal for wearable applications, such as biomechanical energy scavenging or self-powered motion monitoring. Future research should focus on optimizing design parameters and broadening the applications of this technology in self-powered wearable systems, which show great promise for advanced biomechanically responsive electronics.

Overall, L-S TENGs effectively generated either constant current or AC outputs, especially in scenarios where traditional power sources are limited or impractical. However, their reliance on the insulating properties of dielectric materials typically

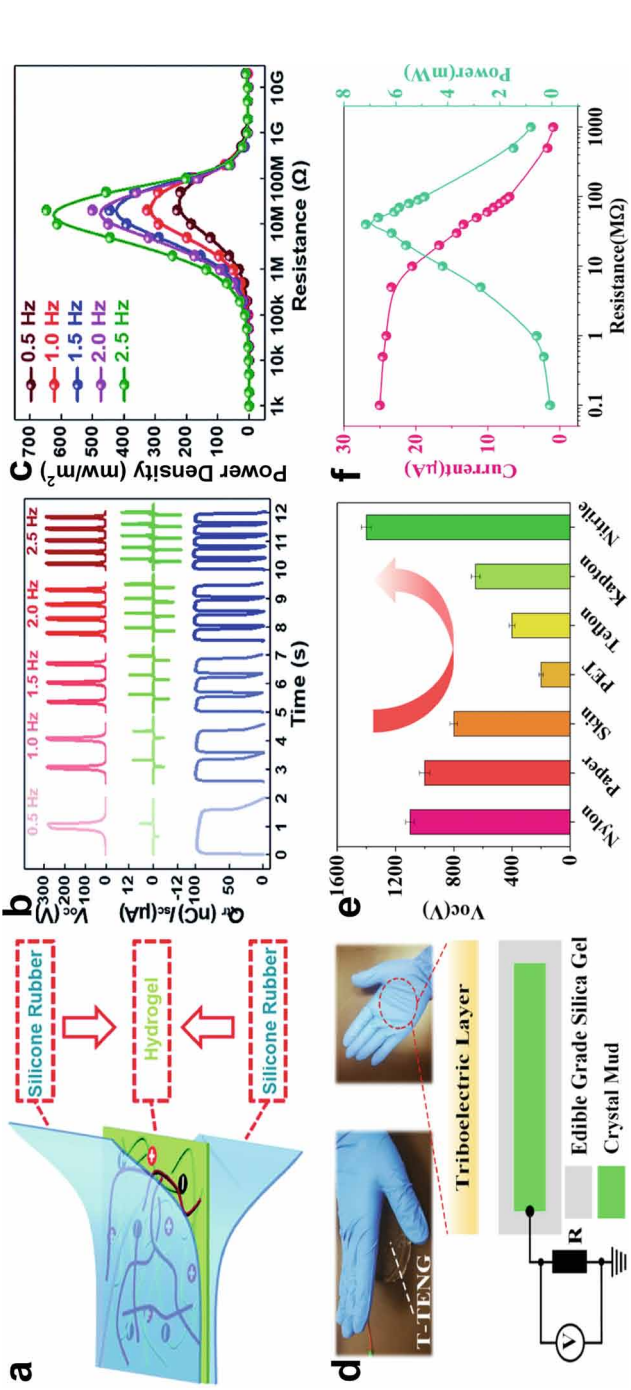

Fig. 7.25 A series of electrostatic-field-driven AC L-S TENGs effectively leveraging dynamic EDL regulation at the dielectric-hydrogel interface and their output characteristics. **a** The AH-TENG was developed in 2020. **b** The I_{SC} increased from 6.7 to 15.5 μA as the frequency rose from 0.5 to 2.5 Hz. **c** The P_R density could reach 626 mW/m^2 at 2.5 Hz. With permission from Royal Society of Chemistry (2020) [61]. **d** In 2021, an EC-TENG based on edible-grade silicone and crystal mud was developed. **e** Larger electronegativity differences allowed for a stronger electrostatic field, which, in turn, enhanced EC-TENG performance. **f** With an optimal load resistance of 40 MΩ, the EC-TENG achieved a P_R density of 0.17 mW/cm^2. With permission from Elsevier Ltd. (2021) [62]

resulted in higher internal resistance. While this elevated resistance facilitated the production of high-voltage outputs suitable for high-voltage applications, it concurrently constrained current output. Thus, optimizing L-S TENG performance for practical use necessitated a delicate balance between voltage and current outputs, particularly in scenarios demanding higher power density. Striking this balance is crucial to unlocking their potential in advanced technologies such as flexible electronics, wearable devices, and renewable energy systems.

7.4.3.2 Various Types of TINGs

Wang's two-step model demonstrated the establishment of a highly efficient ionic-electronic coupling interface in iontronics. This approach marked a pivotal advancement over traditional electronics by enabling optimized ionic-electronic charge exchange at the interface, thereby achieving energy efficiency far exceeding that of conventional electronic systems. A compelling analogy was the human brain, which functions as an integrated iontronic processor, consuming only about 12 W of power [11], whereas replicating its functions with an electronic system would require tens of megawatts. This pronounced contrast underscored the transformative potential of iontronics in advancing the next generation of energy-efficient technologies. In 2023, Wei et al. presented a triboiontronics system that harnessed bidirectional electrostatic fields generated by S-S CE to precisely regulate charge distribution within the EDL [7]. This system effectively controlled charge redistribution within the Stern layer and the polarity of charges in the diffuse layer. In Stage I, the water made contact with an electronegative dielectric material (Dielectric I), forming a stable EDL. The Stern layer carried a small net negative charge, while the diffuse layer contained a modest concentration of free cations (Fig. 7.26a). In Stage II, when Dielectric I contacted a pre-positively charged, electropositive dielectric material (Dielectric II), S-S CE occurred, resulting in additional charge transfer. The positive electrostatic field from Dielectric II intensified the net negative charge in the Stern layer and increased the concentration of free cations in the diffuse layer (Fig. 7.26b). In Stage III, the removal of Dielectric II caused electrons to be retained on Dielectric I, generating a negative electrostatic field that attracted cations to the L-S contact interface. This process resulted in a net positive charge in the Stern layer and an abundance of free anions in the diffuse layer (Fig. 7.26c). This triboiontronic system demonstrated how bidirectional electrostatic fields could dynamically regulate charge redistribution and ion migration within the Stern layer, providing precise control over the charge polarity in the diffuse layer. This approach laid the foundation for advanced iontronic systems capable of high-efficiency charge manipulation and information processing, driving innovation in energy-efficient applications.

Wei et al. made a notable advancement in triboiontronic research by developing a bionic neural circuit capable of dynamically regulating the EDL through bidirectional electrostatic fields [7]. This circuit could emulate the brain's coordination of body movements, such as walking, by efficiently transmitting signals from the central nervous system to control limb motion with minimal energy consumption.

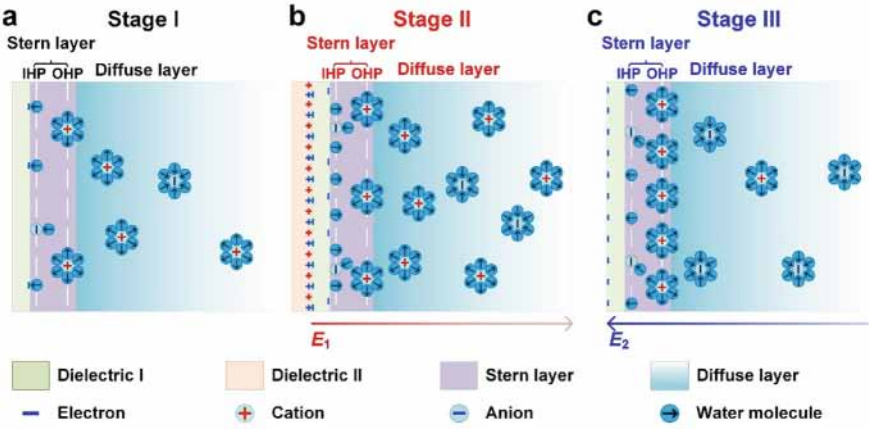

Fig. 7.26 A triboiontronics system was introduced in 2023, which utilized bidirectional electrostatic fields generated by S-S CE to regulate charge distributions in the EDL **a** In Stage I, the water contacted an electronegative Dielectric I, establishing a stable EDL. **b** In Stage II, Dielectric I contact with a pre-positively charged Dielectric II. The pre-positive charges on the Dielectric II generate a positive electrostatic field, intensifying the net negative charge in the Stern layer and increasing the concentration of free cations in the diffuse layer. **c** In Stage III, as dielectric II is removed, its electrons transferred to the surface of Dielectric I form a negative electrostatic field that attracts cations to the L-S interface, resulting in a net positively charged Stern layer and abundant free anions in the diffuse layer. With permission from Elsevier Ltd. (2023) [7]

Replicating similar functionality in traditional electronics would necessitate complex systems comprising multiple diodes and external power supplies. In contrast, the triboiontronic bionic neural circuit provided a more streamlined, energy-efficient alternative through a three-stage operation, as illustrated in Fig. 7.27a. In Stage I, the system remained in a resting state, simulating the central nervous system at rest. In this stage, the positively charged rabbit fur did not contact the initial polyethylene terephthalate (PET) film and a water droplet was added to the charge-collecting layer, with all external circuits remaining disconnected. In Stage II, contact between the positively charged rabbit fur and the PET film caused the water droplet, now enriched with free cations, to induce forward electron transfer in the external circuit, as indicated by the red arrows. Finally, in Stage III, when the rabbit fur was removed, the charge polarity of the water droplet shifted to free anions, inducing reverse electron transfer in the external circuit, highlighted in blue. This bionic neural circuit encoded physical signals as ionic charge polarities within the diffuse layer and converted them into electronic signals, demonstrating effective cross-media information transmission. Through this mechanism, the bionic circuit enabled the control of a virtual robot's coordinated walking movements, as shown in Fig. 7.27b. In Stage I, with the circuit at rest, the virtual robot remained stationary. By adjusting the contact states between the rabbit fur and the PET film in Stages II and III, the ionic polarities in the water droplet enabled direct control over the robot's multi-degree-of-freedom rhythmic and coordinated movements. Unlike conventional silicon-based circuits, triboiontronic systems

leveraged ionic-electronic coupling to create streamlined, self-powered platforms. These platforms could revolutionize human-computer interactions by providing secure, energy-efficient interfaces. The integration of triboiontronic bionic neuromorphic circuits, which feature distributed processing and high biocompatibility, could advance information flows in fields such as in-sensor computing, implantable neural interfaces, and low-power neuromorphic devices. In 2023, Wang et al. provided an insightful preview of the "triboiontronics" concept introduced by Wei et al. [63] (Fig. 7.27c), emphasizing the importance of dynamic EDL control in applications like interface control, biosensing, and human-computer interactions. A key challenge in energy-scavenging systems that dynamically manage the EDL is optimizing ionic migration to maximize energy transfer efficiency and ensure accurate information flow. This necessitates precise control over ionic dynamics and flux. Enhancing system design to minimize energy loss and improve transmission efficiency, particularly through real-time sensing and feedback control of ion migration, holds significant promise. Addressing these challenges is crucial for advancing the next generation of energy-scavenging and information-processing technologies.

In addition to the influence of external electrostatic fields, the type and concentration of ions within a liquid also played a crucial role in modulating the charge density and distribution within the EDL. This regulation mechanism was explored in detail by Wei et al. in 2024, and the process could be broadly divided into three stages [64]. In Stage I (Fig. 7.28a), when the water droplet initially contacted the dielectric surface, the ion concentration was too low to support effective ion migration at the L-S contact interface. As a result, an initial EDL formed at the interface, but the charge density within the diffuse layer of the droplet remained minimal. In Stage II (Fig. 7.28b), as the ion concentration in the LiCl solution droplet increased slightly, the solution's conductivity improved, facilitating enhanced ion migration. This, in turn, led to an increase in charge density within the EDL, with the triboelectric charge in the diffuse layer of the droplet reaching its peak as the concentration rises to around 10^{-5} M. In Stage III (Fig. 7.28c), further increases in LiCl concentration led to a decrease in the contact charge within the diffuse layer. This reduction was likely due to the screening effect created by the dense EDL, where a higher ion concentration limited further charge transfer at the dielectric-liquid interface. As illustrated in Fig. 7.28d, droplets of LiCl solutions at varying concentrations slid across the PTFE surface, showing distinct patterns of triboelectric charge in the diffuse layer at each stage of EDL adjustment. The generated triboelectric charge levels varied according to the ion concentration, reflecting the influence of ion concentration on charge migration behavior. Across all tested concentrations, a positive triboelectric charge was produced. However, when droplets of [EMIM]Cl reach a concentration of 0.1 M or higher, the polarity of the triboelectric charge reversed to negative, likely due to the unique EDL structures induced by the asymmetry of anions and cations at higher concentrations (Fig. 7.28e). This demonstrated that by adjusting the ion type and concentration in the liquid, the charge density and distribution in the EDL could be controlled, offering a tunable approach to modulating the charge polarity in the droplet.

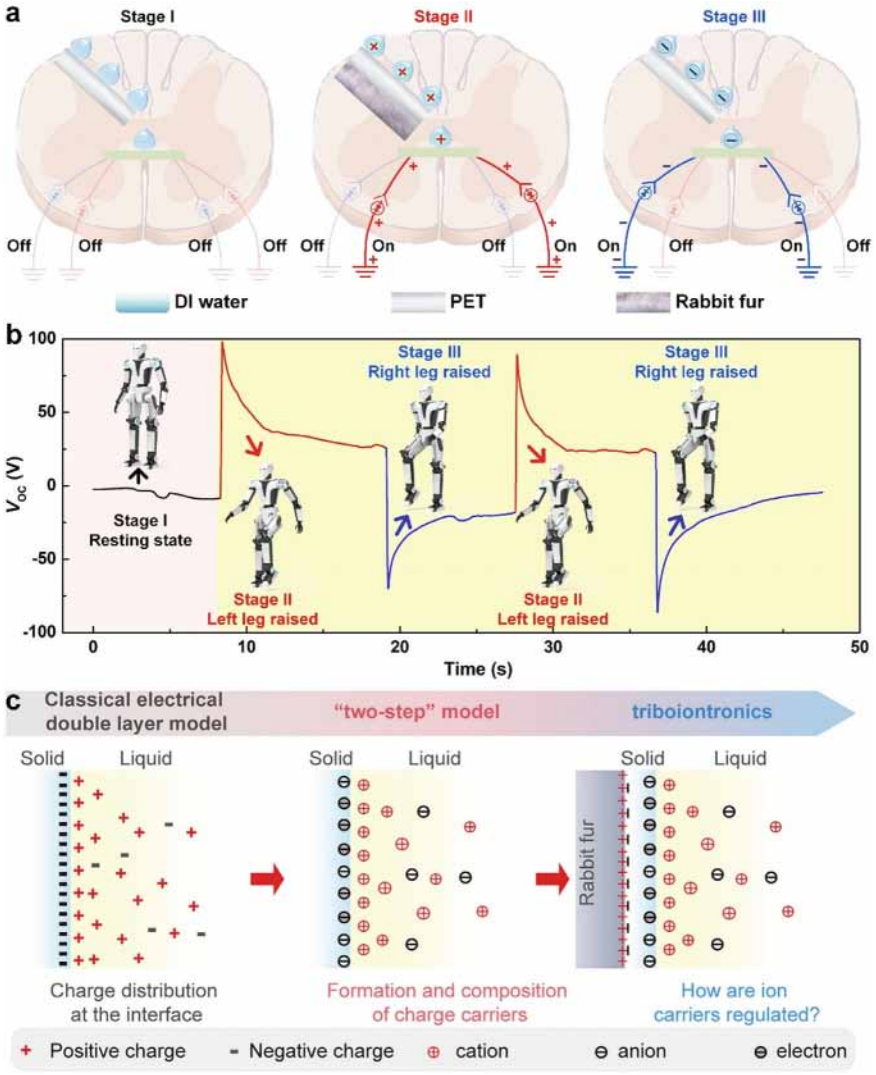

Fig. 7.27 A bionic neurologic circuit capable of dynamically regulating the EDL using bidirectional electrostatic fields was developed in 2023. **a** The three operation stages of the bionic neurologic circuit. **b** The bionic neurologic circuit can direct a virtual robot to perform coordinated walking motions. With permission from Elsevier Ltd. (2023) [7]. **c** In 2023, Wang et al. provided an insightful preview of the "triboiontronics" concept introduced by Wei et al. With permission from Elsevier Ltd. (2023) [63]

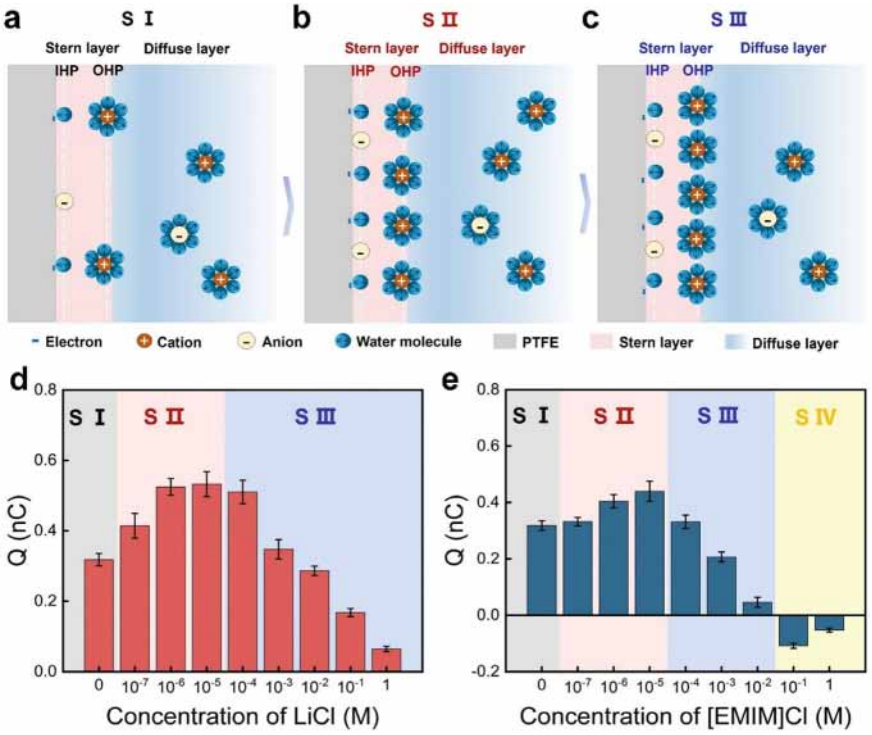

Fig. 7.28 The regulation mechanism of the ion type and concentration on modulating charge density and distribution within the EDL was explored in detail in 2024. **a** In Stage I, when the water droplets initially contact the dielectric surface, the ion concentration in the droplet is too low to fully support effective ion migration at the L-S contact interface. **b** In Stage II, as the ion concentration in the LiCl solution droplet slightly increases, the solution's conductivity improves, facilitating greater ion migration. **c** In Stage III, upon further increases in LiCl concentration, the contact charge within the diffuse layer begins to decrease. **d** Droplets of LiCl solutions at various concentrations slide across the PTFE surface, displaying distinct patterns of triboelectric charges within the diffuse layer at each stage of the EDL adjustment. **e** When droplets of [EMIM]Cl reach a concentration of 0.1 M or above, the triboelectric charge polarity reverses to negative. With permission from Wiley-VCH GmbH (2024) [64]

The flexible regulating of charge carried by droplets enabled effective control of their movement under the influence of an electrostatic field generated by S-S CE[64]. As shown in Fig. 7.29a, droplets with varying ion concentrations exhibited distinct motion behaviors when driven by a constant electrostatic field. Notably, the 10^{-5} M LiCl droplet traveled the longest distance and attained the highest average velocity, while droplets of 0.1 M and 1 M [EMIM]Cl showed a reversal in direction. This reversal was likely due to differences in triboelectric charge polarity,

which were influenced by distinct EDL structures. This approach offered advantages in antigravity movement, flexibility, and minimized surface and energy limitations compared to other methods (Fig. 7.29b). The plug-and-play droplet manipulation system consisted of two main modules: a pre-charged module and a functional module. The pre-charge module used L-S CE to control charge density and polarity, while the functional module was adaptable for diverse tasks, including chemical concentration detection, reaction regulation, and logic circuit construction. In Fig. 7.29c, the functional module was divided by the zone with micron-sized pillars, which facilitated simultaneous droplet transfer and sorting, enhancing selectivity in chemical reactions. This design included a positively charged region on the left and a negatively charged region on the right, enabling dynamic control of droplet movement. Moreover, the droplets served as carriers for both energy and information transfer, effectively supporting logic control within circuits without the need for complex power or electronic components. For instance, by controlling the movement of the droplet, the lift direction of a robot's leg could be synchronized, thereby enabling logic-based control functions within the human-machine interface, as depicted in Fig. 7.29d.

In triboiontronics, dynamic regulation of the EDL facilitates both efficient information transfer in bionic neural circuits and enhanced energy solutions in TINGs. TINGs could produce effective pulsed DC outputs either by modulating the charge density within the diffuse layer of the EDL adjacent to the dielectric surface or by inducing asymmetric EDLs at the interface between an ultra-thin conductor on a dielectric substrate and a contacting liquid. In TINGs that regulated the charge density of the diffuse layer, an ion concentration gradient was established, promoting directed ionic migration to generate ionic current. This ionic current modulated the electrical displacement current, leading to high-power-density DC ionic-electronic coupling output[7], as shown in Fig. 7.30. In the initial state (Fig. 7.30a), the TING was in the separation phase. A mist of positively charged DI water, generated by L-S CE, was sprayed onto the dielectric layer, forming an EDL with a high density of cations in the nano-confined diffuse layer. As the bottom charge-collecting layer approached the dielectric layer, now covered by the positively charged water film, the positive charges in the diffuse layer rapidly transferred to the surface of the bottom charge-collecting layer, generating a larger ionic current (Fig. 7.30b). In the subsequent stage, when the dielectric layer fully contacted the bottom charge-collecting layer, any remaining water film was squeezed out of the TING (Fig. 7.30c). Electrons were transferred from the bottom charge-collecting layer to the dielectric layer surface through the S-S CE. As the dielectric layer began to separate from the bottom charge-collecting layer, electrostatic induction drove electrons from the top charge-collecting layer to the bottom charge-collecting layer, generating an electrical displacement current (Fig. 7.30d). The ionic current and electrical displacement current flow in the same direction, demonstrating that the TING could achieve high-power-density DC ionic-electronic coupling output. When the TING returned to the initial separation phase, the positively charged water mist was reapplied, reestablishing the EDL. This cyclic application of water mist illustrated how L-S CE dynamically modulated charge density within the diffuse layer, producing a stable and consistent DC ionic-electronic

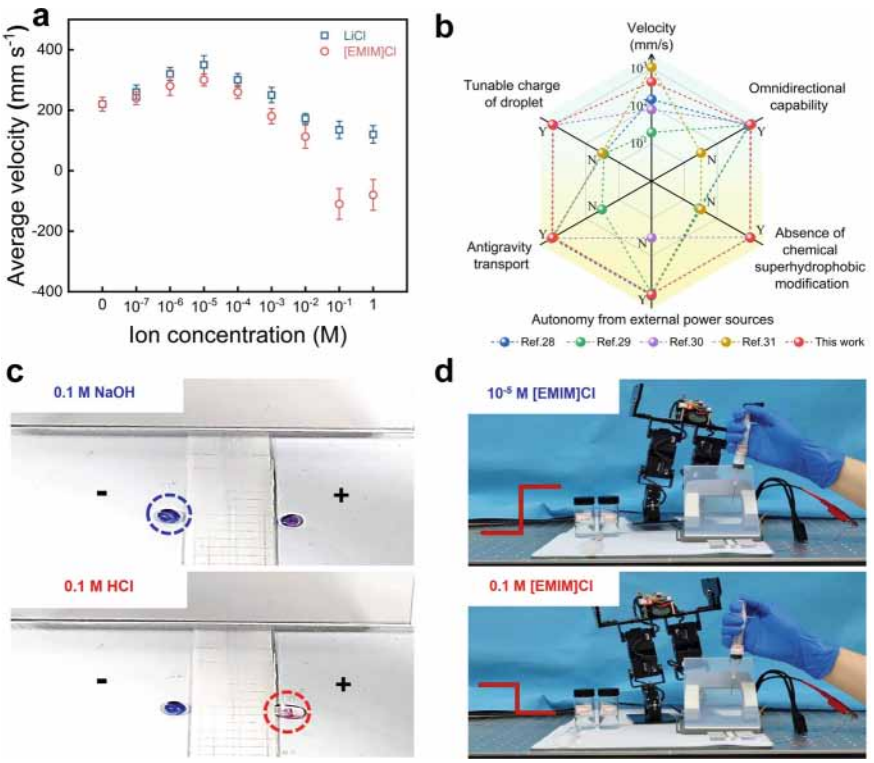

Fig. 7.29 The flexible tuning of charge carried by droplets enables effective control of their movement under the influence of an electrostatic field generated by S-S CE, which was studied in detail in 2024. **a** Droplets with varying ion concentrations exhibit distinct motion behaviors when driven by a constant electrostatic field. **b** This approach exhibits advantages in antigravity movement, flexibility, and minimized surface and energy limitations compared to other methods. **c** The functional module divided by micron-sized pillars supports simultaneous droplet transfer and sorting, enhancing selectivity in chemical reactions. **d** Directing droplet movement can synchronize the lift direction of a robot's leg, thus enabling logic-based control functions. With permission from Wiley-VCH GmbH (2024) [64]

coupling output. Such an approach underscored the potential of EDL regulation in enhancing energy scavenging efficiency, power density, and overall system stability, offering significant advancements in sustainable energy technology.

Based on the principle of regulating charge density in the diffuse layer, the DC-TING was introduced in 2023 (Fig. 7.31a) [7], achieving enhanced charge collection on the dielectric surface by incorporating a carbon nanotube film with a high specific surface area as the charge-collecting layer. Initially, in the absence of the positively charged DI water mist (i.e., in a dry state), the DC-TING operated as a conventional mechanically droplet-driven AC L-S TENG, generating an AC signal of approximately 0.8 μA through S-S CE and electrostatic induction at a frequency of 1 Hz (Fig. 7.31b). However, upon the application of positively charged DI water mist to

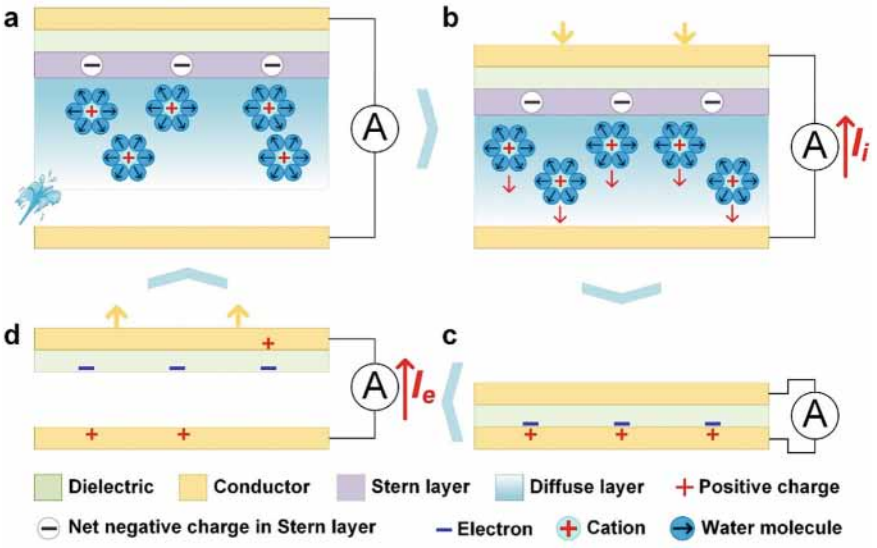

Fig. 7.30 Based on regulating the charge density of the diffuse layer, TINGs could generate a high-power-density DC ionic-electronic coupling output. **a** The mist of positively charged DI water generated by L-S CE is sprayed onto the dielectric layer, forming an EDL with a high density of cations in the nano-confined diffuse layer. **b** As the bottom charge-collecting layer approaches the dielectric layer covered with the positively charged water film, the positive charges in the diffuse layer rapidly transfer to the bottom charge-collecting layer's surface, generating a larger ionic current. **c** When the dielectric layer fully contacts the bottom charge-collecting layer, electrons are transferred from the bottom charge-collecting layer to the dielectric layer surface based on the CE effect. **d** As the dielectric layer begins to separate from the bottom charge-collecting layer, electrostatic induction drives electrons from the top charge-collecting layer to the bottom charge-collecting layer, resulting in an electrical displacement current. With permission from the authors (2024) [56]

the dielectric surface, the DC-TING quickly switched to a DC output mode. As ionic charges accumulated on the dielectric surface, the DC output stabilized at around 6.0 μA. This result confirmed that regulating charge density within the diffuse layer of the EDL could generate a stable DC ionic-electronic coupling output. Further analysis of the charge replenishment time revealed a crucial parameter affecting the DC-TING output (Fig. 7.31c). At lower operational frequencies, extended replenishment times facilitated greater charge accumulation in the diffuse layer, resulting in increased current output when the stored charge was transferred to the charge-collecting layer. Moreover, the hydrophilicity of the dielectric surface played a significant role in determining the output performance of the TING (Fig. 7.31d). Micro-engraving techniques increased the dielectric surface area but introduced air pockets within the microstructure, reducing L-S contact and, consequently, diminishing the surface's hydrophilicity. To address this issue, plasma treatment was employed to introduce oxygen-containing groups on the micro-engraved surface, enhancing hydrophilicity and promoting greater accumulation of positive charges in the diffuse layer, thereby

improving device performance (Fig. 7.31e). Through these charge replenishment strategies, the dielectric surface's charge density was effectively sustained, allowing the TING to deliver consistent and efficient DC output. The device achieved an impressive I_{SC} density of 360 mA/m^2 and a Q_{SC} density of 5.6 mC/m^2 (Fig. 7.31f and g), while its P_R density reached 126.4 W/m^2 (Fig. 7.31h). These findings underscored the importance of optimizing charge density to maximize TING efficiency, offering significant potential for advancing energy scavenging technologies. However, a key challenge for energy scavenging devices that rely on dynamic regulation of the diffuse layer is the reduced charge transfer resulting from increased internal resistance of the dielectric material. Therefore, future research should focus on materials with lower internal resistance, such as those with enhanced conductivity or low resistivity. Additionally, optimizing dielectric materials and improving electrode materials could further enhance charge transfer efficiency.

In addition to generating high-power-density DC ionic-electronic coupling output through regulation of the diffuse layer charge density, TINGs based on asymmetric EDLs exhibited a distinct operational mechanism that significantly enhanced Q_{SC} density [8]. These TINGs employed a hybrid material, consisting of a dielectric substrate with an ultra-thin conductive layer closely adhered to it. This ultra-thin conductive layer functioned both as the charge-collecting layer and as a modulator of the liquid-substrate CE properties, which in turn regulated the charge distribution and migration in the EDL. In the first step, a thin gold (Au) layer was sputtered onto a PET dielectric substrate, forming the hybrid material (Au/FEP). Upon contact with water, the Au layer interacted with the PET surface through microscopic cracks, generating L-S CE and establishing a stable EDL on the substrate (Fig. 7.32a). Subsequently, as the top Au/PET layer made contact with the water, a second L-S CE event occurred, establishing a new EDL at the top contact surface and forming a dual EDL system with pronounced asymmetry. This asymmetry generated an ion concentration gradient, which drove ion migration within the asymmetric EDLs. The ion migration induced electron transfer in the external circuit, thereby generating an ionic current (Fig. 7.32b). When the top Au/PET layer detached, ion migration briefly ceased (Fig. 7.32c). Through repeated contact-separation cycles, the ion concentration gradient gradually diminished, but ion migration persisted until equilibrium was reached between the two EDLs (Fig. 7.32d). This innovative mechanism enhanced Q_{SC} efficiency and underscored the potential of TINGs for various energy-scavenging applications, effectively converting mechanical motion into electrical output.

A physically adsorptive direct-current triboiontronic generator (PDC-TING) based on asymmetric EDLs was also developed [8] (Fig. 7.33a). The device utilized the Au/PET hybrid layer that included a PET dielectric substrate with an ultra-thin Au layer deposited via magnetron sputtering. To optimize the PDC-TING's output performance, three key strategies were introduced to enhance the ion concentration gradient, thereby maximizing device efficiency. The first strategy involved electrostatic field adjustment (Fig. 7.33b). By applying a positive electrostatic field to the bottom Au/PET hybrid layer in the PDC-TING, the I_{SC} was significantly increased. This enhancement was attributed to the influence of the positive electrostatic field on the bottom EDL density, which strengthened the ion concentration

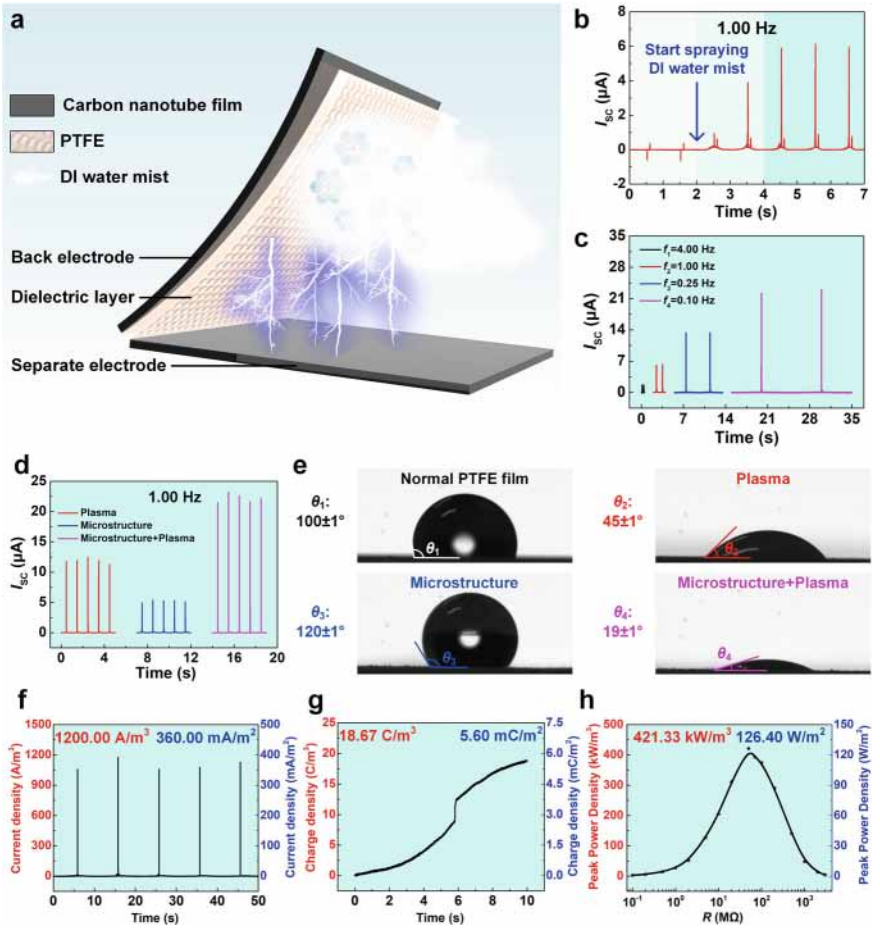

Fig. 7.31 Based on the above principle of regulating the charge density of the diffuse layer, a DC-TING was introduced. **a** The schematic diagram of the DC-TING. **b** Upon application of positively charged DI water mist to the dielectric surface, the DC-TING quickly shifted to a DC output mode from the AC output mode. **c** At lower operational frequencies, prolonged replenishment times enabled a greater buildup of charge in the diffuse layer, resulting in increased current output when this charge was subsequently transferred to the charge-collecting layer. **d** The hydrophilicity of the dielectric surface was found to impact DC-TING performance significantly. **e** Plasma treatment to introduce oxygen-containing groups on the micro-engraved surface successfully enhanced hydrophilicity, facilitating greater accumulation of positive charges in the diffuse layer and improving device performance. **f–h** The DC-TING achieved an impressive I_{SC} density of 360 mA/m^2 and Q_{SC} density of 5.6 mC/m^2 respectively, while the DC-TING's P_R density reached 126.4 W/m^2. With permission from Elsevier Ltd. (2023) [7]

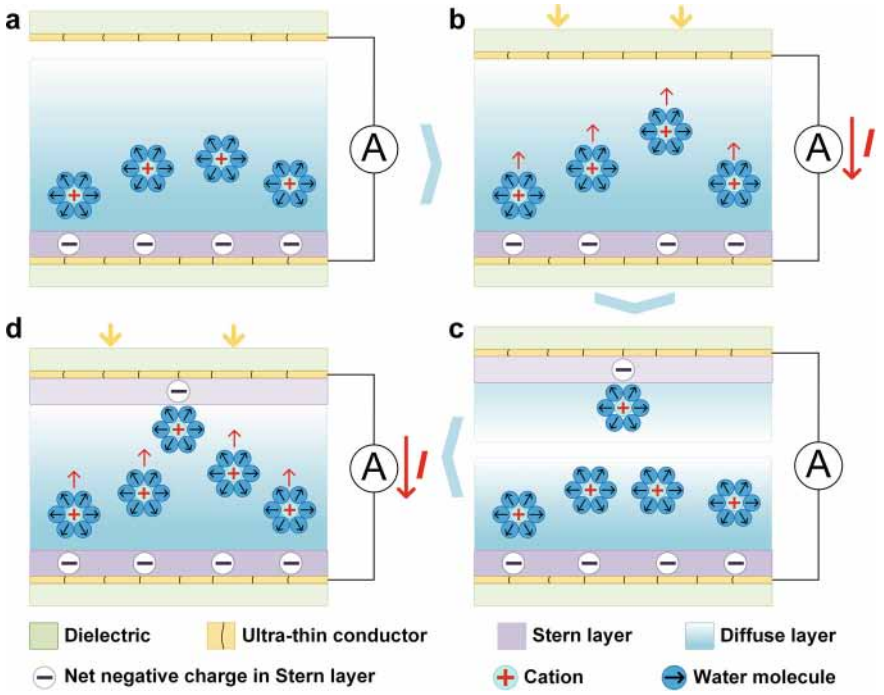

Fig. 7.32 The operating mechanism of TINGs based on asymmetric EDLs. **a** When the water contacts the bottom Au/PET surface, it interacts directly with the PET through microscopic cracks in the Au layer, generating L-S CE and establishing a stable EDL. **b** When the top Au/PET layer descends into contact with the water, asymmetric EDLs are created and an ion concentration gradient is established, driving electron transfer within the external circuit and producing an ionic current. **c** The subsequent detachment of the top Au/PET layer momentarily halts ion migration. **d** Through repeated contact-separation cycles, the ion concentration gradient gradually dissipates, although ion migration continues until equilibrium is achieved between the two EDLs. With permission from the authors (2024) [56]

gradient, promoting greater ion migration and thus improving device performance. The second strategy focused on enhancing the hydrophilicity of the bottom Au/PET hybrid layer (Fig. 7.33c). Plasma treatment was applied to improve the surface's hydrophilicity, which significantly boosted the EDL density at the bottom contact interface. This, in turn, amplified the ion concentration gradient, further improving output performance. The third strategy aimed at increasing the ion concentration in the liquid (Fig. 7.33d). By replacing water with a higher concentration LiCl solution, the bottom EDL density was increased, lowering the internal resistance and reducing energy losses. This modification enhanced both signal sensitivity and output strength. Collectively, these strategies resulted in a substantial improvement in PDC-TING performance, with an I_{SC} density of 26.00 A/m^2 (Fig. 7.33e), a Q_{SC} density of 412.54 mC/m^2 (Fig. 7.33f), and a P_R density of 8.45 W/m^2. The increased Q_{SC} density was pivotal in maximizing energy output efficiency, signal strength, and detection

sensitivity in TINGs. The enhanced Q_{SC} density enabled more charge to be collected per contact cycle, providing a reliable power source for self-powered devices in energy applications. For information flow applications, the improved charge transfer density enabled stronger signal outputs and enhanced sensitivity for rapid detection and precise monitoring of subtle environmental changes.

TINGs that leveraged asymmetric EDLs demonstrated the ability to produce ionic currents that facilitated ionic rectification, enabling traditional AC TENGs to deliver stable DC ionic-electronic coupled outputs. Building on this concept, Ouyang et al. advanced the technology by designing a TING using a polyacrylamide (PAAm)

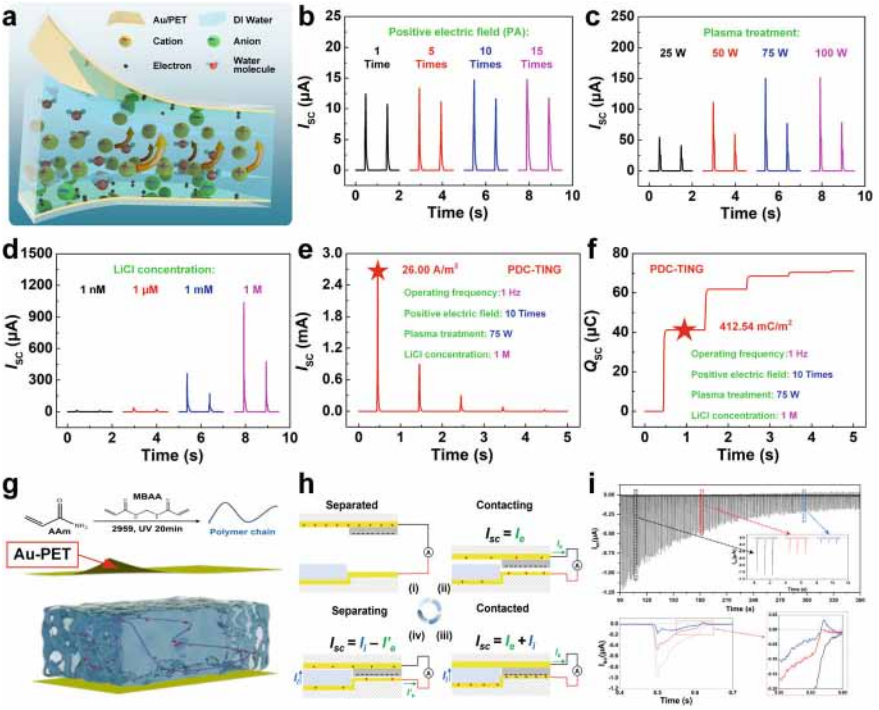

Fig. 7.33 A series of TINGs based on asymmetric EDLs and their output characteristics. **a** The PDC-TING based on asymmetric EDLs was developed in 2024 **b** Applying a positive electrostatic field on the bottom of the PDC-TING successfully increased I_{SC}. **c** Plasma treatment was applied to improve the hydrophilicity of the bottom Au/PET hybrid layer, significantly boosting the EDL density at the bottom contact layer. **d** Replacing water with a higher concentration of LiCl solution increased the bottom EDL density and lowered internal resistance, which minimized energy losses and enhanced signal sensitivity and strength. **e**–**f** The PDC-TING could achieve an optimal output with an I_{SC} density of 26.00 A/m^2 and a Q_{SC} density of 412.54 mC/m^2. With permission from the authors (2024) [8]. **g** In 2024, a TING via asymmetric EDLs was designed, which facilitated the rectification of AC TENG outputs. **h** The principle of ionic rectification. **i** The close correlation between ionic and electronic current variations highlights the crucial role of ionic current in enhancing both energy output and rectification efficiency. With permission from American Chemical Society (2024) [65]

hydrogel in asymmetric EDLs in 2024, which facilitated the rectification of AC TENG outputs[65] (Fig. 7.33g). The hydrogel was created by injecting a reagent solution into a custom mold, followed by UV-induced polymerization, and then integrated with a hybrid material consisting of a PET substrate coated with an ultrathin Au layer. As the hydrogel approached the top hybrid material, the ionic current, driven by the ion concentration gradient, flowed in the same direction as the electrical displacement current induced by electrostatic induction. Upon separation, the direction of the ionic current remained unchanged, while the electrical displacement current was modulated by the ionic current, thereby validating efficient ionic rectification and ultimately generating a DC ionic-electronic coupled output (Fig. 7.33h). Experimental data confirmed a strong correlation between the variations in ionic and electronic currents, underscoring the role of ionic current in enhancing both energy output and rectification efficiency (Fig. 7.33i). This flexible rectification approach overcame the limitations of conventional rigid rectifiers, offering advantages in adaptability, lightweight design, and energy efficiency. This advancement positioned it as a significant step forward for wearable and flexible electronics.

Overall, triboiontronic systems and various types of TINGs were expected to garner increasing research attention due to their remarkable potential in several key areas. These systems held promise for efficient energy scavenging, enabling sustainable power generation from environmental sources. Additionally, the precise control of interfacial EDLs within these systems offered new avenues for optimizing energy conversion efficiency and regulating ionic currents in real time. This regulation was pivotal for the development of biomimetic nervous systems, which were designed to replicate the dynamic response characteristics of biological neural circuits. As a result, triboiontronic systems and TINGs showed significant promise in a variety of applications, ranging from self-powered wearable electronics and flexible energy devices to advanced health-monitoring technologies and intelligent robotics, thereby showcasing their broad and diverse potential for future technological advancements.

7.5 Contact Electrification at Liquid-Semiconductor Interfaces

Beyond the conventional liquid-conductor or liquid-dielectric interfaces, the movement of liquids over semiconductor surfaces could also generate a constant current output, a phenomenon known as the tribovoltaic effect, in which the DI water was considered analogous to a wide-bandgap semiconductor. The conventional tribovoltaic effect at solid semiconductor-semiconductor interfaces was first discovered by Wang et al. in 2019 and was considered to be a DC output mechanism [6]. Specifically, when p-type and n-type semiconductors came into contact, the difference in their Fermi energy levels drove the transfer of electrons between them, with holes migrating in the opposite direction [66]. This electron-hole transfer established a built-in electric field at the contact interface, effectively forming a p-n junction.

Upon relative motion between the two semiconductor surfaces, interactions between surface atoms led to the formation of new chemical bonds, releasing what Wang et al. referred to as "Bindington", a form of frictional energy. In the tribovoltaic effect, this energy behaves similarly to excitons in the photovoltaic effect, as it excites electron-hole pairs at the interface, enabling them to move either along or against the built-in electric field. This movement generates a constant current within an external circuit, underscoring the potential of semiconductor-semiconductor interface interactions for sustainable DC power generation.

The tribovoltaic effect also could be effectively harnessed in liquid-semiconductor interfaces to generate a stable output current. Additionally, this approach offered a promising strategy for reducing friction and wear between solid semiconductor surfaces, potentially extending the device's lifespan. In 2020, Lin et al. developed a nanogenerator based on liquid-semiconductor interfaces using water droplets sliding across a silicon (Si) surface[67], as illustrated in Fig. 7.34a. Notably, when the water droplets moved over p-type Si, the nanogenerator generated consistent V_{OC} and I_{SC}, which remained stable regardless of the sliding direction, as shown in Fig. 7.34b and c. The operational mechanism relied on the difference in Fermi levels between the water and the Si surface. The Fermi level of water was higher than that of p-type Si, and upon separation, the band diagram in Fig. 7.34d showed the resulting difference. When the water droplet contacted the p-type Si, electrons transferred from the droplet to the Si surface, establishing a built-in electric field at the interface. Concurrently, new chemical bonds formed at the contact interface (Fig. 7.34e). As the droplet moved, the bond formation released frictional energy, which excited electron-hole pairs on the p-type Si surface (Fig. 7.34f). These pairs, driven by the built-in electric field, then migrated in alignment with or opposite to the electric field direction, generating a stable output in the external circuit (Fig. 7.34g). When the water droplet interacted with n-type Si, where the Fermi level was higher, electrons were transferred from the Si surface to the droplet, creating a reverse built-in electric field. This reverse field drove electron-hole pairs in a directional motion, resulting in an opposite constant output in the external circuit. The corresponding energy band diagrams for this process at various stages of operation are shown in Fig. 7.34h–k.

Further investigations by Zheng et al. explored the impact of temperature on the performance of nanogenerators based on liquid-semiconductor interfaces[68], focusing specifically on the interactions between the liquid and semiconductor surfaces (Fig. 7.35a). Their study revealed that as the temperature increased from 30 to 90 °C, the CA of water droplets on the Si surface decreased from 86.72° to 60.36° (Fig. 7.35b). This reduction in CA effectively expanded the droplet's contact area with the Si surface, thereby enhancing output performance by increasing the available interface for charge transfer. For example, when water droplets slid over an n-type Si surface, the elevated temperature resulted in higher-density electron-hole pair excitation. This was due to the increased frictional energy at the interface as the droplet moved, leading to a significant enhancement in DC output performance, as shown in Fig. 7.35c and d. Similarly, when the droplet contacted p-type Si, the reverse constant output also increased with temperature, as depicted in Fig. 7.35f–h.

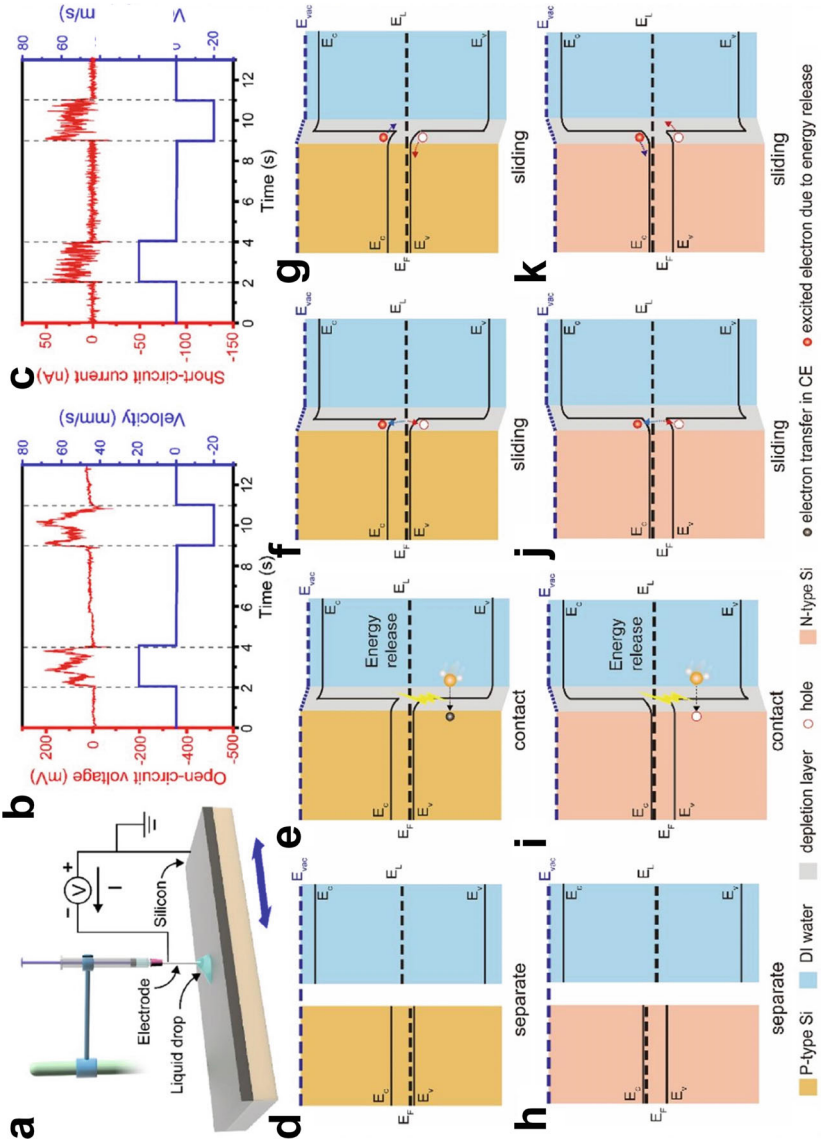

Fig. 7.34 Triboelectric effect at liquid-semiconductor interfaces. **a** In 2020, Lin et al. developed a nanogenerator based on semiconductor-liquid interfaces using droplets of water sliding across the Si surface. **b–c** When the water droplets moved over p-type Si, the nanogenerator generated a consistent V_{OC} and I_{SC} that remained stable regardless of the sliding direction. **d–g** The energy band diagram transitions when the droplet slides on the p-type Si surface. **h–k** The energy band diagram transitions when the droplet slides on the n-type Si surface. With permission from Elsevier Ltd. (2020) [67]

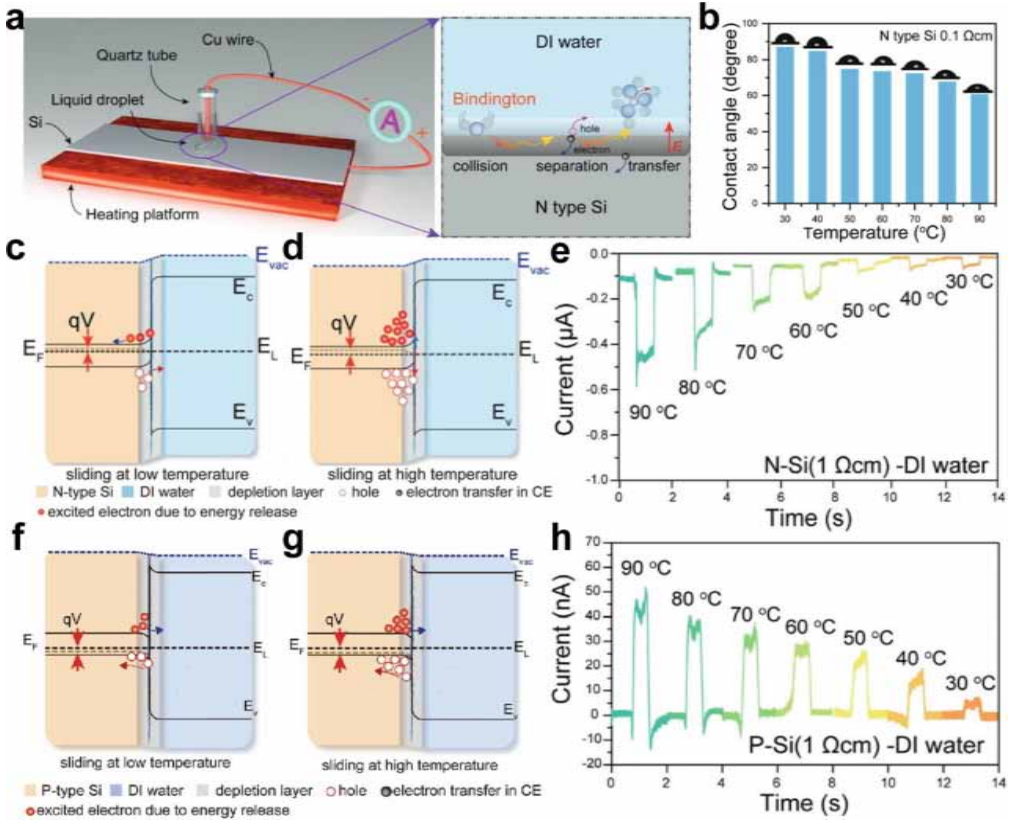

Fig. 7.35 The effect of temperature on the tribovoltaic effect at the liquid-semiconductor interface has been studied in 2021. **a** The test system. **b** As the temperature increased from 30 to 90 °C, the CA of water droplets on the Si surface decreased from 86.72° to 60.36°. **c–e** When water droplets slide over an n-type Si surface, the rising temperature results in higher-density electron–hole pair excitation due to increased friction energy at the interface during droplet sliding, leading to a notable enhancement in DC output performance. **f–h** Similarly, when the droplet contacts p-type Si, the reverse constant output increases with temperature. With permission from Wiley-VCH GmbH (2021) [68]

Overall, these findings underscored the potential of nanogenerators based on liquid-semiconductor interfaces to improve device performance by leveraging the inherent properties of semiconductors. The temperature-dependent changes in CA and frictional energy at the contact interface contributed to higher charge transfer efficiency, resulting in a more stable and enhanced DC output. Additionally, the intrinsic characteristics of semiconductors, such as their ability to reduce internal resistance, further improved current density. These results indicated that nanogenerators based on semiconductor-liquid interfaces can be optimized for greater efficiency and durability, making them suitable for applications that require consistent energy output and minimal wear.

7.6 Summary

In this chapter, a thorough analysis of the mechanisms behind CE at L-S contact interfaces was provided, with a focus on charge transfer processes across interfaces involving solid conductors, dielectrics, and semiconductors. The formation of the EDL, a fundamental structure that governed charge dynamics at these interfaces, was discussed in detail. Key topics included the quantification of ion and electron transfer, advanced modeling of electron transfer mechanisms, and an exploration of the hybrid characteristics of the EDL, offering deeper insights into the fundamental physics underlying L-S CE. Furthermore, this chapter explores techniques for dynamically regulating the EDL using electric fields or mechanical means to control charge carrier behavior, including polarity and ionic flux. By manipulating ion migration and optimizing charge carrier concentration at the contact interface, these methods enable precise regulation of energy scavenging, storage, and information flow. Devices such as supercapacitors, electrochemical sensors, L-S TENGs, and TINGs have been developed based on L-S contact interface regulation. Dynamic control of the EDL at liquid-conductor interfaces has enabled stable energy storage and sensitive sensors, while at liquid-dielectric interfaces, it has facilitated high-efficiency energy scavenging. At liquid-semiconductor interfaces, the tribovoltaic effect, driven by L-S CE, provides an effective energy generation method. These advancements highlighted the significant potential of dynamic EDL regulation across various contact interfaces for supporting efficient energy generation and information flow.

References

1. H. Helmholtz, Ueber einige gesetze der vertheilung elektrischer ströme in körperlichen leitern mit anwendung auf die thierisch-elektrischen versuche. Ann. Phys. **165**(6), 211–233 (1853)
2. M. Gouy, Sur la constitution de la charge électrique à la surface d'un électrolyte. J. Phys. Theor. Appl. **9**(1), 457–468 (1910)

3. D.L. Chapman, A contribution to the theory of electrocapillarity. Philos. Mag. **25**(148), 475–481 (1913)
4. D.C. Grahame, The electrical double layer and the theory of electrocapillarity. Chem. Rev. **41**(3), 441–501 (1947)
5. S. Lin, L. Xu, A. Chi Wang, Z.L. Wang, Quantifying electron-transfer in liquid-solid contact electrification and the formation of electric double-layer. Nat. Commun. **11**(1), 399 (2020)
6. Z.L. Wang, A.C. Wang, On the origin of contact-electrification. Mater. Today **30**, 34–51 (2019)
7. X. Li, S. Li, X. Guo, J. Shao, Z.L. Wang, D. Wei, Triboiontronics for efficient energy and information flow. Matter **6**(11), 3912–3926 (2023)
8. X. Li, R. Li, S. Li, Z.L. Wang, D. Wei, Triboiontronics with temporal control of electrical double layer formation. Nat. Commun. **15**(1), 6182 (2024)
9. X. Li, Z.L. Wang, D. Wei, Scavenging Energy and Information through dynamically regulating the electrical double layer. Adv. Funct. Mater. **34**(42), 2405520 (2024)
10. J. Maier, Nanoionics: ion transport and electrochemical storage in confined systems. Nat. Mater. **4**(11), 805–815 (2005)
11. R. Sarpeshkar, Analog versus digital: extrapolating from electronics to neurobiology. Neural Comput. **10**(7), 1601–1638 (1998)
12. S.Z. Bisri, S. Shimizu, M. Nakano, Y. Iwasa, Endeavor of iontronics: from fundamentals to applications of ion-controlled electronics. Adv. Mater. **29**(25), 1607054 (2017)
13. L.L. Zhang, X.S. Zhao, Carbon-based materials as supercapacitor electrodes. Chem. Soc. Rev. **38**(9), 2520–2531 (2009)
14. M. Şahin, F. Blaabjerg, A. Sangwongwanich, A comprehensive review on supercapacitor applications and developments. Energies **15**(3), 674 (2022)
15. A. González, E. Goikolea, J.A. Barrena, R. Mysyk, Review on supercapacitors: technologies and materials. Renew. Sustain. Energy Rev. **58**, 1189–1206 (2016)
16. R. Liu, Z.L. Wang, K. Fukuda, T. Someya, Flexible self-charging power sources. Nat. Rev. Mater. **7**(11), 870–886 (2022)
17. N. Liu, R. Chen, Q. Wan, Recent advances in electric-double-layer transistors for bio-chemical sensing applications. Sensors **19**(15), 3425 (2019)
18. R. Feiner, T. Dvir, Tissue–electronics interfaces: from implantable devices to engineered tissues. Nat. Rev. Mater. **3**(1), 17076 (2017)
19. S. Zhao, P. Tseng, J. Grasman, Y. Wang, W. Li, B. Napier, B. Yavuz, Y. Chen, L. Howell, J. Rincon, F.G. Omenetto, D.L. Kaplan, Programmable hydrogel ionic circuits for biologically matched electronic interfaces. Adv. Mater. **30**(25), e1800598 (2018)
20. G. Schiavone, S.P. Lacour, Conformable bioelectronic interfaces: mapping the road ahead. Sci. Transl. Med. **11**(503), eaaw5858 (2019)
21. G.G. Wallace, S.E. Moulton, G.M. Clark, Applied physics. Electrode-cellular interface. Science **324**(5924), 185–186 (2009)
22. R. Jalili, A. Kanneganti, M.I. Romero-Ortega, G.G. Wallace, Implantable electrodes. Curr. Opin. Electrochem. **3**(1), 68–74 (2017)
23. M. Hu, J. Ren, Y. Pan, L. Cheng, X. Xu, C.L. Tan, H. Sun, Y. Shi, S. Yan, Scaled elastic hydrogel interfaces for brain electrophysiology. Adv. Funct. Mater. **34**(46), 2407926 (2024)
24. M.T. Darby, C.S. Cucinotta, The role of water at electrified metal-water interfaces unravelled from first principles. Curr. Opin. Electrochem. **36**, 101118 (2022)
25. P. Sebastián-Pascual, Y. Shao-Horn, M. Escudero-Escribano, Toward understanding the role of the electric double layer structure and electrolyte effects on well-defined interfaces for electrocatalysis. Curr. Opin. Electrochem. **32**, 100918 (2022)
26. D. Strmcnik, K. Kodama, d.V.D. van, J. Greeley, V.R. Stamenkovic, N.M. Markovic, The role of non-covalent interactions in electrocatalytic fuel-cell reactions on platinum. Nat. Chem. **1**(6), 466–472 (2009)
27. H. Shi, Z. Cai, J. Patrow, B. Zhao, Y. Wang, Y. Wang, A. Benderskii, J. Dawlaty, S.B. Cronin, Monitoring local electric fields at electrode surfaces using surface enhanced raman scattering-based stark-shift spectroscopy during hydrogen evolution reactions. ACS Appl. Mater. Inter. **10**(39), 33678–33683 (2018)

28. T. Asset, A.G. Oshchepkov, F. Maillard, G.A. Tsirlina, Electrocatalysis, diverse and forever young. Electrochim. Acta **507**, 145174 (2024)
29. A. Frumkin, N. Polianovskaya, I. Bagotskaya, N. Grigoryev, Electrocatalysis and electrode surface properties. J. Electroanal. Chem. Interfacial Electrochem. **33**(2), 319–328 (1971)
30. S. Trasatti, Work function, electronegativity, and electrochemical behaviour of metals. J. Electroanal. Chem. Interfacial Electrochem. **39**(1), 163–184 (1972)
31. R. Parsons, J.O.M. Bockris, Calculation of the energy of activation of discharge of hydrogen ions at metal electrodes. Trans. Faraday Soc. **47**(8), 914–928 (1951)
32. B.E. Conway, B.V. Tilak, Interfacial processes involving electrocatalytic evolution and oxidation of H2, and the role of chemisorbed H. Electrochim. Acta **47**(22–23), 3571–3594 (2002)
33. J. Tafel, Über den Verlauf der elektrolytischen Reduktion schwer reduzierbarer Substanzen in schwefelsaurer Lösung. Z. Phys. Chem. **34U**(1), 187–228 (1900)
34. F. Haber, R. Russ, Über die elektrische Reduktion. Z. Phys. Chem. **47U**(1), 257–335 (1904)
35. N. Kobosew, N.I. Nekrassow, Bildung freier Wasserstoffatome bei Kathodenpolarisation der Metalle. Zeitschrift für Elektrochemie und angewandte physikalische Chemie **36**(8), 529–544 (2010)
36. A.T. Hubbard, Electrochemistry of well-defined surfaces. Acc. Chem. Res. **13**(6), 177–184 (2002)
37. J.C. Canullo, W.E. Triaca, A.J. Arvia, Electrochemical faceting of single crystal platinum electrodes. J. Electroanal. Chem. Interfacial Electrochem. **200**(1–2), 397–400 (1986)
38. J. Liu, Z. Yang, S. Li, Y. Du, Z. Zhang, J. Shao, M. Willatzen, Z.L. Wang, D. Wei, Nonaqueous contact-electro-chemistry via triboelectric charge. J. Am. Chem. Soc. **146**(46), 31574–31584 (2024)
39. Z. Zhang, D. Jiang, J. Zhao, G. Liu, T. Bu, C. Zhang, Z.L. Wang, Tribovoltaic effect on metal–semiconductor interface for direct-current low-impedance triboelectric nanogenerators. Adv. Energy Mater. **10**(9), 1903713 (2020)
40. S.Q. Lin, X.Y. Chen, Z.L. Wang, Contact electrification at the liquid-solid interface. Chem. Rev. **122**(5), 5209–5232 (2022)
41. M. Zheng, S. Lin, L. Xu, L. Zhu, Z.L. Wang, Scanning probing of the tribovoltaic effect at the sliding interface of two semiconductors. Adv. Mater. **32**(21), 2000928 (2020)
42. C. Xu, Y. Zi, A.C. Wang, H. Zou, Y. Dai, X. He, P. Wang, Y.-C. Wang, P. Feng, D. Li, Z.L. Wang, On the electron-transfer mechanism in the contact-electrification effect. Adv. Mater. **30**(15), 1706790 (2018)
43. Z.L. Wang, Triboelectric nanogenerator (TENG)—sparking an energy and sensor revolution. Adv. Energy Mater. **10**(17), 2000137 (2020)
44. K. von Burg, P. Delahay, Photoelectron emission spectroscopy of inorganic anions in aqueous solution. Chem. Phys. Lett. **78**(2), 287–290 (1981)
45. Y. Takakuwa, M. Niwano, M. Nogawa, H. Katakura, S. Matsuyoshi, H. Ishida, H. Kato, N. Miyamoto, Photon-stimulated desorption of H+ ions from oxidized Si(111) surfaces. Jpn. J. Appl. Phys. **28**(12R), 2581 (1989)
46. J. Nie, Z. Ren, L. Xu, S. Lin, F. Zhan, X. Chen, Z.L. Wang, Probing contact-electrification-induced electron and ion transfers at a liquid-solid interface. Adv. Mater. **32**(2), 1905696 (2020)
47. R. Zhang, S. Wang, M.-H. Yeh, C. Pan, L. Lin, R. Yu, Y. Zhang, L. Zheng, Z. Jiao, Z.L. Wang, A streaming potential/current-based microfluidic direct current generator for self-powered nanosystems. Adv. Mater. **27**(41), 6482–6487 (2015)
48. J. Chi, C. Liu, L. Che, D. Li, K. Fan, Q. Li, W. Yang, L. Dong, G. Wang, Z.L. Wang, Harvesting water-evaporation-induced electricity based on liquid-solid triboelectric nanogenerator. Adv. Sci. **9**(17), 2201586 (2022)
49. Z.-H. Lin, G. Cheng, L. Lin, S. Lee, Z.L. Wang, Water-solid surface contact electrification and its use for harvesting liquid-wave energy. Angew. Chem. Int. Ed. **52**(48), 1–6 (2013)
50. J. You, J. Shao, Y. He, F.F. Yun, K.W. See, Z.L. Wang, X. Wang, High-electrification performance and mechanism of a water-solid mode triboelectric nanogenerator. ACS Nano **15**(5), 8706–8714 (2021)

51. F. Yi, X. Wang, S. Niu, S. Li, Y. Yin, K. Dai, G. Zhang, L. Lin, Z. Wen, H. Guo, J. Wang, M.-H. Yeh, Y. Zi, Q. Liao, Z. You, Y. Zhang, Z.L. Wang, A highly shape-adaptive, stretchable design based on conductive liquid for energy harvesting and self-powered biomechanical monitoring. Sci. Adv. **2**(6), e1501624 (2016)
52. X. Chen, J. Xiong, K. Parida, M. Guo, C. Wang, C. Wang, X. Li, J. Shao, P.S. Lee, Transparent and stretchable bimodal triboelectric nanogenerators with hierarchical micro-nanostructures for mechanical and water energy harvesting. Nano Energy **64**, 103904 (2019)
53. Y. Wei, X. Li, Z. Yang, J.J. Shao, Z.L. Wang, D. Wei, Contact electrification at the solid-liquid transition interface. Mater. Today **74**, 2–11 (2024)
54. Z.-H. Lin, G. Cheng, S. Lee, K.C. Pradel, Z.L. Wang, Harvesting water drop energy by a sequential contact-electrification and electrostatic-induction process. Adv. Mater. **26**(27), 4690–4696 (2014)
55. G. Zhu, Y. Su, P. Bai, J. Chen, Q. Jing, W. Yang, Z.L. Wang, Harvesting water wave energy by asymmetric screening of electrostatic charges on a nanostructured hydrophobic thin-film surface. ACS Nano **8**(6), 6031–6037 (2014)
56. X. Li, Z.L. Wang, D. Wei, Nanogenerators via dynamic regulation of electrical double layer. Nano Trends **8**, 100062 (2024)
57. Y. Dong, S. Xu, C. Zhang, L. Zhang, D. Wang, Y. Xie, N. Luo, Y. Feng, N. Wang, M. Feng, X. Zhang, F. Zhou, Z.L. Wang, Gas-liquid two-phase flow-based triboelectric nanogenerator with ultrahigh output power. Sci. Adv. **8**(48), eadd0464 (2022)
58. W. Xu, H. Zheng, Y. Liu, X. Zhou, C. Zhang, Y. Song, X. Deng, M. Leung, Z. Yang, R.X. Xu, Z.L. Wang, X.C. Zeng, Z. Wang, A droplet-based electricity generator with high instantaneous power density. Nature **578**(7795), 392–396 (2020)
59. L. Li, X. Li, W. Deng, C. Shen, X. Chen, H. Sheng, X. Wang, J. Zhou, J. Li, Y. Zhu, Z. Zhang, J. Yin, W. Guo, Sparking potential over 1200 V by a falling water droplet. Sci. Adv. **9**(46), eadi2993 (2023)
60. Z. Tang, D. Yang, H. Guo, S. Lin, Z.L. Wang, Spontaneous wetting induced by contact-electrification at liquid-solid interface. Adv. Mater. **36**(25), 2400451 (2024)
61. D. Bao, Z. Wen, J. Shi, L. Xie, H. Jiang, J. Jiang, Y. Yang, W. Liao, X. Sun, An anti-freezing hydrogel based stretchable triboelectric nanogenerator for biomechanical energy harvesting at sub-zero temperature. J. Mater. Chem. A **8**(27), 13787–13794 (2020)
62. K. Xia, Y. Tian, J. Fu, Z. Zhu, J. lu, Z. Zhao, H. Tang, Z. Ye, Z. Xu, Transparent and stretchable high-output triboelectric nanogenerator for high-efficiency self-charging energy storage systems. Nano Energy **87**, 106210 (2021)
63. L. Zhang, D. Wang, Triboiontronics based on dynamic electric double layer regulation. Matter **6**(11), 3698–3699 (2023)
64. R. Li, X. Li, Z. Zhang, M. Willatzen, Z.L. Wang, D. Wei, Triboelectric programmed droplet manipulation for plug-and-play assembly. Adv. Funct. Mater. **35**(10), 2416457 (2024)
65. Y. Ouyang, X. Li, S. Li, Z.L. Wang, D. Wei, Ionic rectification by dynamic regulation of the electric double layer at the hydrogel interface. ACS Appl. Mater. Interfaces **16**(14), 18236–18244 (2024)
66. S. Lin, Z. Lin Wang, The tribovoltaic effect. Mater. Today **62**, 111–128 (2023)
67. S. Lin, X. Chen, Z.L. Wang, The tribovoltaic effect and electron transfer at a liquid-semiconductor interface. Nano Energy **76**, 105070 (2020)
68. M. Zheng, S. Lin, L. Zhu, Z. Tang, Z.L. Wang, Effects of temperature on the tribovoltaic effect at liquid-solid interfaces. Adv. Mater. Interfaces **9**(3), 2101757 (2021)